DYNAMIC MODELING AND ANALYSIS OF THE THREE-PHASE VOLTAGE SOURCE INVERTER UNDER STAND-ALONE AND GRID-TIED MODES

by

FALEH A ALSKRAN

B. Sc., Kansas State University 2011

A THESIS

Submitted in partial fulfillment of the requirements for the degree

MASTER OF SCIENCE

Department of Electrical and Computer Engineering
College of Engineering

KANSAS STATE UNIVERSITY
Manhattan, Kansas

2014

Approved by:

Major Professor
Dr. Behrooz Mirafzal

Copyright

Abstract

Increasing energy demand, rising oil prices, and environmental concerns have forced attention to alternative energy sources that are environmentally friendly and independent of fossil fuels. Renewable energy sources (RES) have become an attractive alternative to the traditional energy sources for electric power generation. However, one of the main challenges of RES adaption arises when connecting RES to the electric grid. Voltage source inverters (VSIs), typically, connect RES to the electric grid. Similar to any engineering system, detailed dynamic models of the VSIs are needed for design and analysis purposes. However, due to the non-linearity of VSIs, development of dynamic models that can accurately describe their behavior is a complex task. In this thesis, a detailed averaged-state-space model of the two-level three-phase space vector pulse width modulation VSI and its companion LCL filter is derived. Because VSIs can operate under stand-alone and grid-tied modes, two models were derived for each case. In the derived models, the VSI modulation index m and phase angle ϕ are initially considered constant. In practice, however, these parameters are considered the main control parameters. To model these parameters as control inputs, small-signal models of the VSI under stand-alone and grid-tied modes were derived. To verify the accuracy of the developed large-signal and small-signal models, Matlab/Simulink simulations were carried out. The simulation results were compared against the models results. Moreover, the models were verified through lab experiments. The developed models can be used as design and analysis tools. In addition, the developed models can be used as fast and efficient simulation tools for system studies, when the modeling of switching transients is not needed. Nowadays, the number of VSIs connected to the electric grid is growing exponentially. The amount of time and computation needed to simulate VSIs using simulation software packages can be significantly decreased by the use of the developed models.

Table of Contents

List of Figures

List of Tables

Acknowledgements

I would like to express my sincere gratitude to my major professor Dr. Behrooz Mirafzal for guiding and inspiring me to initiate this research. I am very grateful for his help and continuous support. I would like to extend my thanks and appreciation to Rockwell Automation for donating a motor drive to our Power Electronics Research Lab for research purposes. Their donation was vitally important to complete this research. I would like to thank Dr. Ranga Tallam of Rockwell Automation for his instructions on how to use the donated motor drive. Finally, I would like to extend my gratitude to Dr. Anil Pahwa and Dr. Andrew Rys for being part of my supervisory committee.

Dedication

I dedicate this work to my dear parents.

Chapter 1 - Introduction

This chapter addresses motivation, objectives, and contributions of this thesis. This chapter has three sections. Section 1.1 introduces the problem by discussing the need for modeling voltage source inverters (VSIs). Section 1.2 outlines the objectives and contributions of the thesis. Section 1.3 presents the organization of the thesis.

1.1 Background of the Problem

In recent years, increasing energy demand, rising oil prices, and environmental issues have forced attention to environmentally friendly energy sources that are independent of fossil fuels. Renewable energy sources (RES) have become an attractive alternative to traditional energy sources for two main reasons: RES are free abundant forms of energy and RES do not produce excessive amount of heat or emissions. Therefore, they do not contribute to environmental threats such as pollution and global warming. Sun and wind are two primary RES. Wind energy is typically harvested through wind turbines, while solar energy can be harvested through various ways, such as through photovoltaic (PV) panels. The industry for wind turbines and PV panels has grown exponentially over the past few years. For example, according to the American Wind Energy Association (AWEA), the United States wind power production exceeded 61 GW in 2013. Iowa and South Dakota generated over 20% of their energy needs from wind energy, while 17 other states generated over 5% of their energy needs from wind [1], as shown in Figure 1-1. PV energy production has, also, experienced a significant growth over the last few years. According to a report published by Solar Energy Industries Association (SEIA) and GreenTech Media (GTM), PV installation in the US exceeded 4.7 GW during 2013, an increase of 41% compared to 2012 [2]. Figure 1-2 shows new PV installations capacities by state in 2013.

Connecting RES to the electric grid, however, is not as easy as connecting conventional sources of energy. In PV applications PV panels produce variable DC voltage. The output voltage of the panel is influenced by ambient temperature while the output current is influenced by the sun irradiance level. To connect PV modules to the grid, a voltage source inverter (VSI) must convert variable DC voltage to AC voltage with controlled magnitude and frequency. In wind energy applications the same problem exists. Wind turbines are connected to AC generators, primarily, synchronous generators. Output frequency and magnitude are dependent on wind speed; therefore, uncontrolled AC voltage is rectified into DC voltage and then converted to AC via a VSI.

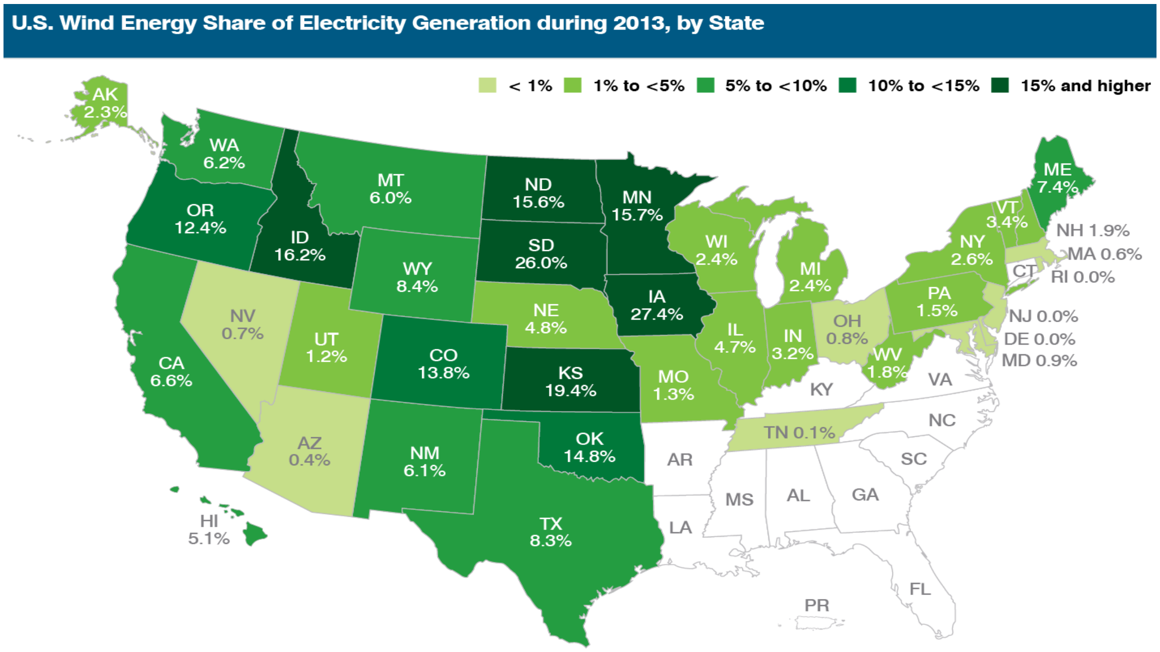

Figure 1-1: Wind Energy Production in the US in 2013 [1]

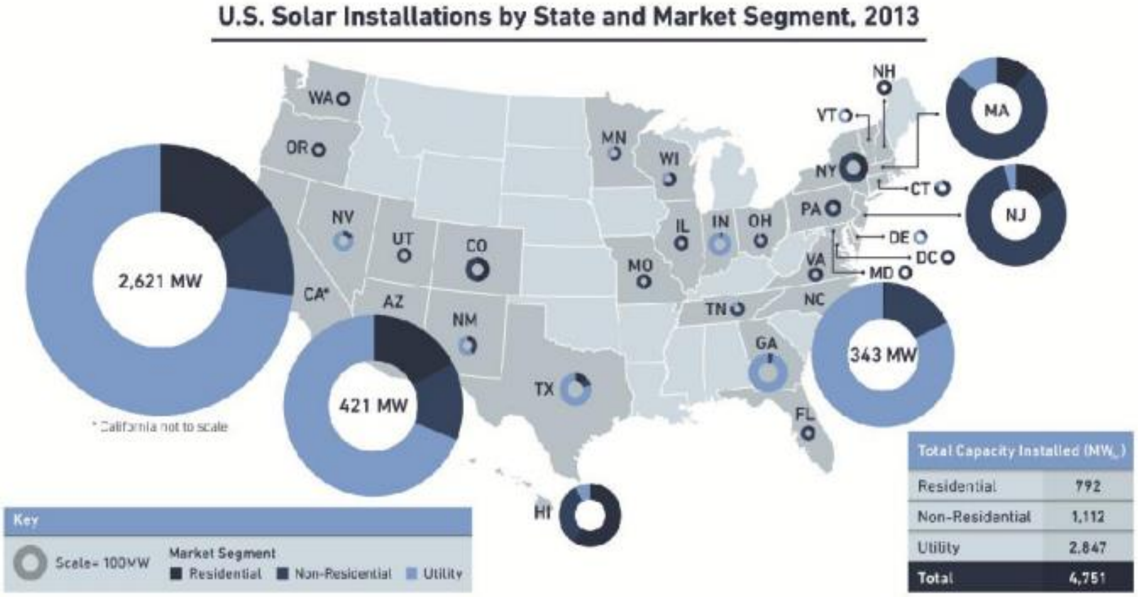

Total Capacity Installed (MW)	
Residential	792
Non-Residential	1,112
Utility	2,847
Total	4,751

Figure 1-2: Capacities of PV Installations in 2013 by State [2]

Beside RES applications, VSIs play an important role in variable speed drive (VSD) applications. In VSD applications varying the frequency of the AC voltage fed to the motor controls the motor speed. In this case AC voltage is typically rectified into DC voltage and then connected to a VSI to produce AC voltage with the required magnitude and frequency.

To evaluate the performance of VSIs, corresponding dynamic large signal models and small signal models must be obtained. These models are required to evaluate the stability of the system and examine its controllability and observability. In addition, these models can provide transfer functions that can be used in different control studies such as: frequency response analysis, controller design, and output filter design. These models can also be used to as simulation tools. Nowadays, due to the rapid adaption of RES, large systems are comprised of large numbers of VSIs. Since VSIs operate at high switching frequencies, simulation software packages require large amounts of computation time to simulate their behavior. Alternatively, dynamic models can be used to significantly reduce the amount of computation time.

However, development of such models has always been considered a complex task. Due to their switching behavior, VSIs are considered non-linear devices; therefore, conventional simple modeling approaches cannot be employed to model these devices.

1.2 Objectives and Contributions of the Thesis

The primary objective of this thesis is to develop accurate models that can describe the behavior of the two-level three-phase VSI under stand-alone and grid-tied modes. These models are simple tools that can be used by other researchers and engineers for different design and analysis purposes, or for use, as simulation tools. In this thesis the state-space averaging method introduced in [3] is used to derive large-signal averaged-state-space models for the three-phase VSI under stand-alone and grid-tied modes. Important control parameters such as VSI modulation index, m, and phase angle between the VSI and the grid, ϕ, were initially considered constant parameters in the developed large-signal models. In practice, m is a variable used to regulate the output voltage of the VSI while ϕ is a variable used to control the power injected to the grid. To consider these control parameters as variable inputs, a small-signal models were developed through introducing small perturbation to these models and then linearizing them around pre-calculated operating points. The small-signal models are used to carry out eigenvalues sensitivity analysis to determine the sensitivity of the system stability to different parameters. The derived models are then verified through Matlab/Simulink simulations and lab experiments.

1.3 Organization of the Thesis

Besides the introductory chapter, Chapter 2 provides a comprehensive review of the Sinusoidal Pulse Width Modulation (SPWM), the Space-Vector Pulse Width Modulation (SVPWM), and the third-harmonic injection Pulse Width Modulation switching techniques for the three-phase VSI. Chapter 3 provides a comprehensive review of two modeling methods: the state-space-averaging method and the black-box method. Because the reference-frame theory was used to simplify the modeling of the VSI in this thesis, the reference-frame theory is also briefly discussed in this chapter. In Chapter 4, the large-signal models and the small-signal models of the three-phase VSI under grid-tied and stand-alone modes are developed. The small signal-models are then used to carry out eigenvalues sensitivity analysis. Chapter 5 verifies the models developed in Chapter 4 through Matlab/Simulink simulations and lab experiments. Chapter 6 concludes this thesis and present advice for future work.

Chapter 2 - Three-Phase Voltage Source Inverters

This chapter discusses operation of the three-phase VSI. While there are several circuits topologies for the three-phase VSI, this thesis focuses on the standard two-level three-phase VSI depicted in Figure 2-1. Several pulse width modulation (PWM) techniques can be used to drive the three-phase VSI, but the most common PWM techniques are:

1) Sinusoidal PWM (SPWM)
2) Third-Harmonic PWM
3) Space Vector PWM (SVPWM)

This chapter contains four sections. Sections 2.1-2.3 discuss the aforementioned PWM and section 2.4 concludes the chapter by briefly comparing PWM techniques. Concluding remarks are also presented in this section.

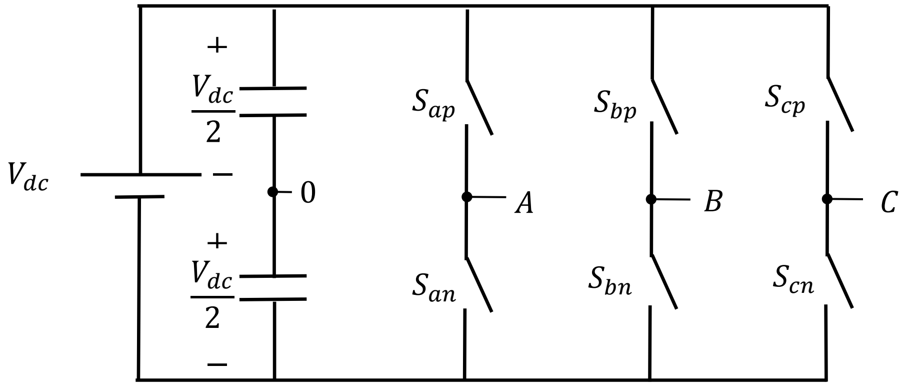

Figure 2-1: Three-Phase VSI

2.1 Sinusoidal PWM

In SPWM, a high frequency carrier signal v_c, is compared to three reference signals 120° apart: v_r^a, v_r^b, and v_r^c, as shown in Figure 2-2(a). When a particular reference signal is higher than the carrier signal the upper switch of the corresponding leg closes to connect that phase to the positive rail of the DC bus while the lower switch opens to prevent shorting the DC bus. Therefore, the upper and lower switches in each leg operate in a complementary manner.

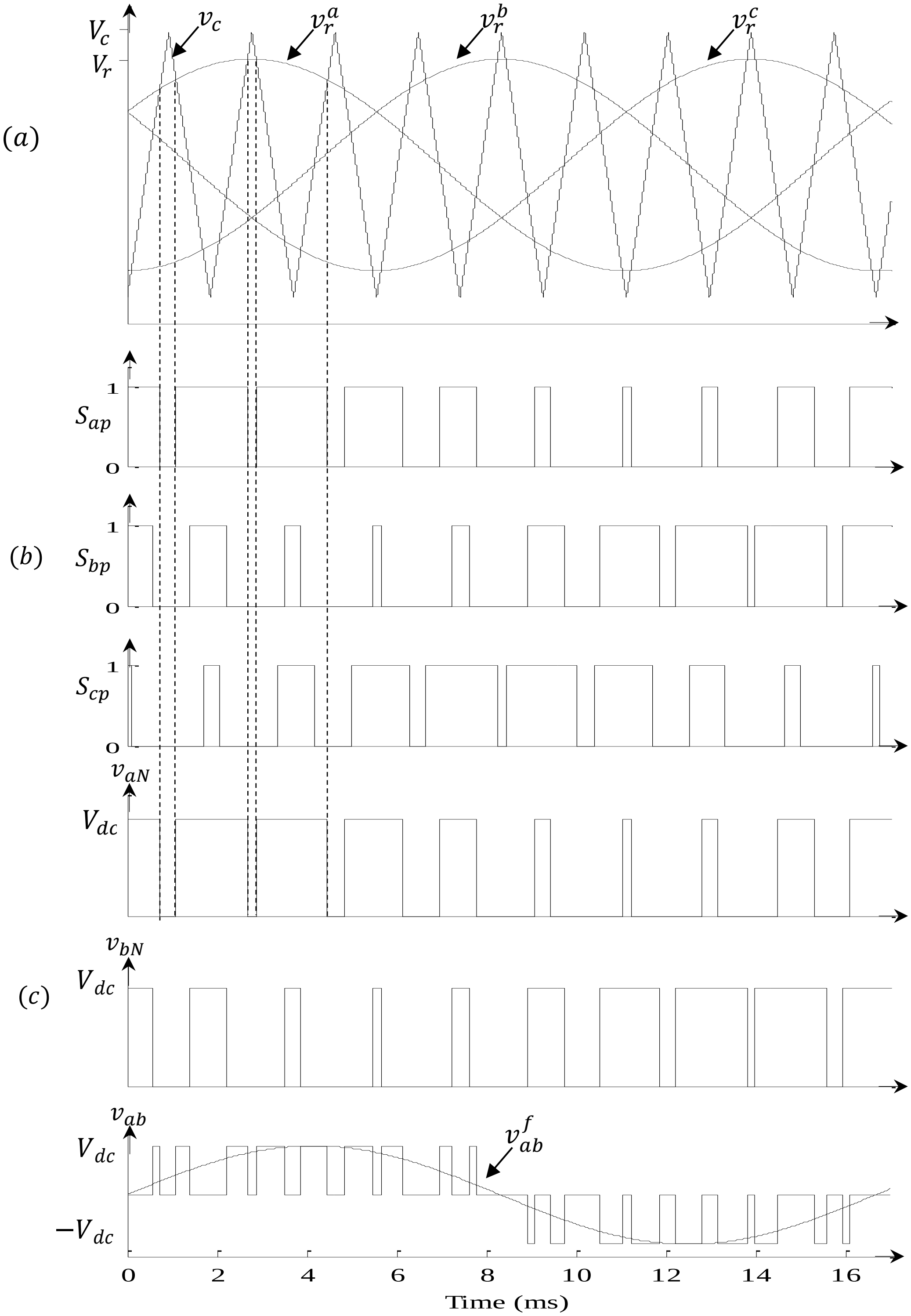

Figure 2-2: SPWM

Control signals for S_{ap}, S_{bp}, and S_{cp} are shown in Figure 2-2(b). Phase voltage waveforms of phase a and phase b along with the line-to-line voltage v_{ab} and its fundamental component v_{ab}^{f} are shown in Figure 2-2(c).

As shown in Figure 2-2(c), the line-to-line voltage waveform is odd, so, all even harmonics do not exist. In addition, triplen harmonics in each phase are in phase with each other; therefore, they do not exist in the line-to-line voltage waveform. For example, consider the 9th harmonic:

$$v_{9aN} = V_9 \sin\big(9(wt)\big) \tag{2-1}$$

$$v_{9bN} = V_9 \sin\left(9(wt - 120^{\circ})\right) = V_9 \sin\big(9(wt)\big) \tag{2-2}$$

Therefore,

$$v_{9ab} = v_{9aN} - v_{9bN} = 0 \tag{2-3}$$

To calculate average output voltage, assume that the carrier signal frequency is much larger than the fundamental frequency, $f_c \gg f$. Under this assumption, the reference signal v_r can be considered constant within one switching cycle T_s as shown in Figure 2-3(a). Voltage waveform in Figure 2-3(b) represents phase-to-midpoint, point 0 in Figure 2-1, voltage. From Figure 2-3(b), the following expression for the average phase-to-midpoint voltage $\hat{v}_{p0}$ can be derived:

$$\hat{v}_{p0} = \frac{1}{T_s}\left\{\frac{V_{dc}}{2}\left(\frac{T_s}{2} + 2t_{ON}\right) - \frac{V_{dc}}{2}\left(\frac{T_s}{2} - 2t_{ON}\right)\right\} \tag{2-4}$$

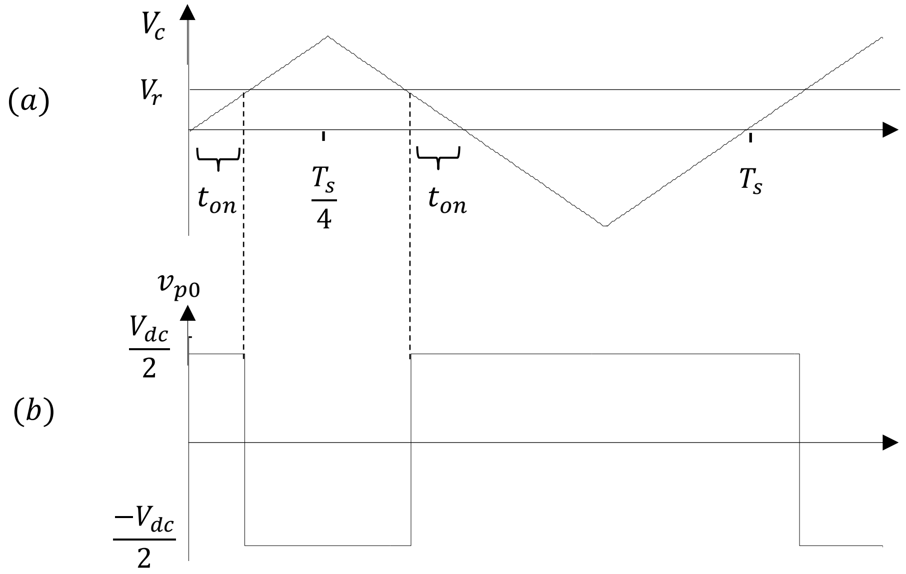

Figure 2-3: SPWM within One Switching Cycle

To further simplify (2-4), consider two similar triangles, extracted from Figure 2-3(a), depicted in Figure 2-4. Using the ratio of the two similar triangles, the following equation can be obtained:

$$t_{on} = \frac{T_S}{4}\frac{V_r}{V_c} \tag{2-5}$$

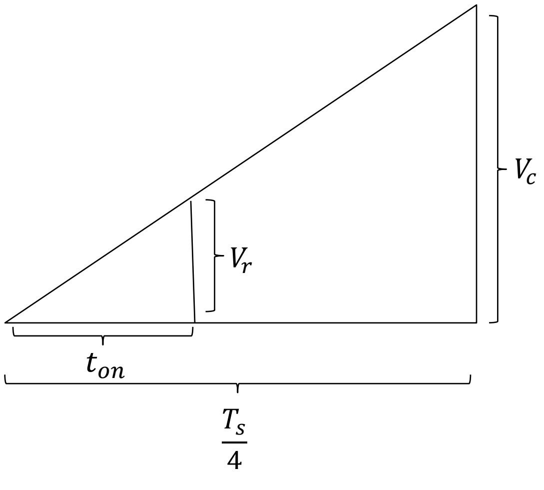

Figure 2-4: Relationship Between v_r and v_c

The ratio of reference signal magnitude to carrier signal magnitude $\frac{V_r}{V_c}$ is referred to as modulation index m and is used to regulate magnitude of output voltage. Combining (2-4) and (2-5) yields:

$$\hat{v}_{p0} = \frac{1}{2} m V_{dc} \tag{2-6}$$

Thus, the RMS line-to-line voltage can be defined as:

$$\hat{v}_{LL} = \frac{\sqrt{3}}{2\sqrt{2}} m V_{dc} \tag{2-7}$$

Mathematical analysis carried out to derive (2-7) is only valid for $0 < m \leq 1$. If m exceeds 1, the inverter goes into what is known as the overmodulation mode, in which, the relationship between input voltage V_{dc} and output voltage v_{LL} becomes non-linear. Larger values of m leads to full overmodulation where v_{LL}output waveform is a square wave, this is also known as square-wave operation. Running, the VSI in the overmodulation mode has the advantage of increasing the magnitude of output voltage. However, as m increases beyond 1, less harmonics are suppressed. Therefore, total harmonic distortion (THD) increases [4].

2.2 Third-Harmonic PWM

The algorithm of third-harmonic PWM is similar to SPWM with the exception of third-harmonic component added to reference signals v_r^a, v_r^b, and v_r^c.The idea of injecting harmonics into reference signals emerged from the need to find a way of increasing m beyond 1 without operating the three-phase VSI under the overmodulation mode. It has been proven in [5] that injecting third harmonic to the reference signal extends the upper boundary of m to 1.155, 15.5 % increase, without going into overmodulation. As shown in Figure 2-5, the fundamental of v_r can exceed v_c, i.e. m is greater than 1. In addition, the presence of a third-harmonic component in phase-voltage waveforms is eliminated from line-to-line voltage waveforms, as proven using Equations (2-1)-(2-3).

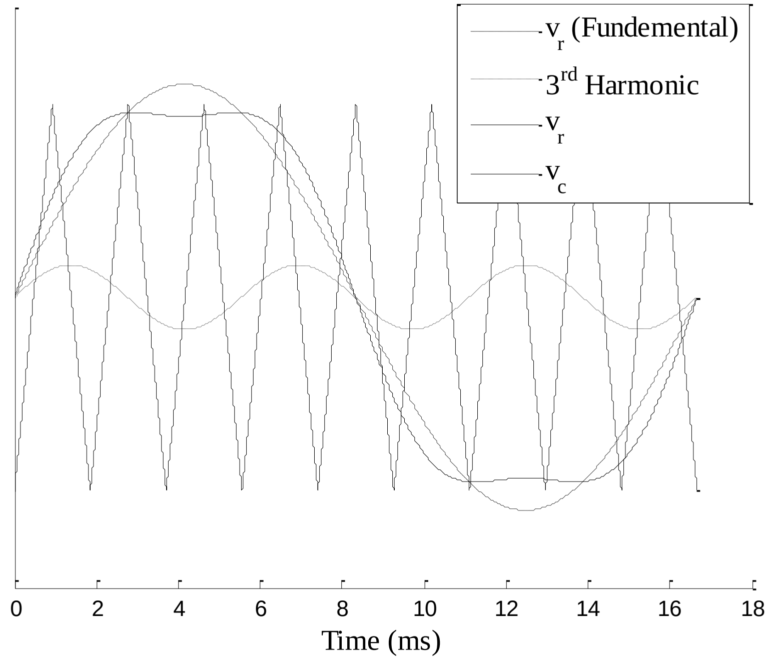

Figure 2-5: Third-Harmonic Injection PWM

2.3 Space Vector PWM

SVPWM is a unique technique. Its uniqueness stems from the fact that it is not dependent on comparing reference signals to any carrier signal in order to make switches change states. For the sake of continuity and increasing understanding of SVPWM, the 180° conduction mode must be discussed first. Assume that the three-phase VSI in Figure 2-1 is connected to a three-phase Y-load, as shown in Figure 2-6, and the VSI follows the switching pattern presented in Table 2-1. The switching pattern in Table 2-1 is given as function of S_k; where S_k is defined for each leg of the inverter as:

$$S_k = \begin{cases} 1, upper\ switch\ is\ ON\ while\ lower\ switch\ is\ OFF \\ 0, lower\ switch\ is\ ON\ while\ upper\ switch\ is\ OFF \end{cases},\ k \in \{a, b, c\} \tag{2-8}$$

As shown in Table 2-1, the fundamental cycle is divided into six sectors and every three sectors (half a cycle or 180°) one leg changes states from 0 to 1 or vice-versa. Thus, every switch conducts for 180°. Therefore, this switching pattern is often referred to as three-phase

180° conduction mode. Resulting line-to-neutral voltage waveforms of this switching pattern are plotted in Figure 2-7.

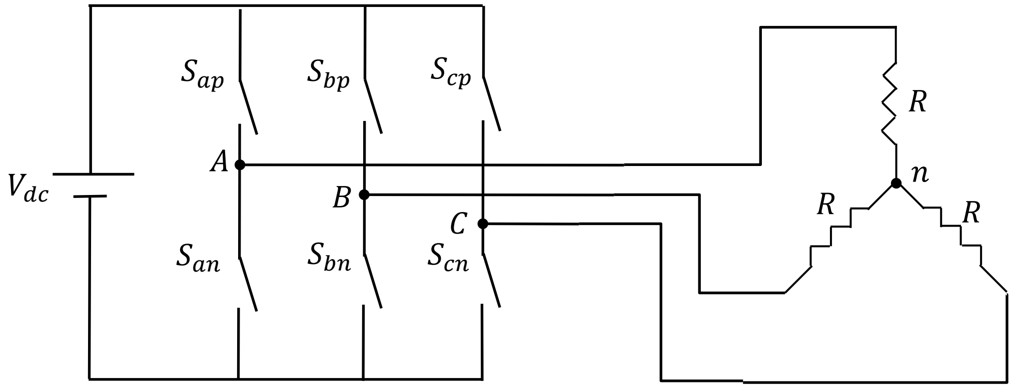

Figure 2-6: Three-Phase VSI Connected to a Y Load

Table 2-1: Three-Phase 180° Conduction Mode Switching Pattern

$S_a\, S_b\, S_c$	v_{an}	v_{bn}	v_{cn}
1 0 0	$\frac{2}{3}V_{dc}$	$-\frac{1}{3}V_{dc}$	$-\frac{1}{3}V_{dc}$
1 1 0	$\frac{1}{3}V_{dc}$	$\frac{1}{3}V_{dc}$	$-\frac{2}{3}V_{dc}$
0 1 0	$-\frac{1}{3}V_{dc}$	$\frac{2}{3}V_{dc}$	$-\frac{1}{3}V_{dc}$
0 1 1	$-\frac{2}{3}V_{dc}$	$\frac{1}{3}V_{dc}$	$\frac{1}{3}V_{dc}$
0 0 1	$-\frac{1}{3}V_{dc}$	$-\frac{1}{3}V_{dc}$	$\frac{2}{3}V_{dc}$
1 0 1	$\frac{1}{3}V_{dc}$	$-\frac{2}{3}V_{dc}$	$\frac{1}{3}V_{dc}$

Produced voltage waveforms in Figure 2-7 contain numerous amounts of harmonics at frequencies close to the fundamental frequency, thereby requiring a large filter to eliminate these harmonics. In addition, the magnitude of the output voltage can only be controlled by the input voltage V_{dc}, which is impractical in RES applications. One way of overcoming these problems is implementation of SVPWM. To understand SVPWM, consider Figure 2-8 where the switching states in Table 2-1 are represented geometrically. The DC source V_{dc} is moving via discrete steps

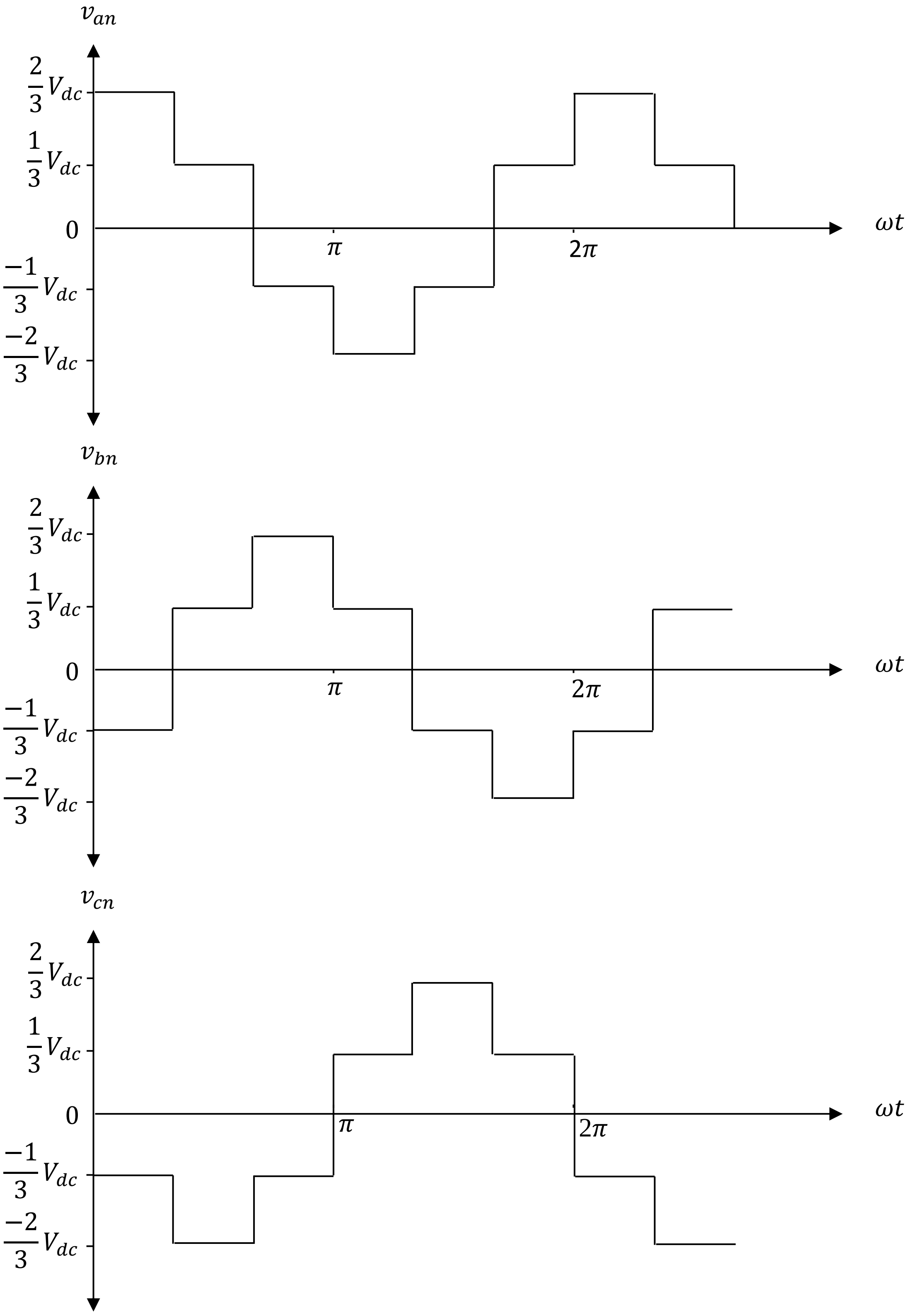

Figure 2-7: Three-Phase 180° Conduction Mode Switching Pattern

of $\frac{T}{6}$ (T is the fundamental period) from one switching state to the next at a speed of ωt, where $\omega = 2\pi f$. Switching states 000 and 111 are located at the center and referred to as the zero switching states because they produce zero output voltage. As determined by Figure 2-8 V_{dc} forms a hexagonal contour, the dotted hexagon. In order to synthesize a sinusoidal-like voltage waveform, a moving reference space vector able to form a circular contour must be defined. The reference space vector represents the following phase voltages:

$$v_a = V_m \sin(\omega t) \tag{2-9}$$

$$v_b = V_m \sin(\omega t + \frac{2\pi}{3}) \tag{2-10}$$

$$v_c = V_m \sin\left(\omega t - \frac{2\pi}{3}\right) \tag{2-11}$$

Thus, the new space vector can be expressed in terms of phase voltages as:

$$\overrightarrow{v_s} = \frac{2}{3}\{V_m + \alpha V_m + \alpha^2 V_c\} \tag{2-12}$$

where α is a shifting operator defined as:

$$\alpha = e^{j\frac{2\pi}{3}} \tag{2-13}$$

Table 2-2 provides values of $\overrightarrow{v_s}$ corresponding to each switching state using values presented in Table 2-1. These values of $\overrightarrow{v_s}$ are referred to as active switching vectors, $\overrightarrow{v_1}$ to $\overrightarrow{v_6}$ and are presented geometrically in Figure 2-9(a). As mentioned, $\overrightarrow{v_s}$ must resemble circular contour to ensure sinusoidal output voltage waveforms. Therefore, when $\overrightarrow{v_s}$ falls between two switching vectors, it can be synthesized by weighted averaging of the two switching vectors and one of the zero vectors. For example, $\overrightarrow{v_s}$ in Figure 2-9 is falling between $\overrightarrow{v_1}$ and $\overrightarrow{v_2}$ and the instantaneous value of $\overrightarrow{v_s}$ synthesized over one switching cycle T_s can be written as:

$$\hat{v}_s = \frac{1}{T_s}[d_1 T_s v_1 + d_2 T_s v_2 + d_0 T_s v_0] \tag{2-14}$$

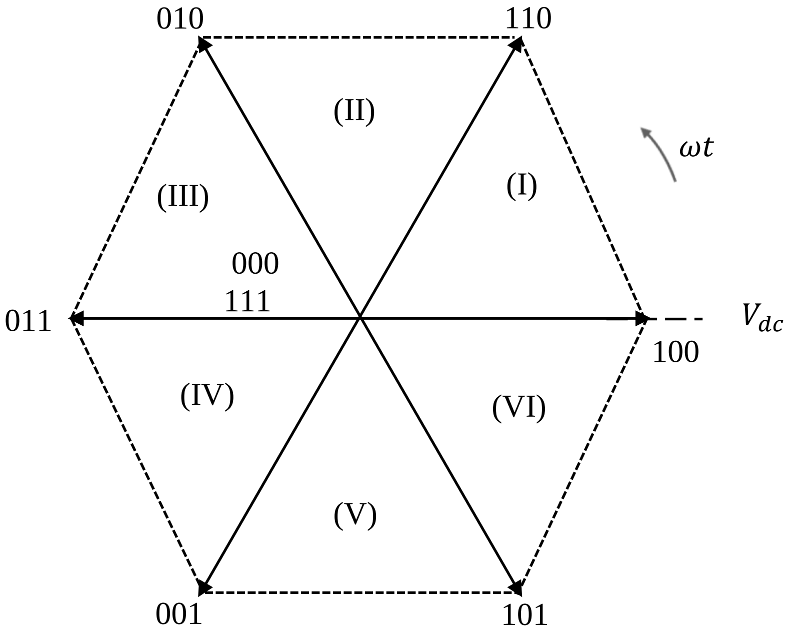

Figure 2-8: Space Vector Representation of the 180° Conduction Mode Switching Pattern

Table 2-2: Space Vector Values

$\boldsymbol{S_a S_b S_c}$	$\vec{v}_{s}$	**Value**
1 0 0	v_1	$\frac{2}{3}V_{dc}e^{j0}$
1 1 0	v_2	$\frac{2}{3}V_{dc}e^{j\frac{2\pi}{3}}$
0 1 0	v_3	$\frac{2}{3}V_{dc}e^{j\frac{\pi}{3}}$
0 1 1	v_4	$\frac{2}{3}V_{dc}e^{j\frac{4\pi}{3}}$
0 0 1	v_5	$\frac{2}{3}V_{dc}e^{j\frac{5\pi}{3}}$
1 0 1	v_6	$\frac{2}{3}V_{dc}e^{j\pi}$

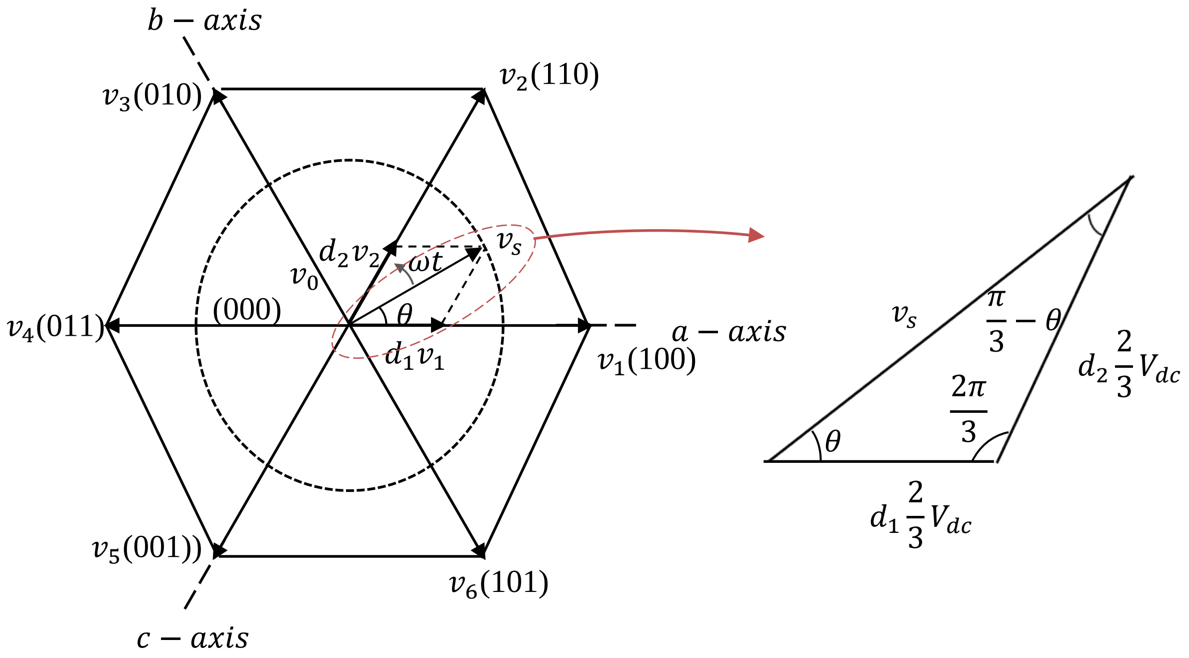

(a) (b)

Figure 2-9: SVPWM Geometrical Representation

v_0 is a zero vector and it could be represented by either 111 or 000 switching states while d_1, d_2,and d_0 are the switching cycle duty ratios corresponding to v_1, v_2,and v_0, respectively. Therefore, the duty ratios satisfy the following equation:

$$d_1 + d_2 + d_0 = 1 \tag{2-15}$$

From (2-15) an expression for d_0 can be derived in terms of $d_1$and d_2 as follows:

$$d_0 = 1 - (d_1 + d_2) \tag{2-16}$$

Expressions for d_1 and d_2 can be derived from the triangle extracted from Figure 2-9(a) and presented in Figure 2-9(b). Applying the rule of sines to the triangle in Figure2-9(b) yields the following equation:

$$\frac{v_s}{\sin(\frac{2\pi}{3})} = \frac{d_1 \frac{2}{3} V_{dc}}{\sin(\frac{\pi}{3} - \theta)} = \frac{d_2 \frac{2}{3} V_{dc}}{\sin(\theta)} \tag{2-17}$$

Consequently, the following expressions for $d_1$and d_2 are obtained:

$$d_1 = \sqrt{3}\,\frac{v_m}{V_{dc}}\sin(\frac{\pi}{3} - \theta) \tag{2-18}$$

$$d_2 = \sqrt{3}\,\frac{v_m}{V_{dc}}\sin(\theta) \tag{2-19}$$

v_m is the magnitude of the phase-to-neutral voltage. Therefore (2-18) and (2-19) can be expressed in terms of line-to-line voltages:

$$d_1 = \frac{v_{LL}}{V_{dc}}\sin\left(\frac{\pi}{3} - \theta\right) = m\sin\left(\frac{\pi}{3} - \theta\right) \tag{2-20}$$

$$d_2 = \frac{v_{LL}}{V_{dc}}\sin(\theta) = m\sin(\theta) \tag{2-21}$$

The ratio $\frac{v_{LL}}{V_{dc}}$ is referred to as the modulation index m and is used to control output voltage by controlling the length of the space vector v_s. Moreover, expressions in (2-20) and (2-21) are valid for Sector I. Therefore the following expressions for $d_1$and d_2 are derived in terms of the number of Sector i and the modulation index, m:

$$d_1 = msin(\frac{\pi}{3} - \theta - (i-1)\frac{\pi}{3}) \tag{2-22}$$

$$d_2 = msin(\theta - (i-1)\frac{\pi}{3}) \tag{2-23}$$

To find maximum possible output voltage, maximum length of v_s must be calculated. Maximum length of v_s is the radius of the largest circular contour within the hexagon representing the switching vectors, as shown in Figure 2-10(a). This figure shows that when v_s is at its maximum length, it lies perpendicularly on the straight line connecting any two adjacent active switching vectors and it forms the triangle in Figure 2-10(b).

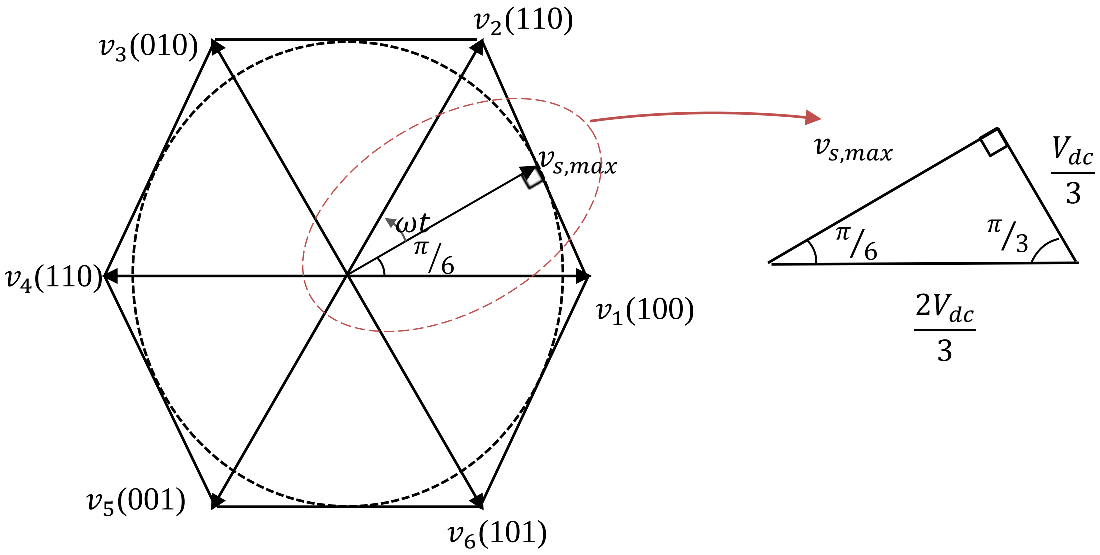

Figure 2-10: Maximum Length of the State-Space Vector v_s

From Figure 2-10(b), an expression for $v_{s,max}$ can be calculated as follows:

$$\cos\left(\frac{\pi}{6}\right) = \frac{v_{s,max}}{2V_{dc}/_{3}} \longrightarrow v_{s,max} = \frac{V_{dc}}{\sqrt{3}} \tag{2-24}$$

v_s represents phase voltage magnitude. To obtain the RMS line-to-line voltage (2-24) is multiplied by $\frac{\sqrt{3}}{\sqrt{2}}$:

$$v_{LL(RMS),max} = \frac{V_{dc}}{\sqrt{2}} \tag{2-25}$$

A more general line-to-line expression in terms of m is given below:

$$v_{LL} = m\frac{V_{dc}}{\sqrt{2}} \tag{2-26}$$

2.4 Conclusion and Closing Remarks

Three commonly used PWM techniques were discussed in this chapter. Because of its simplicity and ease of implementation, SPWM has been one of the most attractive PWM techniques. However, SPWM does not fully utilize the DC bus voltage, so third-harmonic injection was introduced. Third-harmonic injection PWM is implemented similarly to SPWM and it has better utilization of the DC bus voltage, approximately 15.5 % increase. Although it has been regarded as a complex technique, SVPWM, unlike SPWM and third-harmonic injection PWM, does not require comparison of three reference signals to a high frequency carrier signal. Instead, only one reference vector representing three-phase voltage signals is needed. Maximum RMS line-to-line output voltage that can be produced using SVPWM is $v = \frac{V_{dc}}{\sqrt{2}}$ when m = 1, 15.5% increase over SPWM. Therefore, SVPWM and third-harmonic injection have identical utilization of DC bus voltage.

Because switches in any leg of the three-phase inverter work complimentarily, a delay between the upper and lower switches is typically implemented. This delay is sometimes referred to as "dead-time" or "blanking time." Practical non-idealities in switches require such delay. In fast switching devices such as IGBTs, the dead-time period could be as little as 2 μs and the effect is insignificant. In slow switching devices, however, the dead-time period is longer and the effect has more significant impact on the performance of the VSI [6].

Chapter 3 - Modeling of Power Electronics Converters

Over the past few decades, the use of power electronics converters (PECs) has grown exponentially. From laptop adaptors to aircraft on-board power systems, power converters are altering the way electricity is used. To adapt to these changes, dynamic models that describe the behavior of these systems are needed. Such models are used to assess the performance of PECs and design robust control systems for purposes such as direct power control systems and voltage-regulation systems. Over the years, various approaches have been proposed to tackle the issue of modeling different topologies of PECs. Two modeling methods seem to dominate the literature:

1. Black-box method [7] [8] [9] [10]
2. State-space averaging method [11] [12] [13] [14] [15]

In this chapter, the black-box method and the state-space averaging method are thoroughly investigated in Section 3.1 and 3.2, respectively. For simplicity and because VSI modeling examples require lengthy description, illustrative modeling examples provided in this chapter are DC-DC converters examples. However, modeling of the three-phase SVPWM VSI is thoroughly discussed in Chapter 4. Throughout this chapter, the reader will realize that these techniques can be extended to model any type of PECs. In addition to Section 3.1 and 3.2, this chapter contains two more sections. Section 3.3 discusses the reference-frame theory as it is used in Chapter 4, and Section 3.4 contains the conclusion and closing remarks of this chapter.

3.1 Black-Box Method

The Black-box modeling method, also known as behavioral modeling method, is a system level [9] experiment-based modeling method used primarily by system engineers [8]. Need for this method arose from the fact that, in some cases, PECs internal parameters are unknown for various reasons such as manufacturer confidentiality [9]. Instead, the only available data is voltage and current measurements at the input and output ports. The black-box method was first introduced to model DC-DC converters [8]. It models DC-DC converters as non-terminated two-port networks, or G parameters models, in which input is represented by a Norton equivalent circuit and the output is represented by a Thevnin equivelant circuit, as shown in Figure 3-1.

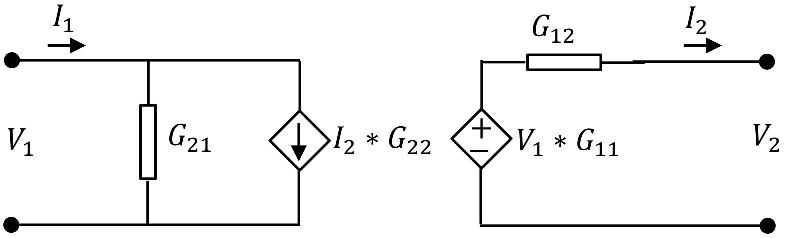

Figure 3-1: None-Terminated Two-Port Network Representation of DC-DC Converter

Input variables of the model shown in Figure 3-1 are output current I_2 and input voltage V_1, and output variables are the input current I_2 and the output voltage V_2. The transfer functions, or G_{ij} parameters, are obtained from direct voltage and current measurements and are defined as follows:

$$G_{11} = \frac{V_2}{V_1}|_{I_2=0} \tag{3-1}$$

$$G_{12} = \frac{V_2}{I_2}|_{V_1=0} \tag{3-2}$$

$$G_{21} = \frac{I_1}{V_1}|_{I_2=0} \tag{3-3}$$

$$G_{22} = \frac{I_1}{I_2}|_{V_1=0} \tag{3-4}$$

Consequently, the input-output relationship can be written as:

$$\begin{bmatrix} V_2 \\ I_1 \end{bmatrix} = \begin{bmatrix} G_{11} & G_{12} \\ G_{21} & G_{22} \end{bmatrix} \begin{bmatrix} V_1 \\ I_2 \end{bmatrix} \tag{3-5}$$

The model in (3-5) is based on two assumptions: *1)* the DC-DC converter is only slightly non-linear *2)* the four transfer functions, also referred to as G_{ij} parameters, are sufficient to capture the dynamics and frequency response of the DC-DC converter. The next step of model development is application of broad-band sinusoidal functions to the DC-DC converter and acquisition of voltage and current measurements. A network analyzer such as Agilent 4395 A is used to complete this task [8]. After acquiring a sufficient amount of data, frequency responses representing the G_{ij} are obtained and fitted to transfer functions. The process of fitting data to transfer functions is referred to as “system identification.” Various approaches are utilized to perform this task. The most convenient approach is to use a software package such as the system identification toolbox by Matlab.

In addition to not requiring any prior knowledge of the internal parameters of the PEC, the black-box method does not require prior knowledge of the PEC topology. Therefore, the model in Figure 3.1 can be used to model any type of DC-DC converter. Experimental data of a buck-converter were obtained and used to fit the model given in Figure 3.1. Verification of the model and a detailed approach of the use of the black-box method are presented in [8]. Using $dq0$ transformation (discussed in Section 3.3) to transform balanced three-phase rotating quantities to two DC quantities, the black-box method discussed in [8] was extended to develop a small-signal model of a three-phase inverter of an unknown topology in in [10]. In both papers [8] [10], the developed models successfully describe the behavior of their corresponding systems, although the development of a large-signal model of three-phase VSI using the black-box method requires further investigation [10].

However, this method has three primary disadvantages. First, this method is only applicable on a case-by-case basis. Meaning, if two PECs have the same topology but the internal parameters are different, then a model developed for one may not necessarily work for the other. Therefore, two experiments may be needed to develop two different models. Second, since this method does not require the knowledge of internal parameters, the developed model cannot assess the performance of the overall system with respect to any variation in the internal parameters, i.e., eigenvalues sensitivity analysis cannot be carried out using black-box developed models. Third, since this is an experiment-based method, accuracy of developed models depends on accuracy of the experimentally obtained data. Thus, error in measurements caused by EMI or other factors will hinder the accuracy of the developed model.

3.2 State-Space Averaging Method

The State-space averaging method was introduced in 1976 as a dynamic modeling tool for DC-DC converters [11] but was later used for other types of PECs such as inverters and rectifiers [12] [13] [14] [15]. The state-space averaging method is based on averaging multiple linear time-varying state-space representations [16] of a periodic system over one period. In state-space representation, any set of linear equations describing a dynamic system with n variables, r inputs, and m outputs can be represented in matrix form as follows:

$$\dot{x} = Ax + Bu \tag{3-6}$$

$$y = Cx + Du \tag{3-7}$$

$A, B, C,$ and, D are matrices of $n \times n, n \times r, m \times n,$ and, $m \times r,$ respectively. In systems like PECs, multiple linear time-varying state-space representations are needed to fully model the system over one switching period. The state-space averaging method was introduced to tackle these issues.

To illustrate the application of this method, consider the DC-DC boost converter in Figure 3-2. Over one switching period T_s, the switch sw is closed for a period of dT_s ,where d is the duty ratio, and opened for a period of $(1 - d)\, T_s$. Figure 3-3(a) and Figure 3-3(b) show the two linear circuits representing DC-DC boost converter over one switching cycle T_s. For the circuit in Figure 3-3(a), the following equations can be obtained using KVL and KCL:

$$V_{dc} + L\frac{di}{dt} = 0 \tag{3-8}$$

$$C\frac{dv_o}{dt} - \frac{v_0}{R_L} = 0 \tag{3-9}$$

Similarly, the following equations can be obtained for the circuit in Figure 3.3 (b):

$$V_{dc} + L\frac{di}{dt} + v_o = 0 \tag{3-10}$$

$$i - C\frac{dv_o}{dt} - \frac{v_0}{R_L} = 0 \tag{3-11}$$

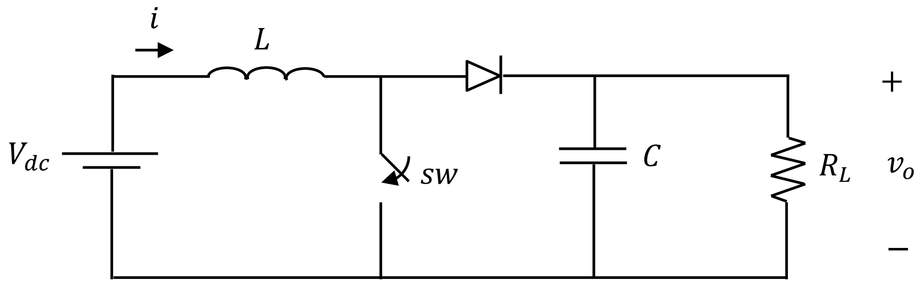

Figure 3-2: DC-DC Boost Converter

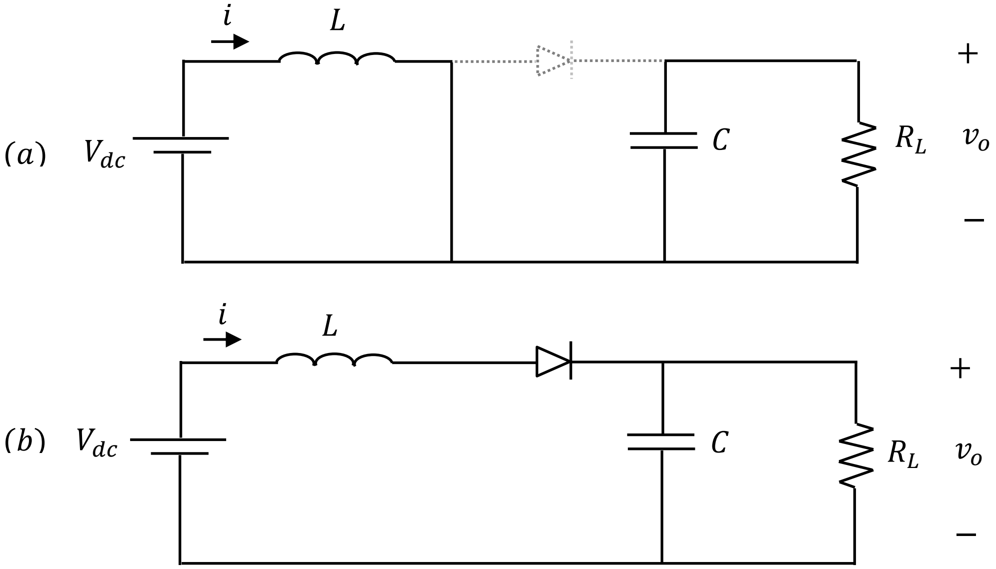

Figure 3-3: DC-DC Boost Converter Operation Over One Switching Cycle

Arranging the above equation in matrix form yields the following two state-space representation for the circuits in Figure 3-3(a) and Figure 3-3 (b), respectively:

$$\frac{d}{dt}\begin{bmatrix} i \\ v_o \end{bmatrix} = \begin{bmatrix} 0 & 0 \\ 0 & \frac{1}{CR_L} \end{bmatrix}\begin{bmatrix} i \\ v_o \end{bmatrix} + \begin{bmatrix} \frac{-1}{L} \\ 0 \end{bmatrix}[V_{dc}] \tag{3-12}$$

$$\frac{d}{dt}\begin{bmatrix} i \\ v_o \end{bmatrix} = \begin{bmatrix} 0 & \frac{-1}{L} \\ \frac{1}{C} & \frac{1}{CR_L} \end{bmatrix}\begin{bmatrix} i \\ v_o \end{bmatrix} + \begin{bmatrix} \frac{-1}{L} \\ 0 \end{bmatrix}[V_{dc}] \tag{3-13}$$

For notation simplicity, (3-12) and (3-13) can be written as:

$$\dot{x} = A_{ON}\,x + Bu \tag{3-14}$$

$$\dot{x} = A_{OFF}\,x + Bu \tag{3-15}$$

where,

$$x = \begin{bmatrix} i \\ v_o \end{bmatrix},\ A_{ON} = \begin{bmatrix} 0 & 0 \\ 0 & \frac{1}{CR_L} \end{bmatrix},\ A_{OFF} = \begin{bmatrix} 0 & \frac{-1}{L} \\ \frac{1}{C} & \frac{1}{CR_L} \end{bmatrix},\ B = \begin{bmatrix} \frac{-1}{L} \\ 0 \end{bmatrix}, \text{and } u = \ [V_{dc}] \tag{3-16}$$

According to the state-space averaging method, state-space models in in (3-14) and (3-15) can be averaged over T_s. Since the control matrix B is identical in (3-14) and (3-15), only state matrices A_{ON} and A_{OFF} are averaged as follows:

$$\tilde{A} = dA_{ON} + (1-d)A_{OFF} = \begin{bmatrix} 0 & \frac{-(1-d)}{L} \\ \frac{(1-d)}{C} & \frac{1}{CR_L} \end{bmatrix} \tag{3-17}$$

Using (3-17), the DC-DC converter in Figure 3.2 can be represented by a single linear time-invariant state-space representation as follows:

$$\dot{\tilde{x}} = \tilde{A}\,x + Bu \tag{3-18}$$

In (3-17) the duty ratio d is considered a constant parameter. However, in practice, d is a variable input used to regulate output voltage of the converter. To model d as a variable input, a small-signal model must be derived where (3-18) is linearized around specific steady-state operating points and a small perturbation is added to the systems state variables, input, and d such that:

$$\dot{x} = \dot{X} + \delta\dot{x} \tag{3-19}$$

$$V_{dc} = \ V_{DC} + \delta V_{dc} \tag{3-20}$$

$$d = D + \ \delta d \tag{3-21}$$

Where, $\dot{X} = [I\ \ V_o]^T$, V_{DC}, and D are the steady-state operating points and δ symbolizes a small perturbation. Applying (3-19)-(3-21) to the state-space averaged model in (3-18) yields:

$$\frac{d}{dt}\begin{bmatrix}\delta i \\ \delta v_o\end{bmatrix} = \begin{bmatrix} 0 & \frac{-(1-D)}{L} \\ \frac{1-D}{C} & \frac{-1}{CR_L} \end{bmatrix}\begin{bmatrix}\delta i \\ \delta v_o\end{bmatrix} + \begin{bmatrix} \frac{1}{L} & \frac{V_o}{L} \\ 0 & \frac{-I}{CR_L} \end{bmatrix}\begin{bmatrix}\delta V_{dc} \\ \delta d\end{bmatrix} \tag{3-22}$$

To demonstrate effectiveness of the large-signal averaged state-space model in (3-18) and the small-signal averaged state-space model in (3-22), a Matlab/Simulink simulation of a DC-DC boost converter with a switching frequency of 20 kHz was carried out and compared against the averaged models. The large-signal parameters are given in Table 3-1 and steady-state operating points used to linearize the small-signal model are given Table 3-2. Simulation results of the large-signal model and the small signal model are presented in Figure 3-4 and Figure 3-5, respectively. In Figure 3-5, the input V_{dc} is decreased by 1 V at $t = 6\,ms$. Then, at $t = 11\,ms$,the duty ratio d was increased from 0.5 to 0.546.

Table 3-1: Large-Signal Model Parameters

Parameter	Value
V_{dc}	12 V
v_o	24 V
d	0.5
L	200 mH
C	47 uF
R_L	10 Ω

Table 3-2: Steady-State Operating Points

Parameter	Value
V_{DC}	12 V
V_o	24 V
D	0.5
I	7.2 A

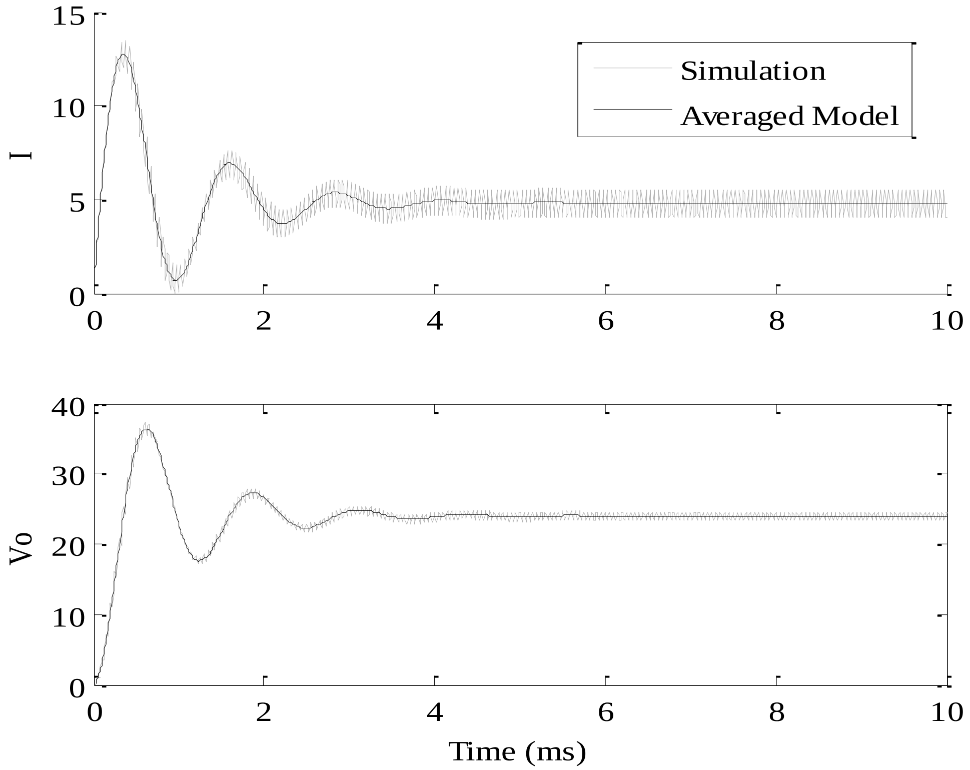

Figure 3-4: Boost Converter Simulation Compared Against Averaged-State-Space Model (Large-Signal)

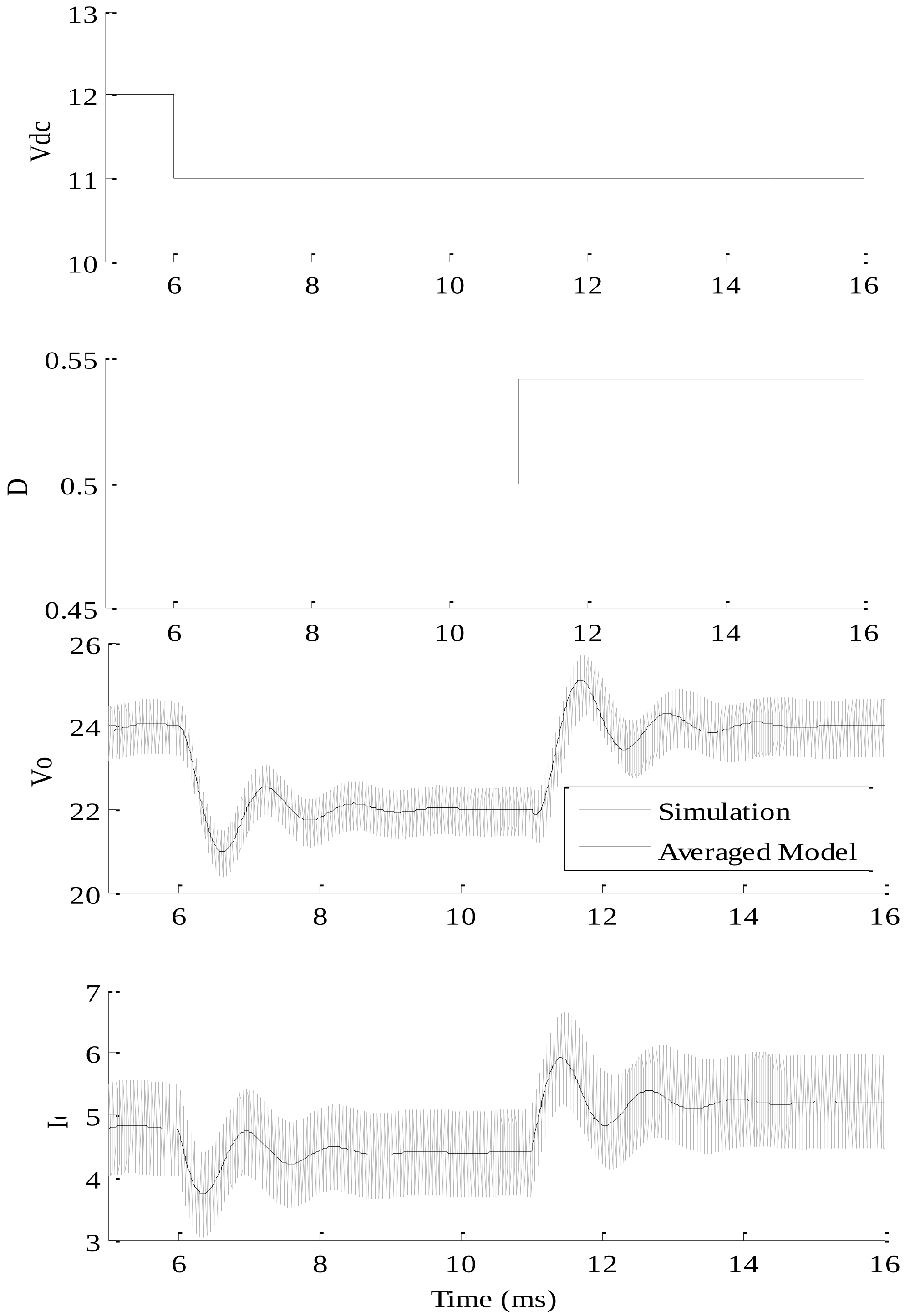

Figure 3-5: Boost Converter Simulation Compared Against Averaged-State-Space Model (Small-Signal)

3.3 Reference-Frame Theory

Transforming rotating AC electrical quantities into constant DC quantities is commonly used to simplify analysis and control of electric machines, power systems, and PECs. One of the most commonly used transformations is the $dq0$ transformation [17] represented geometrically in Figure 3-6.

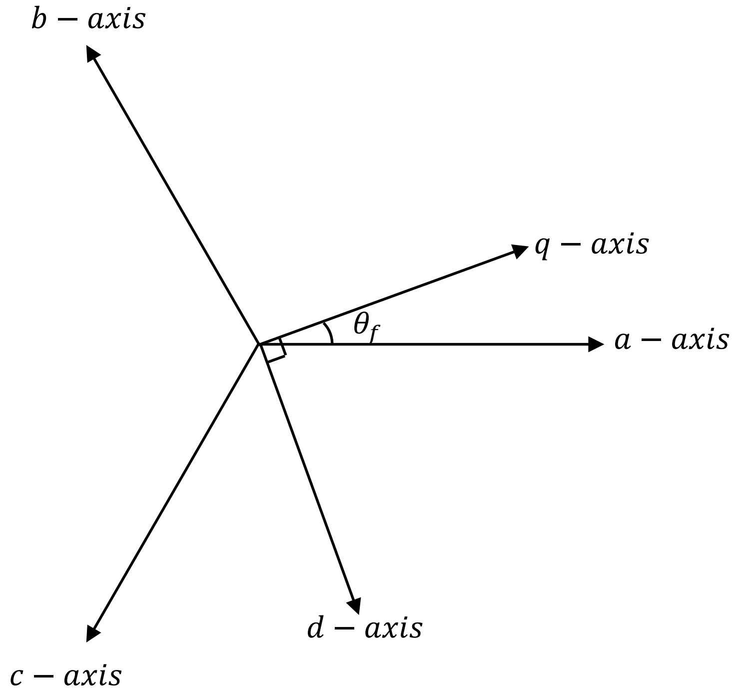

Figure 3-6: dq Transformation Representation in Space Vector

The d and the q quantities are represented by the sum of projections of rotating quantities on the d and the q axis, respectively. The 0 component, however, is the summation of the three rotating quantities. Since the 0 component is always equal to zero for three-phase balanced quantities, it often is not considered. Thus, the transformation reduces to dq quantities. The relationship between rotating quantities and dq quantities is given by:

$$f_{ab} = M f_{dq} \tag{3-23}$$

where,

$$f_{dq} = \begin{bmatrix} f_q \\ f_d \end{bmatrix} \tag{3-24}$$

$$M = \begin{bmatrix} cos(\theta_f) & sin(\theta_f) \\ cos\left(\theta_f - \frac{2\pi}{3}\right) & sin\left(\theta_f - \frac{2\pi}{3}\right) \end{bmatrix} \tag{3-25}$$

$$f_{ab} = \begin{bmatrix} f_a \\ f_b \end{bmatrix} \tag{3-26}$$

The dq frame can be stationary or rotating with respect the abc frame. In this thesis, dq synchronous transformation is used. In other words, the dq frame is rotating with the abc frame at the same angular speed, $\omega = 2\pi f$.

3.4 Conclusion and Closing Remarks

In this chapter, the black-box modeling method and state-space averaging method were discussed. The black-box method, a system-level modeling method used by system engineers, requires experimental results. It has the advantage of not requiring any knowledge of internal parameters or even circuit topology. But it has the disadvantage of incorporating any experimental errors into the developed model. In addition, models for specific PECs developed using this method cannot be modified to describe the behavior of other PECs with similar topologies but different internal parameters. The state-space averaging method, on the other hand, has the advantage of not requiring any experimental results or making too many prior assumptions. However, it requires complete prior knowledge of the circuit being modeled. Averaged-state-space models are internal parameters-based model. For example, if Company A and Company B manufacture DC-DC boost converters, the models given by (3-18) and (3-22) can be used to describe both converters as long as the internal parameters are known. Because averaged-state-space models are internal parameters-based models, these models can be used to carry out eigenvalues sensitivity analysis and study the stability effects of varying specific internal parameters.

The reference-frame theory, also discussed in this chapter, allows AC quantities and circuits to be represented as DC quantities, when synchronous frame of reference transformation is used. Thus, as illustrated in the Chapter 4, reference-frame theory allows DC-DC modeling methods to be extended to modeling AC systems such as the three-phase SVPWM VSI.

Chapter 4 - State-Space-Averaged Model of the Three-Phase SVPWM VSI

In this chapter, the state-space averaging technique is applied to the three-phase SVPWM VSI. Averaged-state-space models were developed for the three-phase SVPWM VSI under stand-alone and grid-tied modes. The modeling process was achieved through three steps. First, as discussed in Chapter 2, the three-phase SVPWM VSI has six active switching states and two zero switching states. Thus, state-space models representing the linear circuits corresponding to each switching state must be developed. Second, as discussed in Chapter 2, the three-phase SVPWM VSI can be represented by three linear circuits over one switching cycle T_s. These circuits represent two active switching states and a zero switching state. The state-space representation of these circuits must be averaged over T_s to yield a single averaged-state-space representation (applying the state space averaging method discussed in Chapter 3). Third, since switching states vary by sector, the averaged-state-space representations vary accordingly. Therefore, the result will be a time-variant averaged-state-space representation (six averaged-state-space representations corresponding to each sector). To replace the six averaged models by a single time-invariant model, the dq transformation into a synchronous frame of reference is applied to the six averaged-state-space representations, assuming the VSI is operating under balanced three-phase condition. Any group of instantaneous three-phase quantities at different arbitrary points in time will always converge to the same dq quantities once they undergo dq transformation into the synchronous frame of reference. Therefore, the six averaged-state-space models should converge to a single averaged-state-space model; that model can be claimed as a dynamic time-invariant model describing the three-phase SVPWM VSI.

Applying the steps described above (to stand-alone and grid-tied cases) results in large signal models. In these models, important control parameters like the modulation index of the VSI m and output voltage phase angle ϕ are considered constant. In practice, m is a variable used to regulate the output voltage and ϕ is a variable used to control the flow of power to the electric grid. Therefore, small-signal models were developed through linearization and introduction of small perturbation to the large-signal models, as discussed in Chapter 3.

Besides an overview of the chapter, this chapter contains three main sections. Section 4.1 contains derivations of the large-signal and small-signal averaged-state-space models of the three-phase SVPWM VSI under stand-alone mode. Section 4.2 contains derivations of the large-signal and small-signal averaged-state-space models of the three-phase SVPWM VSI under grid-tied mode. Section 4.3 presents a comprehensive eigenvalues sensitivity analysis of the small-signal models developed in Section 4.1 and Section 4.2.

4.1 Averaged-State-Space Model of the Three-Phase SVPWM VSI under Stand-Alone Mode

The three-phase VSI to be modeled is supplying a three-phase load through an LCL filter as shown in Figure 4-1. The LCL filter is a low pass filter included with the three-phase VSI to decrease the THD by eliminating higher frequency harmonics. For the sake of accuracy, the LCL filter is included in the modeling process. The implemented LCL filter includes a resistor, R_f, in series with the capacitor, C_f. This resistor provides a passive damping solution and it was recommended to be in the range of $0.5\ \Omega$ to $1\ \Omega$ [18]. Because many applications implement a bank of capacitors at the dc bus side of the inverter, the bank of capacitors is modeled as single capacitor, C. Moreover, the resistor R_s represent any startup pre-charging resistance or any resistance in series with the DC voltage source.

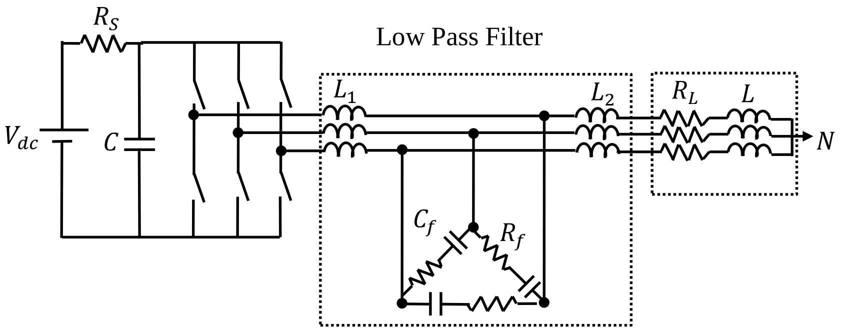

Figure 4-1: Three-Phase SVPWM VSI under Stand-Alone Mode

a) *Large-Signal Model:*

As previously mentioned, the three-phase VSI in Figure 4-1 can be represented by three-linear circuits over T_s. One linear circuit represents zero switching states and two linear circuits representing active switching states, the active switching states vary by sector. Therefore, state-space models for the linear circuits corresponding to the switching states discussed in Chapter 2, presented in Figure **2-9**(a), must be derived. For illustration purposes, the state-space model representing the zero switching states, 000 and 111, is derived in this section, and models representing the other active switching states are included in Appendix A.

The linear circuit representing the zero switching states (000 and 111), marked with the appropriate voltages and currents, is depicted in Figure 4-2. R_1 in the circuit models the ON resistance of the switches and any stray resistance between the VSI and the LCL filter.

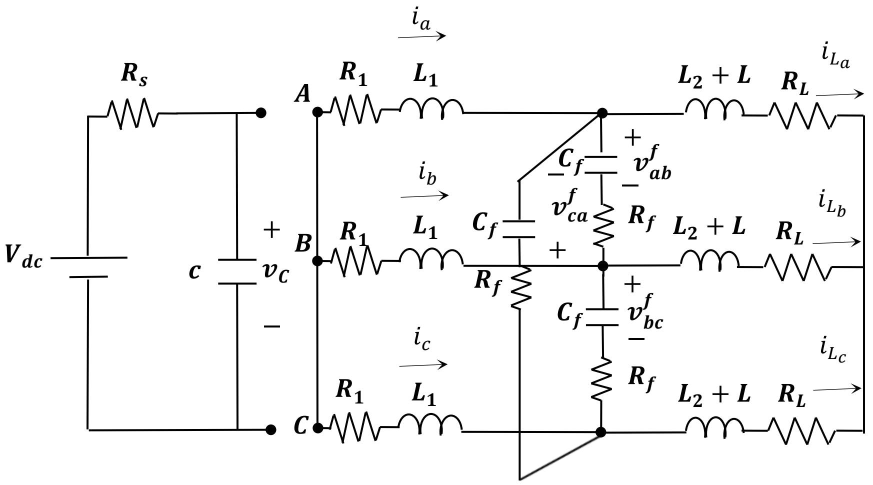

Figure 4-2: Linear Circuit Representing Zero Switching States (Stand-Alone)

Any linear circuit can be represented by a number of differential equations equal to the number of energy storage units in the circuit. However, in three-phase balanced circuits, the number of equations can be reduced by a factor of $\frac{1}{3}$ because any three-phase quantity can be expressed in terms of the other two phase quantities (for example: $x_a = -x_b - x_c$). Therefore, since currents flowing through L_1 and $L_2 + L$ andvoltages across C_f are three-phase balanced quantities only six linear differential equations representing the AC side of the VSI and one linear differential equation representing DC voltage across C are needed. Hence, linear differential equations for the state variables: v_c, i_a, i_b, v_{ab}^f, v_{bc}^f, i_{L_a}, and i_{L_b} can be derived using KVL and KCL.

First, to derive an expression for $\dot{v}_c$, the following KCL equation is developed:

$$\frac{v_c - V_{dc}}{R_s} + C\dot{v}_c = 0 \tag{4-1}$$

From (4-1) an expression for $\dot{v}_c$ can be derived as follows:

$$\dot{v}_c = \frac{V_{dc} - v_c}{CR_s} \tag{4-2}$$

Second, to derive expressions for v_{ab}^f and v_{bc}^f, the following KCL equations are developed as follows:

$$i_a - i_{L_a} - C_f\left(\dot{v}_{ab}^f - \dot{v}_{ca}^f\right) = 0 \tag{4-3}$$

$$i_b - i_{L_b} + C_f\left(\dot{v}_{ab}^f - \dot{v}_{bc}^f\right) = 0 \tag{4-4}$$

Replacing $-\dot{v}_{ca}^f$ with $\dot{v}_{ab}^f + \dot{v}_{bc}^f$ in (4-3) results in:

$$i_a - i_{L_a} - C_f\left(2\dot{v}_{ab}^f + \dot{v}_{bc}^f\right) = 0 \tag{4-5}$$

From (4-3) and (4-5), expressions for $\dot{v}_{ab}^f$and $\dot{v}_{bc}^f$ can be derived as follows:

$$\dot{v}_{ab}^f = \frac{-i_{L_a} + i_a - i_b + i_{L_b}}{3C_f} \tag{4-6}$$

$$\dot{v}_{bc}^f = \frac{-i_{L_a} + i_a + 2(i_b - i_{L_b})}{3C_f} \tag{4-7}$$

Third, to develop expressions for i_a and i_b, KVL equations for the loops formed by i_a and i_b must be derived. In order to do so, expressions for currents flowing from phase A to B through C_f and B to C through C_f must be developed. Using (4-6) and (4-7), the following current equations are derived:

$$i_{a\ to\ b} = C_f \dot{v}_{ab}^f = \frac{-i_{L_a} + i_a - i_b + i_{L_b}}{3} \tag{4-8}$$

$$i_{b\ to\ c} = C_f \dot{v}_{bc}^f = \frac{-i_{L_a} + i_a + 2(i_b - i_{L_b})}{3} \tag{4-9}$$

Using (4-8) and (4-9) the following KVL equations are derived:

$$R_1(i_a - i_b) + L_1(\dot{i}_a - \dot{i}_b) + v_{ab}^f + \left(\frac{i_a - i_{L_a} - i_b + i_{L_b}}{3}\right) R_f = 0 \tag{4-10}$$

$$R_1(2i_b + i_a) + L_1(2\dot{i}_b + \dot{i}_a) + v_{bc}^f + \left(\frac{i_a - i_{L_a} + 2\left(i_b - i_{L_b}\right)}{3}\right) R_f = 0 \tag{4-11}$$

From (4-10) and (4-11) the following expressions for $\dot{i}_a$ and $\dot{i}_b$ are derived as follows:

$$\dot{i}_a = \frac{-3R_1 i_a - 2v_{ab}^f - v_{bc}^f + \left(i_{L_a} - i_a\right) R_f}{3L_1} \tag{4-12}$$

$$\dot{i}_b = \frac{-3R_1 i_b + v_{ab}^f + \left(i_{L_b} - i_b\right) R_f - v_{bc}^f}{3L_1} \tag{4-13}$$

Finally, to derive expressions for $\dot{i}_{L_a}$ and $\dot{i}_{L_b}$ KVL equations for the loops formed by i_{L_a} and $i_{L_b}$are developed as follows:

$$v_{ab}^f + \frac{(i_a - i_{L_a} - i_b + i_{L_b})}{3} R_{ac} = R_L\left(i_{L_a} - i_{L_b}\right) + (L_2 + L)\left(\dot{i}_{L_a} - \dot{i}_{L_b}\right) \tag{4-14}$$

$$v_{bc}^f + \frac{i_a - i_{L_a} + 2(i_b - i_{L_b})}{3} R_{ac} = R_L\left(2i_{L_b} + i_{L_a}\right) + (L_2 + L)\left(2\dot{i}_{L_b} + \dot{i}_{L_a}\right) \tag{4-15}$$

Solving for $\dot{i}_{L_a}$ and $\dot{i}_{L_b}$, yields:

$$\dot{i}_{L_a} = \frac{2v_{ab}^f + R_f\left(i_a - i_{L_a}\right) + v_{bc}^f - 3R_L i_{L_a}}{3(L_2 + L)} \tag{4-16}$$

$$i_{L_b} = \frac{v_{bc}^{f} + R_f\left(i_b - i_{L_b}\right) - v_{ab}^{f} - 3R_L i_{L_b}}{3(L_2 + L)} \tag{4-17}$$

Arranging the above expressions for the aforementioned state variables and recognizing V_{dc} as the systems input, yields the following state space representation for the zero switching states:

$$\dot{x} = A_{000}\, x + Bu \tag{4-18}$$

where,

$$x = \begin{bmatrix} v_c \\ i_a \\ i_b \\ v_{ab}^{f} \\ v_{bc}^{f} \\ i_{L_a} \\ i_{L_b} \end{bmatrix} \tag{4-19}$$

$$A_{000} = \begin{bmatrix} \frac{-1}{CR_s} & 0 & 0 & 0 & 0 & 0 & 0 \\ 0 & \frac{-(3R_1+R_f)}{3L_1} & 0 & \frac{-2}{3L_1} & \frac{-1}{3L_1} & \frac{R_f}{3L_1} & 0 \\ 0 & 0 & \frac{-(3R_1+R_f)}{3L_1} & \frac{1}{3L_1} & \frac{-1}{3L_1} & 0 & \frac{R_f}{3L_1} \\ 0 & \frac{1}{3C_f} & \frac{-1}{3C_f} & 0 & 0 & \frac{-1}{3C_f} & \frac{1}{3C_f} \\ 0 & \frac{1}{3C_f} & \frac{2}{3C_f} & 0 & 0 & \frac{-1}{3C_f} & \frac{-2}{3C_f} \\ 0 & \frac{R_f}{3(L_2+L)} & 0 & \frac{2}{3(L_2+L)} & \frac{1}{3(L_2+L)} & \frac{-3R_L-R_f}{3(L_2+L)} & 0 \\ 0 & 0 & \frac{R_f}{3(L_2+L)} & \frac{-1}{3(L_2+L)} & \frac{1}{3(L_2+L)} & 0 & \frac{-3R_L-R_f}{3(L_2+L)} \end{bmatrix} \tag{4-20}$$

$$B = \begin{bmatrix} \frac{1}{CR_s} \\ 0 \\ 0 \\ 0 \\ 0 \\ 0 \\ 0 \end{bmatrix} \tag{4-21}$$

The model in (4-18) represents only the operation of the three-phase SVPWM VSI during the portion of the switching cycle T_s corresponding to the duty ratio d_0. To derive a comprehensive model, the state-space averaging method must be applied to the zero switching state and two active states as follow:

$$\tilde{\dot{x}} = \bar{A}x + Bu \tag{4-22}$$

where $\bar{A}$ is defined as follow:

$$\bar{A} = d_0A_0 + d_1A_1 + d_2A_2 \tag{4-23}$$

In (4-22) the state matrix A is averaged while the control matrix B is not because B is constant for every switching state. Therefore, B does not need to be averaged. In addition, the definition of the averaged state matrix A in (4-23) results in different matrix for each sector. Therefore, six state-space representations are obtained and included in Appendix A. The result of (4-22) for Sector I is defined as follows:

$$\tilde{\dot{x}} = \bar{A}_I\tilde{x} + Bu \tag{4-24}$$

where,

$$\bar{A}_I = d_0A_{000} + d_1A_{100} + d_2A_{110} \tag{4-25}$$

$$\bar{A}_I = \begin{bmatrix} \frac{-1}{CR_s} & \frac{-(d_1+d_2)}{C} & \frac{-d_2}{C} & 0 & 0 & 0 & 0 \\ \frac{2d_1+d_2}{3L_1} & \frac{-(3R_1+R_f)}{3L_1} & 0 & \frac{-2}{3L_1} & \frac{-1}{3L_1} & \frac{R_f}{3L_1} & 0 \\ \frac{-d_1+d_2}{3L_1} & 0 & \frac{-(3R_1+R_f)}{3L_1} & \frac{1}{3L_1} & \frac{-1}{3L_1} & 0 & \frac{R_f}{3L_1} \\ 0 & \frac{1}{3C_f} & \frac{-1}{3C_f} & 0 & 0 & \frac{-1}{3C_f} & \frac{1}{3C_f} \\ 0 & \frac{1}{3C_f} & \frac{2}{3C_f} & 0 & 0 & \frac{-1}{3C_f} & \frac{-2}{3C_f} \\ 0 & \frac{R_f}{3(L_2+L)} & 0 & \frac{2}{3(L_2+L)} & \frac{1}{3(L_2+L)} & \frac{-3R_L-R_f}{3(L_2+L)} & 0 \\ 0 & 0 & \frac{R_f}{3(L_2+L)} & \frac{-1}{3(L_2+L)} & \frac{1}{3(L_2+L)} & 0 & \frac{-3R_L-R_f}{3(L_2+L)} \end{bmatrix} \tag{4-26}$$

As previously discussed, (4-24) and any of the other averaged-state-space representations for the other sectors can represent three-phase VSI operating in any sector once transformed into a synchronous dq frame of reference. To transform (4-24) into a synchronous dq frame of reference, the rotating quantities in (4-24) are grouped together in sub matrices and the result is presented as follows:

$$\frac{d}{dt}\begin{bmatrix} v_c \\ \boldsymbol{i} \\ \boldsymbol{v}_{LL}^{f} \\ \boldsymbol{i}_{L} \end{bmatrix} = \begin{bmatrix} \bar{A}_I(1,1) & \bar{A}_I(1,2:3) & 0_{1x2} & 0_{1x2} \\ \bar{A}_I(2:3,1) & \bar{A}_I(2:3,2:3) & \bar{A}_I(2:3,4:5) & \bar{A}_I(2:3,6:7) \\ 0_{2x1} & \bar{A}_I(4:5,2:3) & 0_{2x2} & \bar{A}_I(4:5,6:7) \\ 0_{2x1} & \bar{A}_I(6:7,2:3) & \bar{A}_I(6:7,4:5) & \bar{A}_I(6:7,6:7) \end{bmatrix}\begin{bmatrix} v_c \\ \boldsymbol{i} \\ \boldsymbol{v}_{LL}^{f} \\ \boldsymbol{i}_{L} \end{bmatrix} + \begin{bmatrix} B(1,1) \\ 0_{2x1} \\ 0_{2x1} \\ 0_{2x1} \end{bmatrix} u \tag{4-27}$$

where, $\boldsymbol{i} = \begin{bmatrix} i_a \\ i_b \end{bmatrix}$, $\boldsymbol{v}_{LL}^{f} = \begin{bmatrix} v_{ab}^{f} \\ v_{bc}^{f} \end{bmatrix}$, and $\boldsymbol{i}_{L} = \begin{bmatrix} i_{L_a} \\ i_{L_b} \end{bmatrix}$

To transform rotating variables of the RHS of equation (4-27), the dq transformation discussed in Chapter 3, equation (3-23), can be used. However, transforming the rotating variables on the LHS requires the derivation of (3-23) with respect to time, since the variables on the LHS are derivatives of time. Therefore, the derivation of (3-23) with respect to time is defined as follows:

$$\frac{d}{dt}f_{ab} = (\frac{d}{dt}M)f_{qd} + M(\frac{d}{dt}f_{qd}) \tag{4-28}$$

where,

$$\frac{d}{dt}M = \begin{bmatrix} -\dot{\theta}_f\sin(\theta_f) & \dot{\theta}_f\cos(\theta_f) \\ -\dot{\theta}_f\sin(\theta_f - \frac{2\pi}{3}) & -\dot{\theta}_f\cos(\theta_f - \frac{2\pi}{3}) \end{bmatrix} \tag{4-29}$$

Using (3-23) to replace the rotating variables in the RHS of (4-27) with their corresponding dq quantities, $\frac{d}{dt}v_c$ can be expressed as:

$$\frac{d}{dt}v_c = \bar{A}_I(1,1)v_c + \bar{A}_I(1,2:3)M\boldsymbol{i}_{qd} + B(1,1)u \tag{4-30}$$

where, $\boldsymbol{i_{qd}} = \begin{bmatrix} i_q \\ i_d \end{bmatrix}$

Next, using (4-28) to replace the LHS and (3-23) to replace rotating variables in the RHS of (4-27), an expression for $\frac{d}{dt}\boldsymbol{i}$ can be derived in the following manner:

$$\left(\frac{d}{dt}M\right)\boldsymbol{i_{qd}} + M\left(\frac{d}{dt}\boldsymbol{i_{qd}}\right) = \bar{A}_I(2{:}3,1)v_c + \bar{A}_I(2{:}3,2{:}3)M\boldsymbol{i_{qd}} + \bar{A}_I(2{:}3,4{:}5)M\boldsymbol{v_{qd}^f} + \bar{A}_I(2{:}3,6{:}7)M\boldsymbol{i_{L_{qd}}} \tag{4-31}$$

where, $\boldsymbol{v_{qd}^f} = \begin{bmatrix} v_q^f \\ v_d^f \end{bmatrix}$, $\boldsymbol{i_{L_{qd}}} = \begin{bmatrix} i_{L_q} \\ i_{L_d} \end{bmatrix}$

After rearranging (4-31) so only $\frac{d}{dt}\boldsymbol{i_{qd}}$ remains on the LHS:

$$\frac{d}{dt}\boldsymbol{i_{qd}} = M^{-1}\bar{A}_I(2{:}3,1)v_c + M^{-1}\left[\bar{A}_I(2{:}3,2{:}3)M - \frac{d}{dt}M\right]\boldsymbol{i_{qd}} + M^{-1}\bar{A}_I(2{:}3,4{:}5)M\boldsymbol{v_{qd}^f} + M^{-1}\bar{A}_I(2{:}3,6{:}7)M\boldsymbol{i_{L_{qd}}} \tag{4-32}$$

Similarly, using (4-28) and (3-23) the following expression for $\frac{d}{dt}\boldsymbol{v_{qd}^f}$ is derived as follows:

$$\left(\frac{d}{dt}M\right)\boldsymbol{v_{qd}^f} + M\left(\frac{d}{dt}\boldsymbol{v_{qd}^f}\right) = \bar{A}_I(4{:}5,2{:}3)M\boldsymbol{i_{qd}} + \bar{A}_I(4{:}5,6{:}7)M\boldsymbol{i_{L_{qd}}} \tag{4-33}$$

After rearranging the equation so only $\frac{d}{dt}\boldsymbol{v_{qd}^f}$ remains on the LHS:

$$\frac{d}{dt}\boldsymbol{v_{qd}^f} = M^{-1}\bar{A}_I(1{,}2{:}3)M\boldsymbol{i_{qd}} - M^{-1}\frac{d}{dt}M\boldsymbol{v_{qd}^f} + M^{-1}\bar{A}_I(4{:}5,6{:}7)M\boldsymbol{i_{L_{qd}}} \tag{4-34}$$

Likewise, $\frac{d}{dt}\boldsymbol{i_{L_{qd}}}$ is obtained as follow:

$$\left(\frac{d}{dt}M\right)\boldsymbol{i_{L_{qd}}} + M\left(\frac{d}{dt}\boldsymbol{i_{L_{qd}}}\right) = \bar{A}_I(6{:}7,2{:}3)M\boldsymbol{i_{qd}} + \bar{A}_I(6{:}7,4{:}5)M\boldsymbol{v_{qd}^f} + \bar{A}_I(6{:}7,6{:}7)M\boldsymbol{i_{L_{qd}}} \tag{4-35}$$

After rearranging the equation so only $\frac{d}{dt}\boldsymbol{i_{L_{qd}}}$ remains on the LHS:

$$\begin{aligned}\frac{d}{dt}\boldsymbol{i}_{\boldsymbol{L_{qd}}} &= M^{-1}\bar{A}_I(6:7,2:3)M\boldsymbol{i}_{\boldsymbol{qd}} + M^{-1}\bar{A}_I(6:7,4:5)M\boldsymbol{v}^{\boldsymbol{f}}_{\boldsymbol{qd}} \\ &\quad + M^{-1}[\bar{A}_I(6:7,6:7)M\boldsymbol{i}_{\boldsymbol{L_{qd}}} - \frac{d}{dt}M]\end{aligned} \tag{4-36}$$

Arranging (4-30)-(4-36) in standard state-space matrix representation yields the following:

$$\frac{d}{dt}\begin{bmatrix} v_c \\ \boldsymbol{i}_{\boldsymbol{qd}} \\ \boldsymbol{v}^{\boldsymbol{f}}_{\boldsymbol{qd}} \\ \boldsymbol{i}_{\boldsymbol{L_{qd}}} \end{bmatrix} =$$

$$\begin{bmatrix} \bar{A}_I(1,1) & \bar{A}_I(1,2:3)M & 0_{1x2} & 0_{1x2} \\ M^{-1}\bar{A}_I(2:3,1) & M^{-1}\left[\bar{A}_I(2:3,2:3)M - \frac{d}{dt}M\right] & M^{-1}\bar{A}_I(2:3,4:5)M & M^{-1}\bar{A}_I(2:3,6:7)M \\ 0_{2x1} & M^{-1}\bar{A}_I(4:5,2:3)M & -M^{-1}\frac{d}{dt}M & M^{-1}\bar{A}_I(4:5,6:7)M \\ 0_{2x1} & M^{-1}\bar{A}_I(6:7,2:3)M & M^{-1}\bar{A}_I(6:7,4:5)M & M^{-1}\left[\bar{A}_I(6:7,6:7)M - \frac{d}{dt}M\right] \end{bmatrix}\begin{bmatrix} v_c \\ \boldsymbol{i}_{\boldsymbol{qd}} \\ \boldsymbol{v}^{\boldsymbol{f}}_{\boldsymbol{qd}} \\ \boldsymbol{i}_{\boldsymbol{L_{qd}}} \end{bmatrix} +$$

$$\begin{bmatrix} B(1,1) \\ 0_{2x1} \\ 0_{2x1} \\ 0_{2x1} \end{bmatrix} u \tag{4-37}$$

Replacing the duty ratios d_1 and d_2 in $\bar{A}_I$ by their corresponding expressions presented in Chapter 2, (2-22) and (2-23) respectively, and applying a few trigonometric identities to simplify the state matrix in the (4-37) results in the following state-space representation:

$$\frac{d}{dt}\begin{bmatrix} v_c \\ i_q \\ i_d \\ v_q^f \\ v_d^f \\ i_{L_q} \\ i_{L_d} \end{bmatrix} =$$

$$\begin{bmatrix}
\frac{-1}{CR_s} & \frac{-\sqrt{3}\,m\cos(\theta_f-\theta)}{2C} & \frac{\sqrt{3}\,m\sin(\theta_f-\theta)}{2C} & 0 & 0 & 0 & 0 \\
\frac{\sqrt{3}\,m\cos(\theta_f-\theta)}{3L_1} & \frac{-R_f}{3L_1} & \dot{\theta}_f & \frac{-1}{2L_1} & \frac{-\sqrt{3}}{6L_1} & \frac{R_f}{3L_1} & 0 \\
\frac{-\sqrt{3}\,m\sin(\theta_f-\theta)}{3L_1} & -\dot{\theta}_f & \frac{-R_f}{3L_1} & \frac{-\sqrt{3}}{6L_1} & \frac{-1}{2L_1} & 0 & \frac{R_f}{3L_1} \\
0 & \frac{1}{2C_f} & \frac{-\sqrt{3}}{6C_f} & 0 & \dot{\theta}_f & \frac{-1}{2C_f} & \frac{\sqrt{3}}{6C_f} \\
0 & \frac{\sqrt{3}}{6C_f} & \frac{1}{2C_f} & -\dot{\theta}_f & 0 & \frac{-\sqrt{3}}{6C_f} & \frac{-1}{2C_f} \\
0 & \frac{R_f}{3(L_2+L)} & 0 & \frac{1}{2(L_2+L)} & \frac{\sqrt{3}}{6(L_2+L)} & \frac{-3R_L-R_f}{3(L_2+L)} & \dot{\theta}_f \\
0 & 0 & \frac{R_f}{3(L_2+L)} & -\frac{\sqrt{3}}{6(L_2+L)} & \frac{1}{2(L_2+L)} & -\dot{\theta}_f & \frac{-3R_L-R_f}{3(L_2+L)}
\end{bmatrix}
\begin{bmatrix} v_c \\ i_q \\ i_d \\ v_q^f \\ v_d^f \\ i_{L_q} \\ i_{L_d} \end{bmatrix}$$

$$+\begin{bmatrix} \frac{1}{CR_s} \\ 0 \\ 0 \\ 0 \\ 0 \\ 0 \\ 0 \end{bmatrix} u \qquad (4\text{-}38)$$

$\theta_f - \theta$ is the difference between the angle of the synchronous dq frame of reference, θ_f, and line-to-neutral voltage phase angle of the VSI, θ. For our purpose, both angles are set to equal each other, i.e. $\theta_f - \theta = 0$. In addition, $\dot{\theta}_f$ represents the angular speed of the dq frame of reference. Since the dq transformation applied is synchronous, the dq frame of reference has the same angular speed as the VSI three-phase voltages. Therefore, $\dot{\theta}_f$ can be replaced by $\omega = 2\pi f$, where f is the VSI frequency. Applying the aforementioned changes yields the following model:

$$\dot{\tilde{x}}_{qd} = \bar{A}_{qd}\tilde{x}_{qd} + Bu \qquad (4\text{-}39)$$

where,

$$\bar{A}_{qd} = \begin{bmatrix} \frac{-1}{CR_s} & \frac{-\sqrt{3}\,m}{2C} & 0 & 0 & 0 & 0 & 0 \\ \frac{\sqrt{3}\,m}{3L_1} & \frac{-R_f}{3L_1} & \omega & \frac{-1}{2L_1} & \frac{-\sqrt{3}}{6L_1} & \frac{R_f}{3L_1} & 0 \\ 0 & -\omega & \frac{-R_f}{3L_1} & \frac{-\sqrt{3}}{6L_1} & \frac{-1}{2L_1} & 0 & \frac{R_f}{3L_1} \\ 0 & \frac{1}{2C_f} & \frac{-\sqrt{3}}{6C_f} & 0 & \omega & \frac{-1}{2C_f} & \frac{\sqrt{3}}{6C_f} \\ 0 & \frac{\sqrt{3}}{6C_f} & \frac{1}{2C_f} & -\omega & 0 & \frac{-\sqrt{3}}{6C_f} & \frac{-1}{2C_f} \\ 0 & \frac{R_f}{3(L_2+L)} & 0 & \frac{1}{2(L_2+L)} & \frac{\sqrt{3}}{6(L_2+L)} & \frac{-3R_L-R_f}{3(L_2+L)} & \omega \\ 0 & 0 & \frac{R_f}{3(L_2+L)} & -\frac{\sqrt{3}}{6(L_2+L)} & \frac{1}{2(L_2+L)} & -\omega & \frac{-3R_L-R_f}{3(L_2+L)} \end{bmatrix} \tag{4-40}$$

and

$$\tilde{x}_{qd} = \begin{bmatrix} v_c \\ i_q \\ i_d \\ v_q^f \\ v_d^f \\ i_{L_q} \\ i_{L_d} \end{bmatrix} \tag{4-41}$$

As previously mentioned, any of the state-space models representing the six sectors, $\bar{A}_I$, ..., $\bar{A}_{VI}$, can model the behavior of the VSI once transformed into a dq synchronous frame of reference. To verify this claim, the above transformation and simplifications were applied to the state-space representations of the other sectors. The result was the conversion of every one of the six models to the model in (4-39).

b) Small-Signal Model:

Modulation index m is assumed to be constant in the averaged-state-space model in (4-39). In practice, m is a variable used to regulate the output voltage. To take that into consideration, (4-39) is linearized around pre-calculated steady-state operating points and then a small perturbation is introduced as follows:

$$\boldsymbol{\tilde{x}_{qd}} = \boldsymbol{\tilde{X}_{qd}} + \boldsymbol{\delta\tilde{x}_{qd}} \;, \quad m = M + \delta m \;, \quad u = \mathrm{U} + \delta u \tag{4-42}$$

Capital letters in (4-42) symbolizes steady-state operating points and δ symbolizes small perturbation. After incorporating (4-42) and ignoring higher order terms, the following small-signal model was derived:

$$\frac{d}{dt}\begin{bmatrix}\delta v_c\\ \delta i_q\\ \delta i_d\\ \delta v_q^f\\ \delta v_d^f\\ \delta i_{L_q}\\ \delta i_{L_d}\end{bmatrix}=\begin{bmatrix}\frac{-1}{CR_s} & \frac{-\sqrt{3}\,M}{2C} & 0 & 0 & 0 & 0 & 0\\ \frac{\sqrt{3}\,M}{3L_1} & \frac{-R_f}{3L_1} & \omega & \frac{-1}{2L_1} & \frac{-\sqrt{3}}{6L_1} & \frac{R_f}{3L_1} & 0\\ 0 & -\omega & \frac{-R_f}{3L_1} & \frac{-\sqrt{3}}{6L_1} & \frac{-1}{2L_1} & 0 & \frac{R_f}{3L_1}\\ 0 & \frac{1}{2C_f} & \frac{-\sqrt{3}}{6C_f} & 0 & \omega & \frac{-1}{2C_f} & \frac{\sqrt{3}}{6C_f}\\ 0 & \frac{\sqrt{3}}{6C_f} & \frac{1}{2C_f} & -\omega & 0 & \frac{-\sqrt{3}}{6C_f} & \frac{-1}{2C_f}\\ 0 & \frac{R_f}{3(L_2+L)} & 0 & \frac{1}{2(L_2+L)} & \frac{\sqrt{3}}{6(L_2+L)} & \frac{-3R_L-R_f}{3(L_2+L)} & \omega\\ 0 & 0 & \frac{R_f}{3(L_2+L)} & -\frac{\sqrt{3}}{6(L_2+L)} & \frac{1}{2(L_2+L)} & -\omega & \frac{-3R_L-R_f}{3(L_2+L)}\end{bmatrix}\begin{bmatrix}\delta v_c\\ \delta i_q\\ \delta i_d\\ \delta v_q^f\\ \delta v_d^f\\ \delta i_{L_q}\\ \delta i_{L_d}\end{bmatrix}+$$

$$\begin{bmatrix}\frac{1}{CR_s} & \frac{-\sqrt{3}\,\tilde{I}_q}{2C}\\ 0 & \frac{\sqrt{3}\,\tilde{V}_c}{L_1}\\ 0 & 0\\ 0 & 0\\ 0 & 0\\ 0 & 0\\ 0 & 0\end{bmatrix}\begin{bmatrix}\delta v_{dc}\\ \delta m\end{bmatrix} \tag{4-43}$$

4.2 Averaged-State-Space Model of the Three-Phase SVPWM VSI under Grid-Tied Mode

The same procedure followed to derive the averaged-state-space model for the three-phase SVPWM VSI under stand-alone mode was followed to derive a similar model under grid-tied mode. The system being modeled in this section is depicted in Figure 4-3. The grid is modeled as a three-phase voltage source with its series inductance, L_g, and its series resistance, R_g.

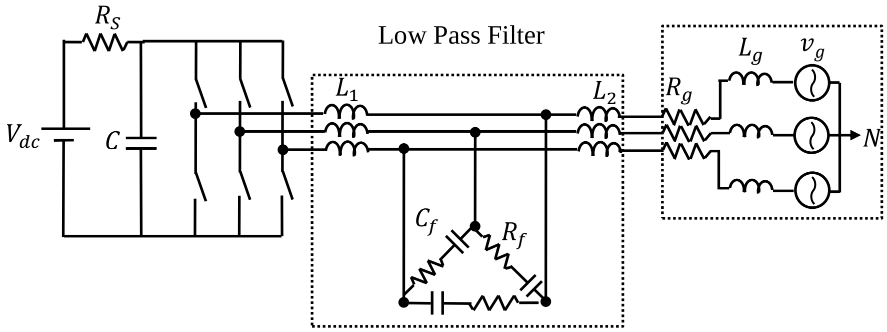

Figure 4-3: Three-Phase VSI under Grid-Tied Mode

Similar to the pervious section, only the state-space-representation for zero switching states, 000 and 111, is discussed thoroughly in great details. State-space representations for other switching states are given in Appendix A.

a) *Large-Signal Model:*

Linear circuit modeling the zero switching states, marked with the appropriate voltages and currents is depicted in Figure 4-4. Since the only difference between the circuit in Figure 4-4 and Figure 4-2 is the addition of voltage sources (the grid), the same state variables will be used and the line-to-line grid voltages will be added to the systems inputs.

First, to derive an expression for $\dot{v}_c$, the following KCL equation is derived:

$$\frac{v_c - V_{dc}}{R_s} + C\dot{v}_c = 0 \tag{4-44}$$

From (4-44), an equation for $\dot{v}_c$ can be derived as follow:

$$\dot{v}_c = \frac{V_{dc} - v_c}{CR_s} \tag{4-45}$$

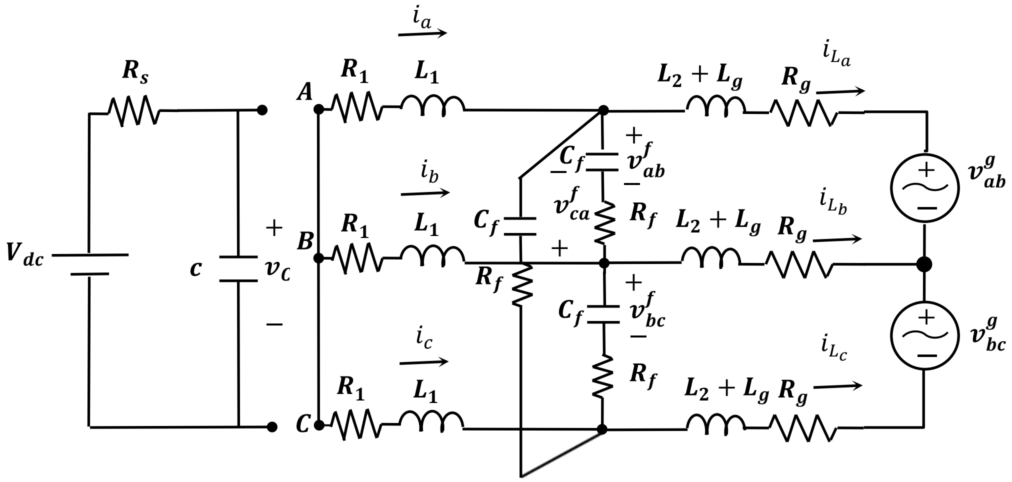

Figure 4-4: Linear Circuit Representing Zero Switching States (Grid-Tied)

Second, to derive expressions for v_{ab}^f and v_{bc}^f, the following KCL equations are derived as follows:

$$i_a - i_{L_a} - C_f\left(\dot{v}_{ab}^f - \dot{v}_{ca}^f\right) = 0 \tag{4-46}$$

$$i_b - i_{L_b} + C_f\left(\dot{v}_{ab}^f - \dot{v}_{bc}^f\right) = 0 \tag{4-47}$$

Replacing $-\dot{v}_{ca}^f$ with $\dot{v}_{ab}^f + \dot{v}_{bc}^f$ in (4-46) results in:

$$i_a - i_{L_a} - C_f\left(2\dot{v}_{ab}^f + \dot{v}_{bc}^f\right) = 0 \tag{4-48}$$

From (4-47) and (4-48), equations for $\dot{v}_{ab}^f$and $\dot{v}_{bc}^f$ can be derived as follows:

$$\dot{v}_{ab}^f = \frac{-i_{L_a} + i_a - i_b + i_{L_b}}{3C_f} \tag{4-49}$$

$$\dot{v}_{bc}^f = \frac{-i_{L_a} + i_a + 2(i_b - i_{L_b})}{3C_f} \tag{4-50}$$

Third, to develop expressions for i_a and i_b, KVL equations for the loops formed by i_a and i_b must be derived. In order to do so, expressions for the currents flowing from phase A to B through C_f and B to C through C_f must be developed. Using (4-49) and (4-50), the following current equations are derived:

$$i_{a\ to\ b} = C_f \dot{v}_{ab}^{f} = \frac{-i_{L_a} + i_a - i_b + i_{L_b}}{3} \tag{4-51}$$

$$i_{b\ to\ c} = C_f \dot{v}_{bc}^{f} = \frac{-i_{L_a} + i_a + 2(i_b - i_{L_b})}{3} \tag{4-52}$$

Using (4-51) and (4-52) the following KVL equations are derived:

$$R_1(i_a - i_b) + L_1(\dot{i_a} - \dot{i_b}) + v_{ab}^{f} + \left(\frac{i_a - i_{L_a} - i_b + i_{L_b}}{3}\right) R_f = 0 \tag{4-53}$$

$$R_1(2i_b + i_a) + L_1(2\dot{i_b} + \dot{i_a}) + v_{bc}^{f} + \left(\frac{i_a - i_{L_a} + 2\left(i_b - i_{L_b}\right)}{3}\right) R_f = 0 \tag{4-54}$$

From (4-53) and (4-54) the following expressions for $\dot{i_a}$ and $\dot{i_b}$ are derived as follows:

$$\dot{i_a} = \frac{-3R_1 i_a - 2v_{ab}^{f} - v_{bc}^{f} + \left(i_{L_a} - i_a\right)R_f}{3L_1} \tag{4-55}$$

$$\dot{i_b} = \frac{-3R_1 i_b + v_{ab}^{f} + \left(i_{L_b} - i_b\right)R_f - v_{bc}^{f}}{3L_1} \tag{4-56}$$

Finally, to derive expressions for $\dot{i}_{L_a}$ and $\dot{i}_{L_b}$, KVL equations for the loops formed by i_{L_a} and $i_{L_b}$are developed as follow:

$$v_{ab}^{f} + \frac{(i_a - i_{L_a} - i_b + i_{L_b})}{3} R_{ac} = R_g\left(i_{L_a} - i_{L_b}\right) + \left(L_2 + L_g\right)\left(\dot{i}_{L_a} - \dot{i}_{L_b}\right) + v_{ab}^{g} \tag{4-57}$$

$$v_{bc}^{f} + \frac{(i_a - i_{L_a} + 2i_b - i_{L_b})}{3} R_{ac} = R_g\left(2i_{L_b} + i_{L_a}\right) + \left(L_2 + L_g\right)\left(2\dot{i}_{L_b} + \dot{i}_{L_a}\right) + v_{bc}^{g} \tag{4-58}$$

Solving for $\dot{i}_{L_a}$ and $\dot{i}_{L_b}$, yields:

$$\dot{i}_{L_a} = \frac{2v_{ab}^{f} + R_f(i_a - i_{al}) + v_{bc}^{f} - 3R_g i_{al} - 2v_{ab}^{g} - v_{bc}^{g}}{3(L_2 + L_g)} \tag{4-59}$$

$$\dot{i}_{L_b} = \frac{v_{bc}^{f} + R_f(i_b - i_{bl}) - v_{ab}^{f} - 3R_g i_{bl} + v_{ab}^{g} - v_{bc}^{g}}{3(L_2 + L_g)} \tag{4-60}$$

Arranging the above expressions, (4-44)-(4-60), for the aforementioned state variables and recognizing V_{dc}, v_{ab}^{g}, and v_{bc}^{g} as systems input, yields the following state space representation for zero switching states:

$$\dot{x} = A_{000}\, x + Bu \tag{4-61}$$

where,

$$x = \begin{bmatrix} v_c \\ i_a \\ i_b \\ v_{ab}^{f} \\ v_{bc}^{f} \\ i_{L_a} \\ i_{L_b} \end{bmatrix} \tag{4-62}$$

$$A_{000} = \begin{bmatrix} \frac{-1}{CR_s} & 0 & 0 & 0 & 0 & 0 & 0 \\ 0 & \frac{-(3R_1+R_f)}{3L_1} & 0 & \frac{-2}{3L_1} & \frac{-1}{3L_1} & \frac{R_f}{3L_1} & 0 \\ 0 & 0 & \frac{-(3R_1+R_f)}{3L_1} & \frac{1}{3L_1} & \frac{-1}{3L_1} & 0 & \frac{R_f}{3L_1} \\ 0 & \frac{1}{3C_f} & \frac{-1}{3C_f} & 0 & 0 & \frac{-1}{3C_f} & \frac{1}{3C_f} \\ 0 & \frac{1}{3C_f} & \frac{2}{3C_f} & 0 & 0 & \frac{-1}{3C_f} & \frac{-2}{3C_f} \\ 0 & \frac{R_f}{3(L_2+L_g)} & 0 & \frac{2}{3(L_2+L_g)} & \frac{1}{3(L_2+L_g)} & \frac{-3R_g-R_f}{3(L_2+L_g)} & 0 \\ 0 & 0 & \frac{R_f}{3(L_2+L_g)} & \frac{-1}{3(L_2+L_g)} & \frac{1}{3(L_2+L_g)} & 0 & \frac{-3R_g-R_f}{3(L_2+L_g)} \end{bmatrix} \tag{4-63}$$

$$B = \begin{bmatrix} \frac{-1}{CR_s} & 0 & 0 \\ 0 & 0 & 0 \\ 0 & 0 & 0 \\ 0 & 0 & 0 \\ 0 & 0 & 0 \\ 0 & \frac{-2}{3(L_2+L_g)} & \frac{-1}{3(L_2+L_g)} \\ 0 & \frac{1}{3(L_2+L_g)} & \frac{-1}{3(L_2+L_g)} \end{bmatrix} \tag{4-64}$$

and,

$$u = \begin{bmatrix} V_{dc} \\ v_{ab}^{g} \\ v_{bc}^{g} \end{bmatrix} \tag{4-65}$$

The model in (4-61) is only representing the operation of the three-phase SVPWM VSI during the portion of the switching cycle T_s corresponding to the duty ratio d_0. To derive a comprehensive model valid for Sector I, the state-space averaging method must be applied to the zero switching state and two active states as follow:

$$\tilde{\dot{x}} = \bar{A}x + Bu \tag{4-66}$$

where $\bar{A}$ is defined as follow:

$$\bar{A} = d_0 A_0 + d_1 A_1 + d_2 A_2 \tag{4-67}$$

The state matrix A in (4-66) is averaged while the control matrix B is not because B is constant for every switching state. Thus, it does not need to be averaged. Moreover, the definition of the averaged state matrix A in (4-67) results in different matrix for each sector. Therefore, six state-space representations are obtained and included in Appendix B. The result of (4.62) for Sector I is defined as follows:

$$\dot{\tilde{x}} = \bar{A}_I \tilde{x} + Bu \tag{4-68}$$

where,

$$\bar{A}_I = d_0 A_{000} + d_1 A_{100} + d_2 A_{110} \tag{4-69}$$

$$\bar{A}_I = \begin{bmatrix} \frac{-1}{CR_s} & \frac{-(d_1+d_2)}{C} & \frac{-d_2}{C} & 0 & 0 & 0 & 0 \\ \frac{2d_1+d_2}{3L_1} & \frac{-(3R_1+R_f)}{3L_1} & 0 & \frac{-2}{3L_1} & \frac{-1}{3L_1} & \frac{R_f}{3L_1} & 0 \\ \frac{-d_1+d_2}{3L_1} & 0 & \frac{-(3R_1+R_f)}{3L_1} & \frac{1}{3L_1} & \frac{-1}{3L_1} & 0 & \frac{R_f}{3L_1} \\ 0 & \frac{1}{3C_f} & \frac{-1}{3C_f} & 0 & 0 & \frac{-1}{3C_f} & \frac{1}{3C_f} \\ 0 & \frac{1}{3C_f} & \frac{2}{3C_f} & 0 & 0 & \frac{-1}{3C_f} & \frac{-2}{3C_f} \\ 0 & \frac{R_f}{3(L_2+L_g)} & 0 & \frac{2}{3(L_2+L_g)} & \frac{1}{3(L_2+L_g)} & \frac{-3R_g-R_f}{3(L_2+L_g)} & 0 \\ 0 & 0 & \frac{R_f}{3(L_2+L_g)} & \frac{-1}{3(L_2+L_g)} & \frac{1}{3(L_2+L_g)} & 0 & \frac{-3R_g-R_f}{3(L_2+L_g)} \end{bmatrix} \tag{4-70}$$

The averaged-state-space representation given by (4-68) is only valid for Sector I. To derive a time invariant averaged-state-space representation, the model in (4-68) must be transformed into a dq synchronous frame of reference. The first step of the transformation is to group rotating quantities together in sub matrices as follows:

$$\frac{d}{dt}\begin{bmatrix} v_c \\ \boldsymbol{i} \\ \boldsymbol{v_{LL}} \\ \boldsymbol{i_L} \end{bmatrix} = \begin{bmatrix} \bar{A}_I(1,1) & \bar{A}_I(1,2:3) & 0_{1x2} & 0_{1x2} \\ \bar{A}_I(2:3,1) & \bar{A}_I(2:3,2:3) & \bar{A}_I(2:3,4:5) & \bar{A}_I(2:3,6:7) \\ 0_{2x1} & \bar{A}_I(4:5,2:3) & 0_{2x2} & \bar{A}_I(4:5,6:7) \\ 0_{2x1} & \bar{A}_I(6:7,2:3) & \bar{A}_I(6:7,4:5) & \bar{A}_I(6:7,6:7) \end{bmatrix} \begin{bmatrix} v_c \\ \boldsymbol{i} \\ \boldsymbol{v_{LL}} \\ \boldsymbol{i_L} \end{bmatrix} + \begin{bmatrix} B(1,1) & 0_{1x2} \\ 0_{2x1} & 0_{2x2} \\ 0_{2x1} & 0_{2x2} \\ 0_{2x1} & B(6:7,2:3) \end{bmatrix} u \tag{4-71}$$

where, $\boldsymbol{i} = \begin{bmatrix} i_a \\ i_b \end{bmatrix}$, $\boldsymbol{v_{LL}} = \begin{bmatrix} v_{ab}^f \\ v_{bc}^f \end{bmatrix}$, and $\boldsymbol{i_L} = \begin{bmatrix} i_{L_a} \\ i_{L_b} \end{bmatrix}$

Similar to the transformation carried out in Section 4.1 (the stand-alone case), the dq transformation can be applied to v_c, $\boldsymbol{i}$, $\boldsymbol{v_{LL}}$, and $\boldsymbol{i_L}$ individually. However, in the grid-tied case, the grid is used as a reference for the synchronous dq transformation. Therefore, the term $\theta_f - \theta$ represents the voltage phase difference between the grid and the inverter. This term is used to control the injection of active power to the grid and it is referred to as ϕ in this thesis. Applying the dq transformation and recognizing $\theta_f - \theta$ as ϕ yields the following model:

$$\dot{\tilde{x}}_{qd} = \bar{A}_{qd}\tilde{x}_{qd} + B_{qd}u_{qd} \tag{4-72}$$

where,

$$\bar{A}_{qd} = \begin{bmatrix} \frac{-1}{CR_s} & \frac{-\sqrt{3}\, mcos(\phi)}{2C} & \frac{-\sqrt{3}\, msin(\phi)}{2C} & 0 & 0 & 0 & 0 \\ \frac{\sqrt{3}\, mcos(\phi)}{3L_1} & \frac{-R_f}{3L_1} & \omega & \frac{-1}{2L_1} & \frac{-\sqrt{3}}{6L_1} & \frac{R_f}{3L_1} & 0 \\ \frac{\sqrt{3}\, msin(\phi)}{3L_1} & -\omega & \frac{-R_f}{3L_1} & \frac{-\sqrt{3}}{6L_1} & \frac{-1}{2L_1} & 0 & \frac{R_f}{3L_1} \\ 0 & \frac{1}{2C_f} & \frac{-\sqrt{3}}{6C_f} & 0 & \omega & \frac{-1}{2C_f} & \frac{\sqrt{3}}{6C_f} \\ 0 & \frac{\sqrt{3}}{6C_f} & \frac{1}{2C_f} & -\omega & 0 & \frac{-\sqrt{3}}{6C_f} & \frac{-1}{2C_f} \\ 0 & \frac{R_f}{3(L_2+L_g)} & 0 & \frac{1}{2(L_2+L_g)} & \frac{\sqrt{3}}{6(L_2+L_g)} & \frac{-3R_g-R_f}{3(L_2+L_g)} & \omega \\ 0 & 0 & \frac{R_f}{3(L_2+L_g)} & -\frac{\sqrt{3}}{6(L_2+L_g)} & \frac{1}{2(L_2+L_g)} & -\omega & \frac{-3R_g-R_f}{3(L_2+L_g)} \end{bmatrix} \tag{4-73}$$

$$\tilde{x}_{qd} = \begin{bmatrix} v_c \\ i_q \\ i_d \\ v_q^f \\ v_d^f \\ i_{L_q} \\ i_{L_d} \end{bmatrix} \tag{4-74}$$

$$u = \begin{bmatrix} V_{dc} \\ v_q^g \\ v_d^g \end{bmatrix} \tag{4-75}$$

$$B_{qd} = \begin{bmatrix} \frac{-1}{CR_s} & 0 & 0 \\ 0 & 0 & 0 \\ 0 & 0 & 0 \\ 0 & 0 & 0 \\ 0 & 0 & 0 \\ 0 & \frac{-1}{2(L_2+L_g)} & \frac{\sqrt{3}}{6(L_2+L_g)} \\ 0 & \frac{-\sqrt{3}}{6(L_2+L_g)} & \frac{\sqrt{3}}{6(L_2+L_g)} \end{bmatrix} \tag{4-76}$$

As previously mentioned, any of the state-space models representing the six sectors can model the behavior of the three-phase SVPWM VSI once transformed into a synchronous dq frame of reference. To verify this claim, the above transformation and simplifications were applied to the averaged-state-space representations of the other sectors, given in Appendix B . The result was the conversion of every model to the model in (4-72).

b) *Small-Signal Model:*

The model in (4-72) regards the modulation index m and the phase difference ϕ as fixed parameters. In practice, m is a variable used to regulate the voltage and ϕ is a variable used to control the injection of power to the grid. To change m and ϕ from fixed parameters to variable inputs, the model in (4-72) is linearized around pre-calculated steady-state operating points then a small perturbation is introduced to produce a small-signal model as follows:

$$\boldsymbol{\tilde{x}_{qd}} = \boldsymbol{\tilde{X}_{qd}} + \boldsymbol{\delta\tilde{x}_{qd}} \ , \quad m = M + \delta m \ , \phi = \Phi + \delta\phi \ , \ u = \mathrm{U} + \delta u \tag{4-77}$$

Incorporating the (4-76) into (4-72) yields the following small-signal model:

$$\frac{d}{dt}\begin{bmatrix} \delta v_c \\ \delta i_q \\ \delta i_d \\ \delta v_q^f \\ \delta v_d^f \\ \delta i_{L_q} \\ \delta i_{L_d} \end{bmatrix} = \begin{bmatrix} \frac{-1}{CR_s} & \frac{-\sqrt{3}\,M}{2C} & 0 & 0 & 0 & 0 & 0 \\ \frac{\sqrt{3}\,M}{3L_1} & \frac{-R_f}{3L_1} & \omega & \frac{-1}{2L_1} & \frac{-\sqrt{3}}{6L_1} & \frac{R_f}{3L_1} & 0 \\ 0 & -\omega & \frac{-R_f}{3L_1} & \frac{-\sqrt{3}}{6L_1} & \frac{-1}{2L_1} & 0 & \frac{R_f}{3L_1} \\ 0 & \frac{1}{2C_f} & \frac{-\sqrt{3}}{6C_f} & 0 & \omega & \frac{-1}{2C_f} & \frac{\sqrt{3}}{6C_f} \\ 0 & \frac{\sqrt{3}}{6C_f} & \frac{1}{2C_f} & -\omega & 0 & \frac{-\sqrt{3}}{6C_f} & \frac{-1}{2C_f} \\ 0 & \frac{R_f}{3(L_2+L_g)} & 0 & \frac{1}{2(L_2+L_g)} & \frac{\sqrt{3}}{6(L_2+L_g)} & \frac{-3R_L-R_f}{3(L_2+L_g)} & \omega \\ 0 & 0 & \frac{R_f}{3(L_2+L_g)} & -\frac{\sqrt{3}}{6(L_2+L_g)} & \frac{1}{2(L_2+L_g)} & -\omega & \frac{-3R_L-R_f}{3(L_2+L)} \end{bmatrix} \begin{bmatrix} \delta v_c \\ \delta i_q \\ \delta i_d \\ \delta v_q^f \\ \delta v_d^f \\ \delta i_{L_q} \\ \delta i_{L_d} \end{bmatrix} +$$

$$\begin{bmatrix} \frac{1}{CR_s} & 0 & 0 & \frac{-\sqrt{3}\,[\tilde{I}_q\cos(\Phi)+\tilde{I}_d\sin(\Phi)]}{2C} & \frac{-\sqrt{3}\,[-\tilde{I}_q M\sin(\Phi)+\tilde{I}_q M\cos(\Phi)]}{2C} \\ 0 & 0 & 0 & \frac{\widetilde{V}_c\cos(\Phi)}{\sqrt{3}L_1} & \frac{-\,\widetilde{V}_c\,\mathrm{M}\sin(\Phi)}{\sqrt{3}L_1} \\ 0 & 0 & 0 & \frac{\widetilde{V}_c\sin(\Phi)}{\sqrt{3}L_1} & \frac{\widetilde{V}_c\,\mathrm{M}\cos(\Phi)}{\sqrt{3}L_1} \\ 0 & 0 & 0 & 0 & 0 \\ 0 & 0 & 0 & 0 & 0 \\ 0 & \frac{-1}{2(L_2+L_g)} & \frac{\sqrt{3}}{6(L_2+L_g)} & 0 & 0 \\ 0 & \frac{-\sqrt{3}}{6(L_2+L_g)} & \frac{\sqrt{3}}{6(L_2+L_g)} & 0 & 0 \end{bmatrix} \begin{bmatrix} \delta v_{dc} \\ \delta v_q^g \\ \delta v_d^g \\ \delta m \\ \delta\phi \end{bmatrix} \tag{4-78}$$

4.3 Eigenvalues Sensitivity Analysis of the Small-Signal Models of the Three-Phase SVPWM VSI

In this section, the small-signal models derived in (4-43) and (4-78) are used to carry out eigenvalues sensitivity analysis. This type of analysis is particularly useful to determine how variations in the systems parameters affect the systems stability. The eigenvalues sensitivity analysis is carried out by varying a single parameter at a time and observing the movement of the eigenvalues of the state matrix in the complex plane.

4.3.1 Sensitivity Analysis of Stand-Alone Small-Signal Model

This subsection investigates eigenvalues sensitivity analysis for the three-phase SVPWM VSI under stand-alone mode. The parameters of the system to be analyzed are given in Table 4-1 and initial eigenvalues locations of the system are given Table 4-2. As shown in Table 4-2, the system has a single negative real value and three complex pair values on the LHS of the complex plane, therefore, the system is initially stable.

Table 4-1: Eigenvalues Sensitivity Analysis Parameters (Stand-Alone)

Parameter	Nominal Value
C	$4000\ uF$
R_1	0.1 Ω
L_1	2.5 mH
R_f	0.5 Ω
C_f	$10\ uF$
R_g	2 Ω
$L_2 + L_g$	4 mH
M	0.9
Φ	-30°

Table 4-2: Initial Eigenvalues in the Complex Plane (Stand-Alone)

Eigenvalue	Location
$\lambda_{1,2}$	$-720.2 \pm j4995.7$
$\lambda_{3,4}$	$-720.2 \pm j4241.9$
$\lambda_{5,6}$	$-2062.8 \pm j383.5$
λ_7	-2484.7

A) Sensitivity of DC Bus Capacitance, C

Eigenvalues response to increased DC bus capacitance from $2000\ uF$ to $6000\ uF$ is shown in Figure 4-5 in which cross signs (+) indicate the locations of eigenvalues corresponding to nominal values of the systems parameters given in Table 4-1. As shown in Figure 4-5, only one eigenvalue, λ_1, was sensitive to changes in C. Increasing the DC capacitance moved λ_1 to the left. Therefore, increasing the DC capacitance improves the systems stability. In general, larger capacitance on the DC side of the inverter reduces the systems vulnerability to voltage changes, thereby ensuring a more stable operation.

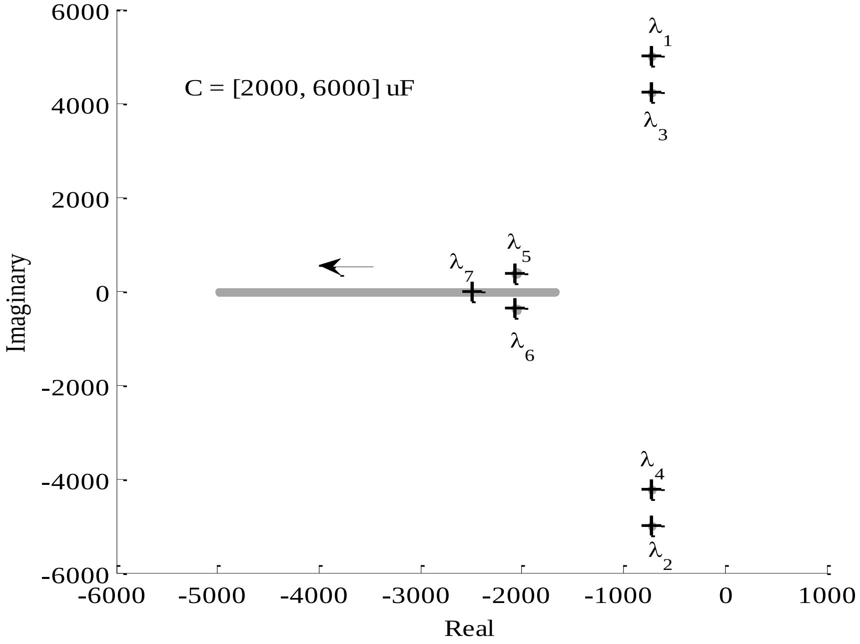

Figure 4-5: Eigenvalues Response to Change in the DC Capacitance, C (Stand-Alone)

B) Sensitivity of LCL Filter Inductor, L_1

Systems eigenvalues to L_1 value increases from $1.25\,mH$ to $3.75\,mH$ is shown in Figure 4-6. Although the value of L_1 is critically important for harmonics filtering, the increase in the value of L_1 hinders the systems stability. As shown in Figure 4-6, increasing L_1 moved $\lambda_{1,2}$, $\lambda_{3,4}$, and $\lambda_{5,6}$ towards the RHS of the complex plane. Therefore, the value of L_1 should be kept at minimum.

C) Sensitivity of Damping Resistor, R_f

Systems response to the increase of R_f from 0 to 5Ω is shown in Figure 4-7. Increasing R_f moved $\lambda_{1,2}$, and $\lambda_{3,4}$ away from the imaginary axis, thereby improving the system stability. Increasing R_f might be desirable from a damping point of view. However, larger values of R_f increases the losses at the fundamental frequency.

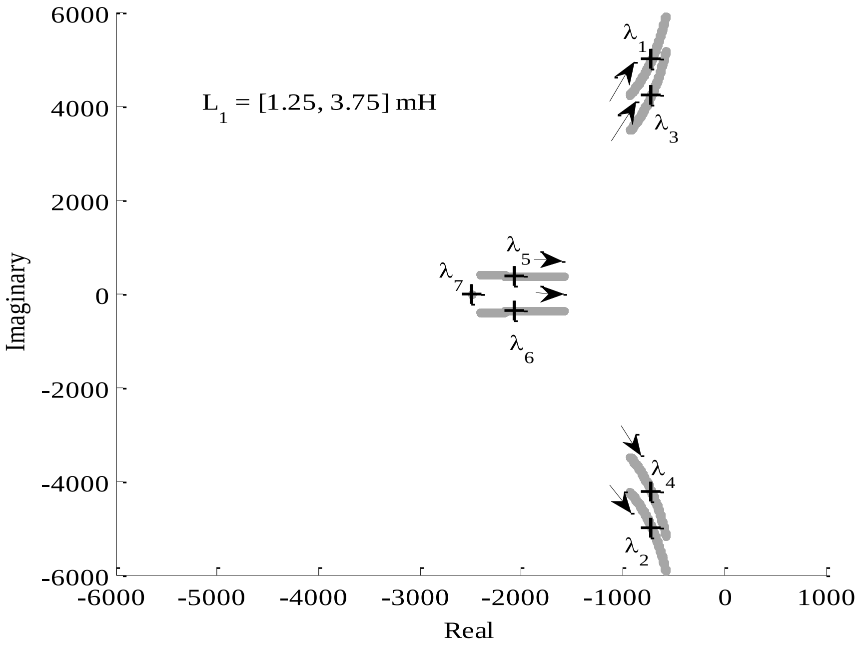

Figure 4-6: Eigenvalues Response to Change in LCL Filter Inductor, L_1 (Stand-Alone)

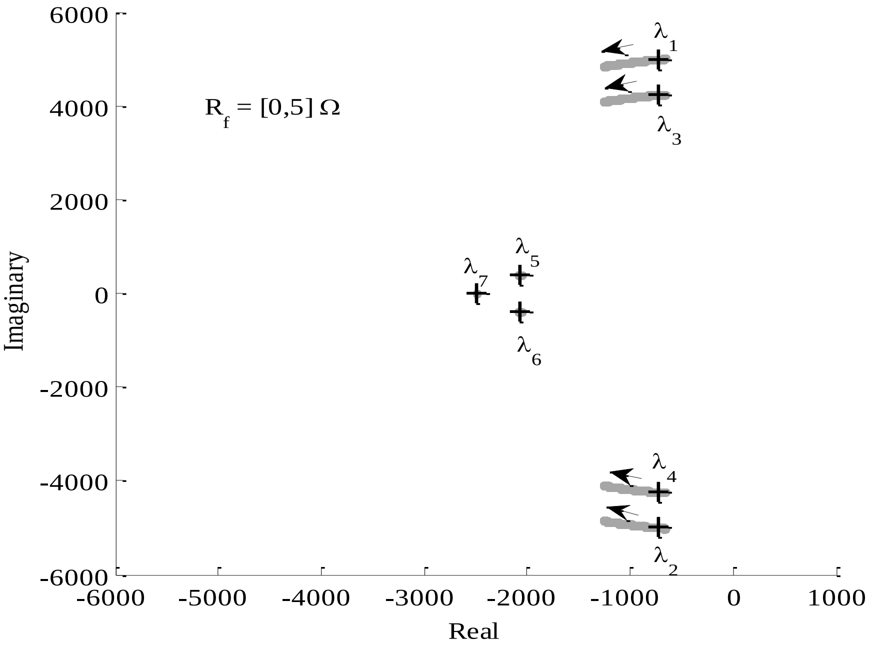

Figure 4-7: Eigenvalues Response to Change in Damping Resistor of LCL Filter, R_f (Stand-Alone)

D) *Sensitivity of LCL Capacitor, C_f*

Eigenvalues response to an increase in the LCL filter capacitor from 5 to 15 uF is shown in Figure 4-8. As C_f increased, the locations of $\lambda_{1,2}$ and $\lambda_{3,4}$ moved toward the origin point and the locations of $\lambda_{5,6}$ moved horizontally to the RHS of the complex plane. Therefore, larger C_f values aggravate systems stability.

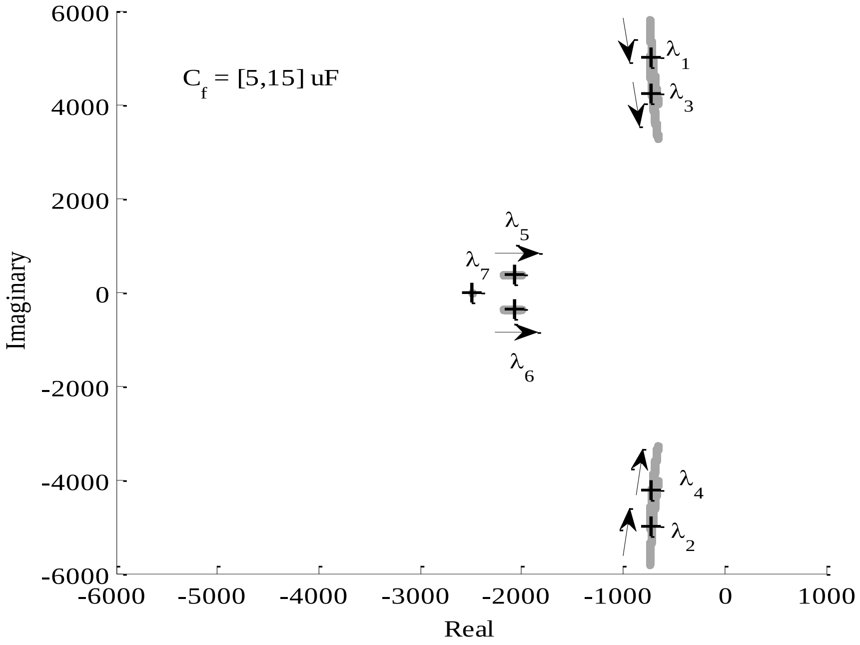

Figure 4-8: Eigenvalues Response to Change in the LCL Capacitor, C_f (Stand-Alone)

E) *Sensitivity of Load Resistance, R_L*

Systems response to an increase of load resistance from 5 to 20 Ω is shown in Figure 4-9. The locations of $\lambda_{1,2}$, $\lambda_{3,4}$, and $\lambda_{5,6}$ moved further into the LHS of the complex plane as R_L increased. However, the location of λ_7 remained unchanged. Therefore, the overall stability of the system improves as load resistance increases.

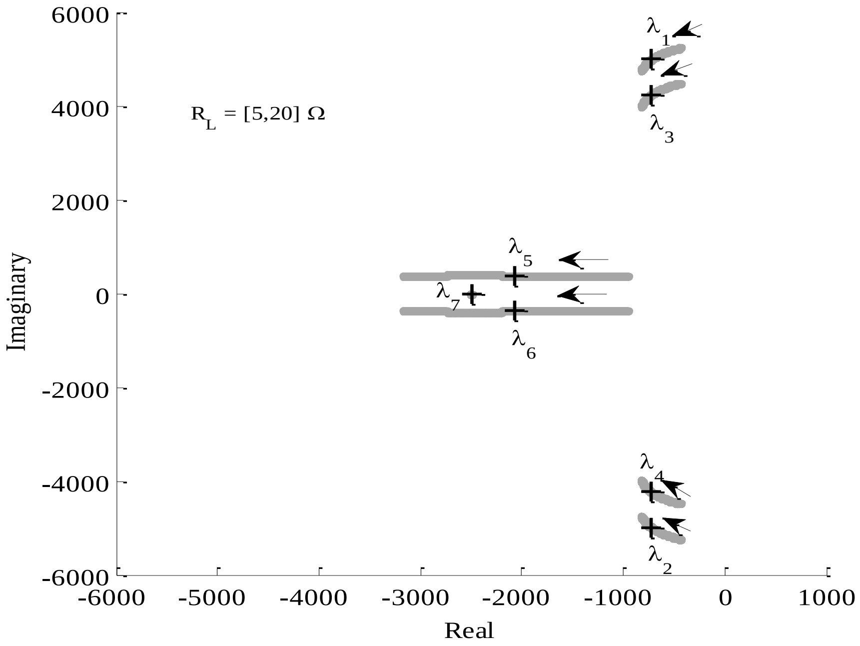

Figure 4-9: Eigenvalues Response to Change in Load Resistance, R_L (Stand-Alone)

F) Sensitivity of LCL filter Inductor and Load Inductance,$L_2 + L$

System response to increased filter inductance and load inductance, $L_2 + L$, are shown in Figure 4-10. As $L_2 + L$ increased, the locations of $\lambda_{1,2}$ and $\lambda_{3,4}$ moved toward the origin and the locations of $\lambda_{5,6}$ moved horizontally to the RHS of the complex plane. However, the location of λ_7 remained unchanged. Therefore, the overall effect of increasing $L_2 + L$ hinders the system stability.

G) Sensitivity of Modulation Index, M

The effect of increasing the modulation index, *M*, from 0.7 to 0.9 on the systems eigenvalues is shown in Figure 4-11. As shown in the figure, the locations of the eigenvalues of the system are not affected by varying M.

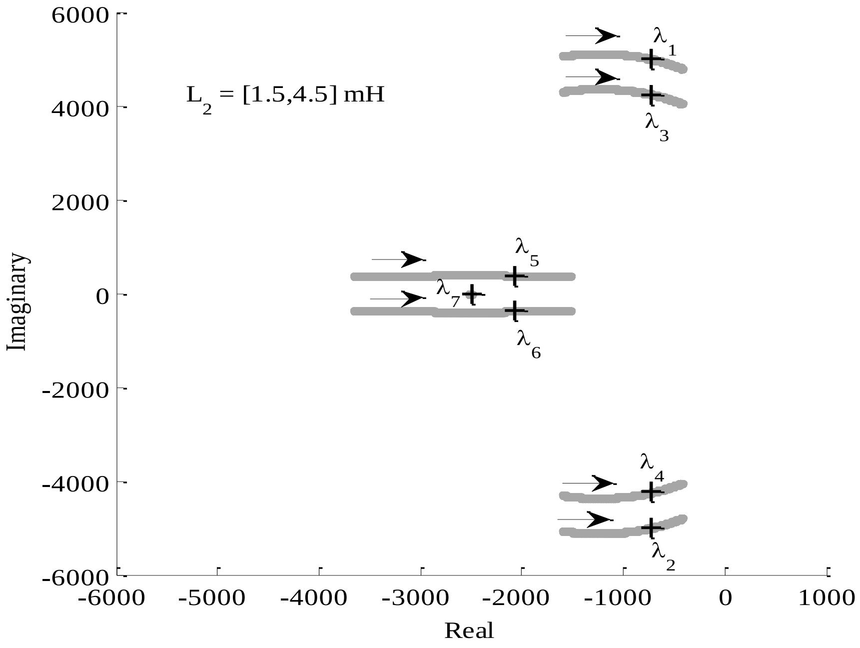

Figure 4-10: Eigenvalues Response to Change in LCL Filter Inductor and Load Inductance, $L_2 + L$ (Stand-Alone)

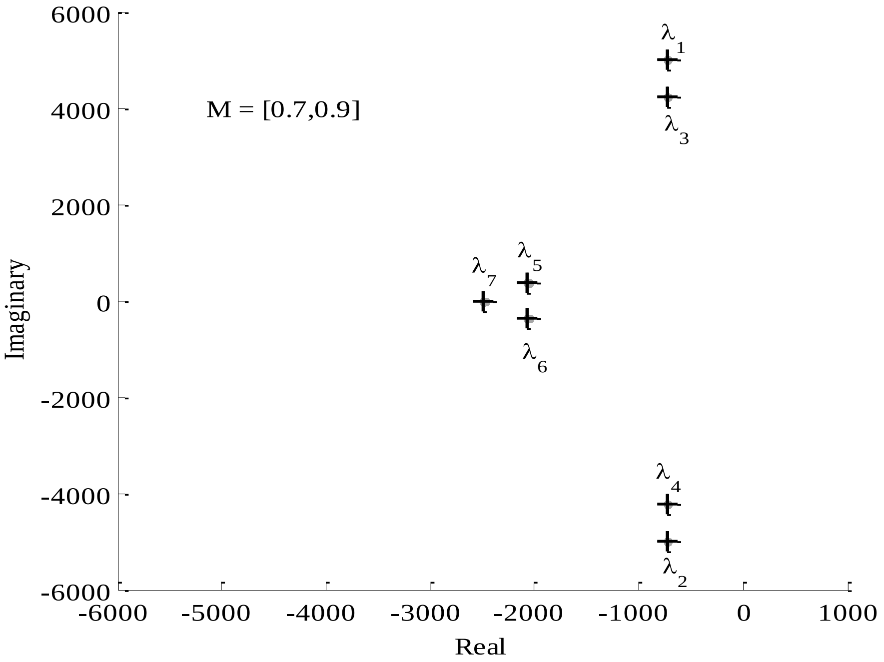

Figure 4-11: Eigenvalues Response to Change in Modulation Index, M (Stand-Alone)

4.3.2 Sensitivity Analysis of Grid-Tied Small-Signal Model

This subsection studies the eigenvalues sensitivity analysis for the three-phase SVPWM VSI under grid-tied mode. The parameters of the system to be analyzed are given in Table 4-3 and the initial eigenvalues locations of the system are given Table 4-4. As shown in Table 4-4, the system has a single negative real value and three complex pair values on the LHS of the complex plane, so the system is initially stable.

Table 4-3: Eigenvalues Sensitivity Analysis Parameters Analysis (Grid-Tied)

Parameter	Nominal Value
C	$4000\ uF$
R_1	0.1 Ω
L_1	2.5 mH
R_f	0.5 Ω
C_f	$10\ uF$
R_g	2 Ω
$L_2 + L_g$	4 mH
M	0.9
Φ	-30°

Table 4-4: Initial Eigenvalues in the Complex Plane (Grid-Tied)

Eigenvalue	Location
$\lambda_{1,2}$	$-162.7 \pm j5024.6$
$\lambda_{3,4}$	$-162.8 \pm j4270.7$
$\lambda_{5,6}$	$-327.3 \pm j377.6$
λ_7	-2491.1

A) Sensitivity of DC Bus Capacitance, C

Eigenvalues response to increasing DC bus capacitance from $2000\ uF$ to $6000\ uF$ is shown in Figure 4-12 in which cross signs (+) indicate the locations of eigenvalues corresponding to nominal values of systems parameters given in Table 4-3. As it can be seen from Figure 4-12, only one eigenvalue, λ_1, is sensitive to changes in C. Increasing the DC capacitance moved λ_1 to the left. Therefore, increasing the DC capacitance improves the systems stability. In general, larger capacitance on the DC side of the inverter reduces the systems vulnerability to changes in voltage, thereby ensuring a more stable operation.

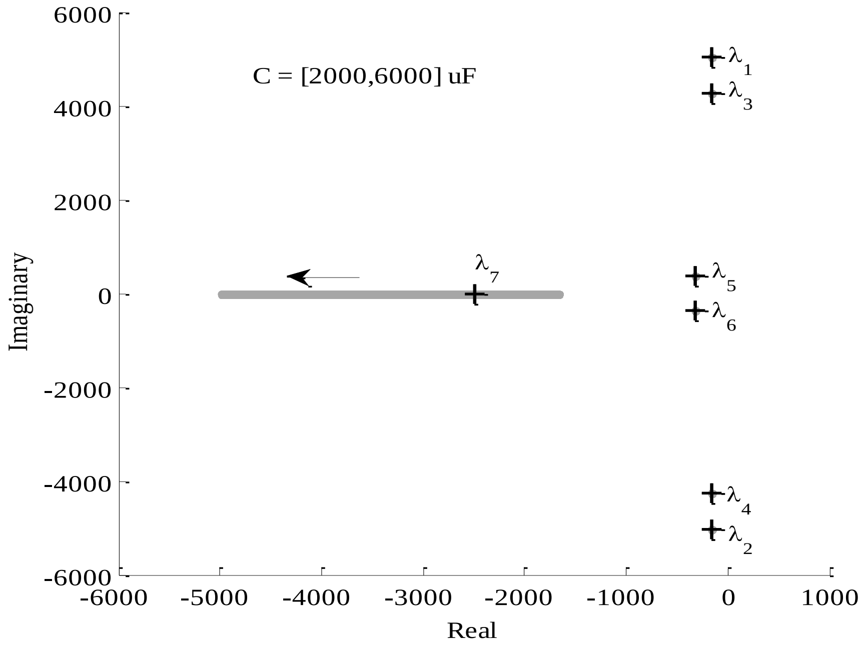

Figure 4-12: Eigenvalues Response to Change in DC Bus Capacitance, C (Grid-Tied)

B) Sensitivity of LCL Filter Inductor, L_1

Response of the system eigenvalues to increasing the value of L_1 from 1.5 mH to 4.5 mH is shown in Figure 4-13. While the value of L_1 is critically important from for higher harmonics filtering, the increase in the value of L_1 hinders the systems stability. As shown in Figure 4-13, increasing L_1 moved $\lambda_{1,2}$, $\lambda_{3,4}$, and $\lambda_{5,6}$ towards the RHS of the complex plane.

C) Sensitivity of Damping Resistor, R_f

System response to increasing R_f from 0 to 5Ω is shown in Figure 4-14. Increasing R_f moved $\lambda_{1,2}$, and $\lambda_{3,4}$ away from the imaginary axis. Therefore, it improves the system stability. Although R_f is desirable for higher harmonics damping, larger values of R_f increases the losses at fundamental frequency.

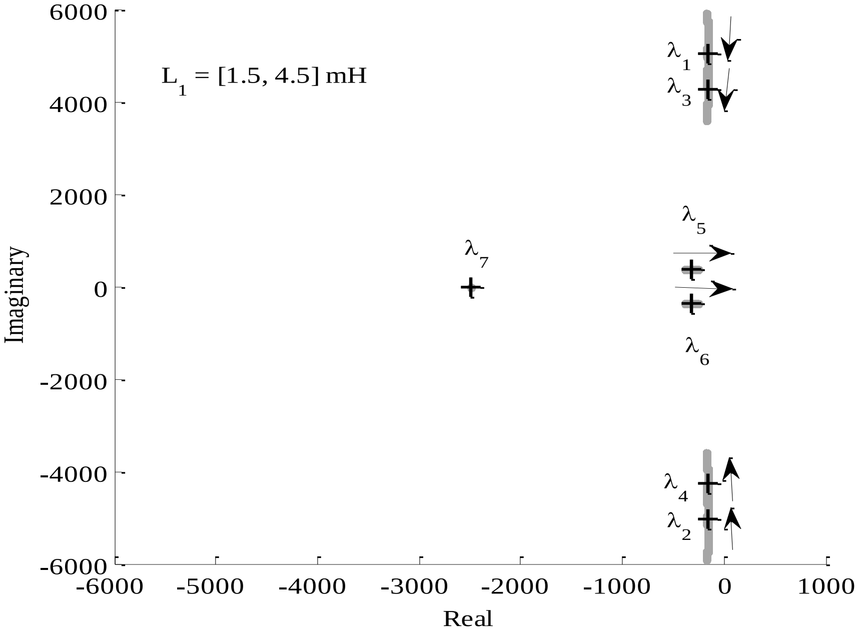

Figure 4-13: Eigenvalues Response to Change in LCL Filter Inductor, L_1 (Grid-Tied)

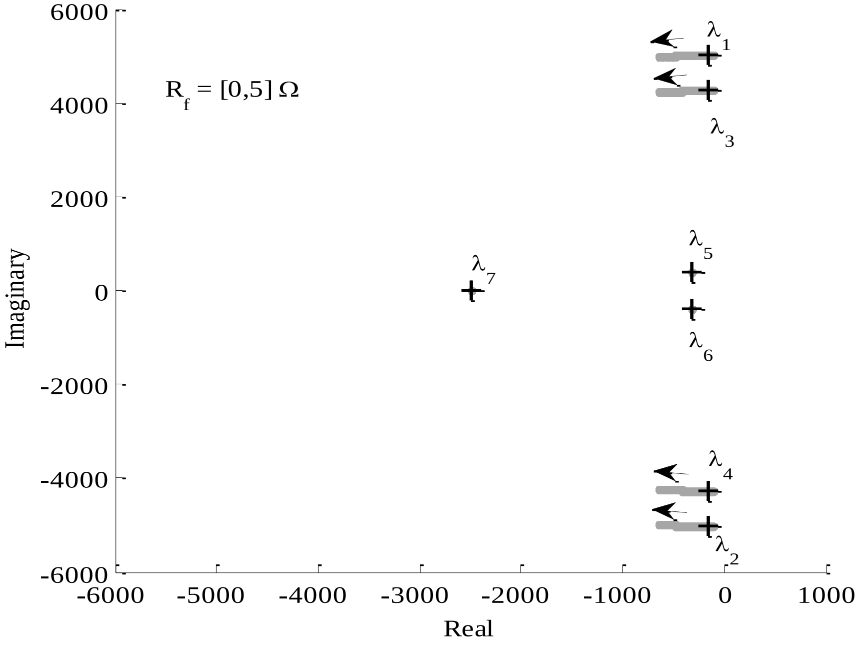

Figure 4-14: Eigenvalues Response to Change in Damping Resistor of LCL Filter, R_f (Grid-Tied)

D) Sensitivity of LCL Capacitor, C_f

Response of eigenvalues to increasing the LCL filter capacitor from 5 to $15\,uF$ is shown in Figure 4-15. As C_f increased, the locations of $\lambda_{1,2}$ and $\lambda_{3,4}$ moved vertically toward the real axis and the locations of $\lambda_{5,6}$ and λ_7 remained unchanged. Therefore, increasing C_f does not impact the systems stability.

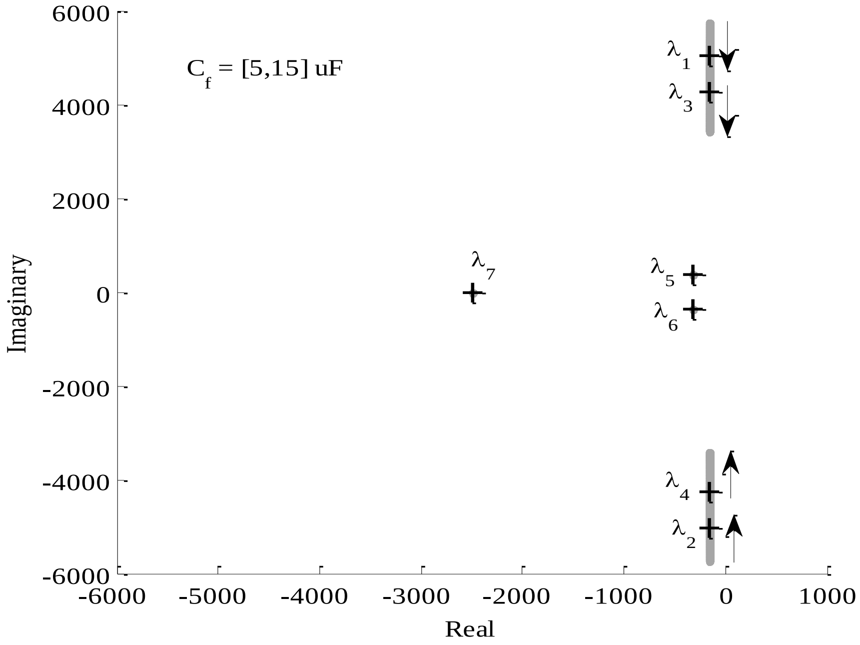

Figure 4-15: Eigenvalues Response to Change in the LCL Capacitor, C_f (Grid-Tied)

E) Sensitivity of Grid Resistance, R_g

System response to an increase in the resistance of the grid from 0 to $5\,\Omega$ is shown in Figure 4-16. As R_g increased, the locations of $\lambda_{1,2}$, $\lambda_{3,4}$, and $\lambda_{5,6}$ moved toward LHS of the complex plane, thereby making the system more stable.

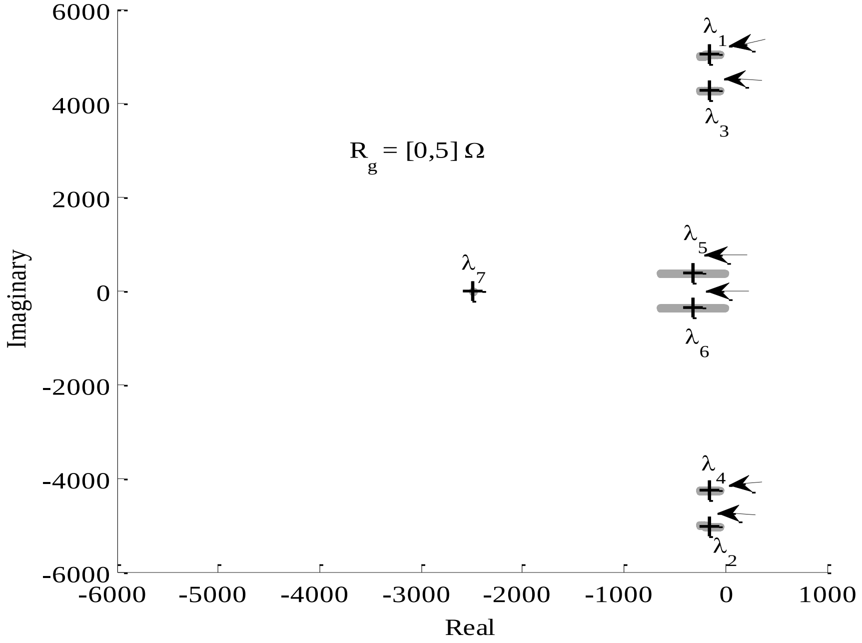

Figure 4-16: Eigenvalues Response to Change in Grid Resistance, R_g (Grid-Tied)

F) Sensitivity of LCL filter Inductor and Grid Inductance, $L_2 + L_g$

System response to increasing the inductance of the filter and the grid are shown in Figure 4-17. The locations of $\lambda_{1,2}$ and $\lambda_{3,4}$ moved toward the origin and the locations of $\lambda_{6,7}$ moved horizontally to the right. However, the location of λ_7 remained unchanged. Therefore, increasing $L_2 + L_g$ hinders the systems stability.

G) Sensitivity of Modulation Index, M

The effect of increasing the modulation index, *M*, from 0.8 to 1 on the system eigenvalues is shown in Figure 4-18. As it can be seen in Figure 4-18, the eigenvalues of the system are not affected by varying M.

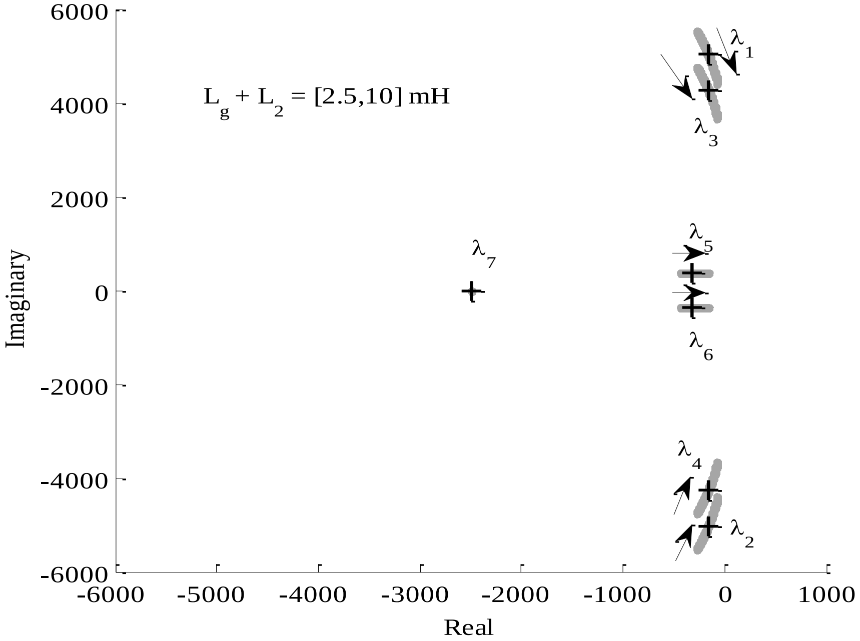

Figure 4-17: Eigenvalues Response to Change Load Inductance and Filter Inductance, $L_2 + L$ (Grid-Tied)

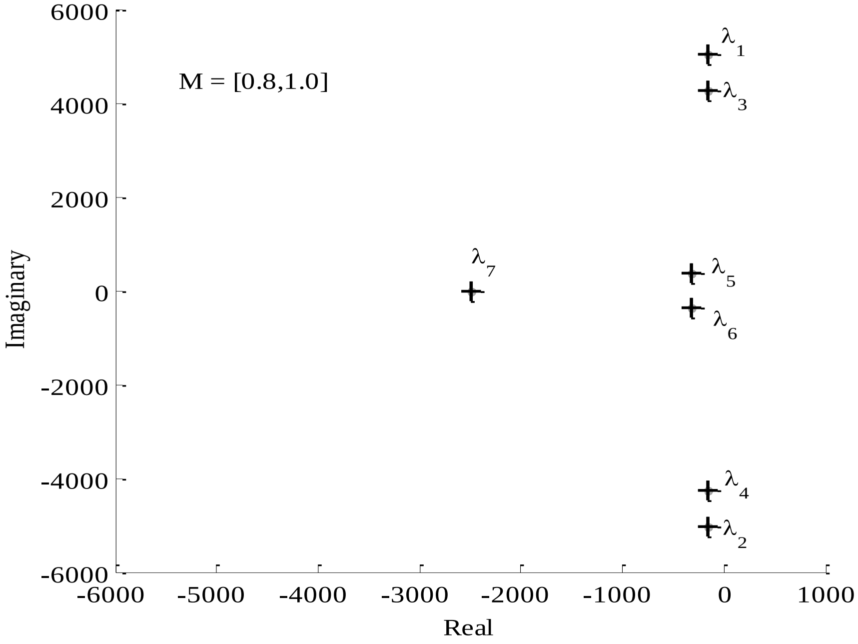

Figure 4-18: Eigenvalues Response to Change in Modulation Index, M (Grid-Tied)

H) Sensitivity of Phase Angle, Φ

The effect of increasing the phase angle, Φ, from -60° to 0 on the systemeigenvalues is shown in Figure 4-19. As shown in the figure, the eigenvalues of the system are not affected by varying Φ. Therefore, variations in Φ do not impact the system stability.

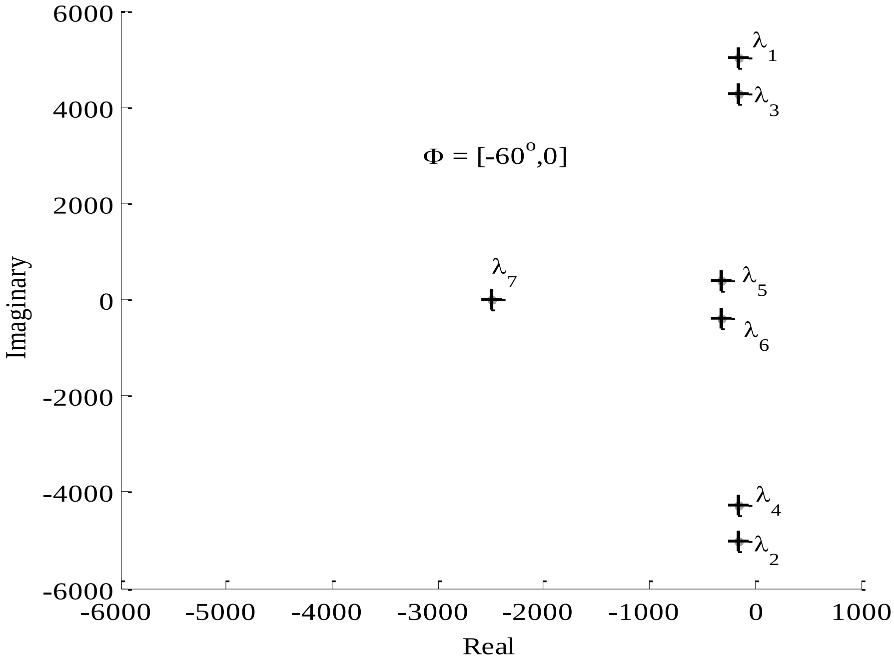

Figure 4-19: Eigenvalues Response to Change in Phase Angle, Φ (Grid-Tied)

Chapter 5 - Model Verification through Simulation and Experiments

In this chapter, the large-signal model and the small-signal model of the three-phase SVPWM VSI under stand-alone and grid-tied modes are verified via Matlab/Simulink simulations and lab experiments. Fortunately, Matlab/Simulink has a designated block that simulates SVPWM gate pulses generation. Moreover, Matlab/Simulink has another dSpace specific SVPWM block, $DS1103\_DSP\_PWMSV$, that generates SVPWM gate pulses with specified dead-time through the PWM I/O serial port of dSpace. Both blocks are used in this thesis. The results of the simulations and experiments are compared against the developed models to determine their accuracy. For experimental verification, a three-phase VSI in an industrial motor drive made by Rockwell Automation is used. The motor drive was donated to Dr. Mirafzal by Rockwell Automation for research purposes. With Dr. Mirafzal permission, the drive was modified to be externally controlled by dSpace instead of its internal control system.

Section 5.1, which contains two subsections, provides verification of the large-signal and small-signal model of the three-phase SVPWM VSI under stand-alone mode. Subsection 5.1.1 discusses the verification through Matlab/Simulink simulation and Subsection 5.1.2 discusses the experimental verification. Section 5.2, which is also divided into two subsections, contains verification of the large-signal and small-signal model of the three-phase SVPWM VSI under grid-tied mode. Subsection 5.2.1 discusses verification through Matlab/Simulink simulation and Subsection 5.2.2 discusses the experimental verification. Finally, Section 5.3 concludes this chapter and presents some closing remarks.

5.1 Stand-Alone Models Verification

In this section, the large signal-model and the small signal model, (4-39) and (4-43) respectively, of the three-phase SVPWM VSI under stand-alone mode are verified using simulation and experiments.

5.1.1 Verification through Simulation

The circuit of the three-phase VSI connected to a local load through an LCL filter, as depicted in Figure 4-1, was built in Matlab/Simulink as shown in Figure 5-1. As previously mentioned, the Matlab/Simulink SVPWM block was used in the simulation. The parameters of the SVPWM block along with the other circuit parameters are presented in Table 5-1.

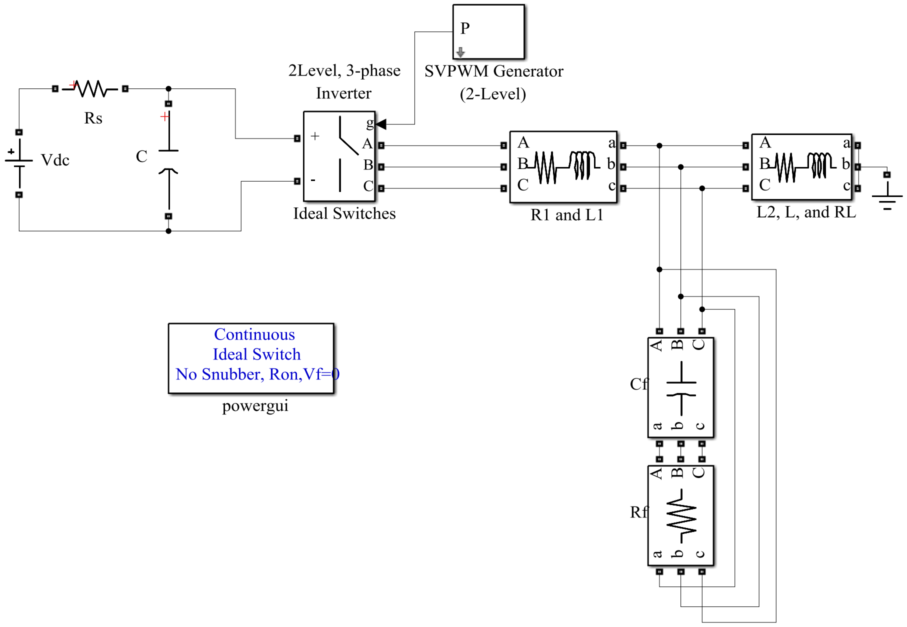

Figure 5-1: SVPWM VSI Matlab/Simulink Simulation (Stand-Alone)

Table 5-1: Simulation Parameters of the Large-Signal Model

Parameter	Value
V_{dc}	350 V
m	0.841
C	4000 uF
L_1	2.5 mH
L_2	2.5 mH
L	0 mH
C_f	10 uF
R_f	0.7 Ω
R_L	20 Ω
f_s	3.6 kHz
f	60 Hz

State variables of the averaged-state-space model specified in Chapter 4 were measured during simulation and transformed into their corresponding dq componenets. Simulation results compared against the large-signal model given by (4-39) are presented in Figure 5-2. As shown in the figure, the model described the start-up slow dynamics and the steady-state operation of the VSI accurately. The behavior of the state variable v_c was described by the averaged-state-space model with almost 100% accuracy. The reason behind that is because v_c is more dependent on the voltage source V_{dc} and less dependent on the inverter output currents i_a and i_b. Since V_{dc} is constant and not effected by the switching behavior of the inverter, the state-space averaging technique has little effect on v_c. Moreover, it can be noticed from the simulation that higher harmonics were present in the rest of the state variables. These harmonics were caused by the switching of the VSI at high frequency. It can be further noticed that rather than describing high frequency phenomena, the averaged-state-space model calculated their average. Therefore, the state-space averaging method is very accurate in describing phenomena at the fundamental frequency (60 Hz) or frequencies lower than the fundamental frequency. However, the state-space averaging method is not accurate in describing phenomena at much higher frequencies. For further illustration, the dq state-space variables are converted back to their corresponding quantities in abc frame of reference and presented in Figure 5-3. It can be seen that the unfiltered VSI output currents ($i_a, i_b,$ and i_c) contained enormous amounts of high frequency harmonics present in the simulation but only their average was reflected by the model.

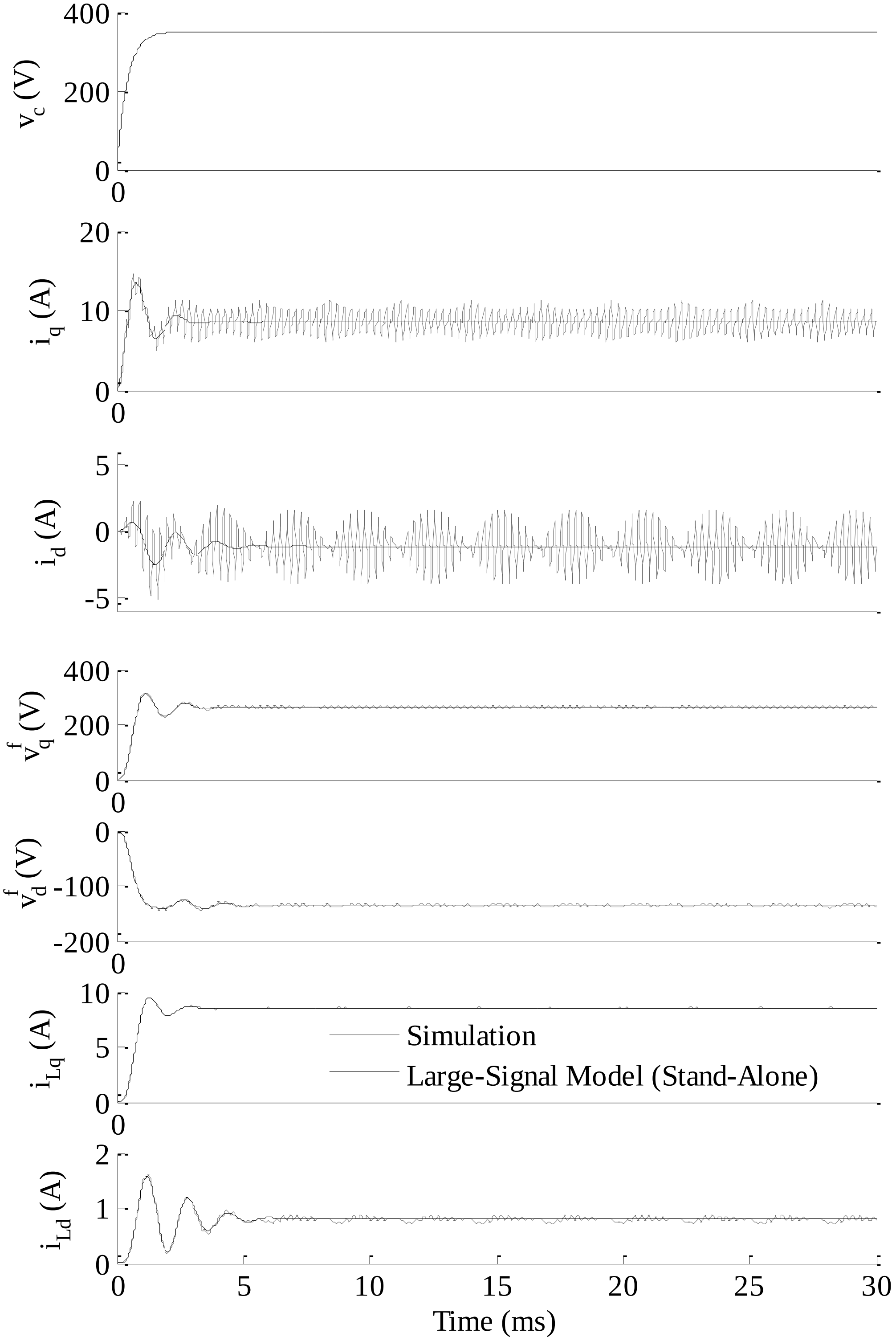

Figure 5-2: Simulation Results Compared Against Large-Signal Model in dq Frame of Reference (Stand-Alone)

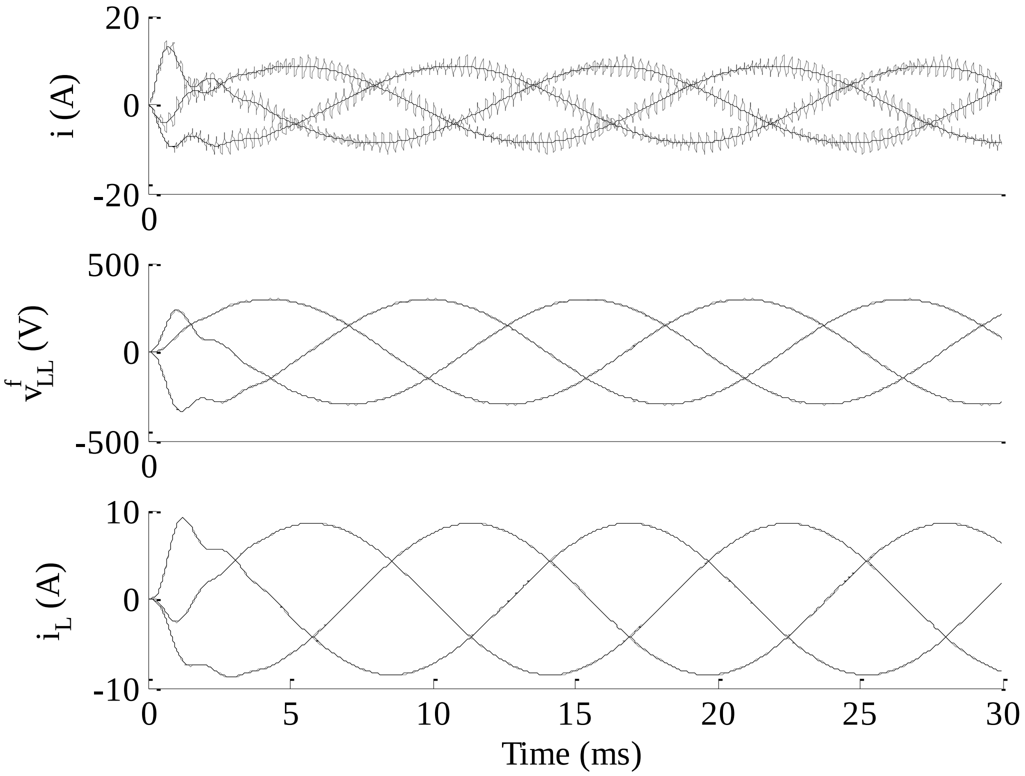

Figure 5-3: Simulation Results Compared Against Large-Signal Model in abc Frame of Reference (Stand Alone)

To verify the small-signal model, another simulation was carried out in which m is increased from 0.841 to 0.941 at $t = 40\,ms$ then decreased to 0.741 at $t = 60\,ms$. Since the small-signal model must be linearized around pre-calculated steady-state operating points, the steady-state operating points of the large-signal simulation are used. The steady-state operating points are: $\tilde{V}_c = 349.4\,A$, $\tilde{I}_q = 8.594\,A$ and, $M = 0.841$. The simulation results compared against the small-signal model in (4-43) are presented in dq frame of reference in Figure 5-4. In addition, the results in abc frame of reference are presented in Figure 5-5. Similar to the large-signal model, the small-signal model is very accurate in describing the VSI slow dynamics and steady state operation.

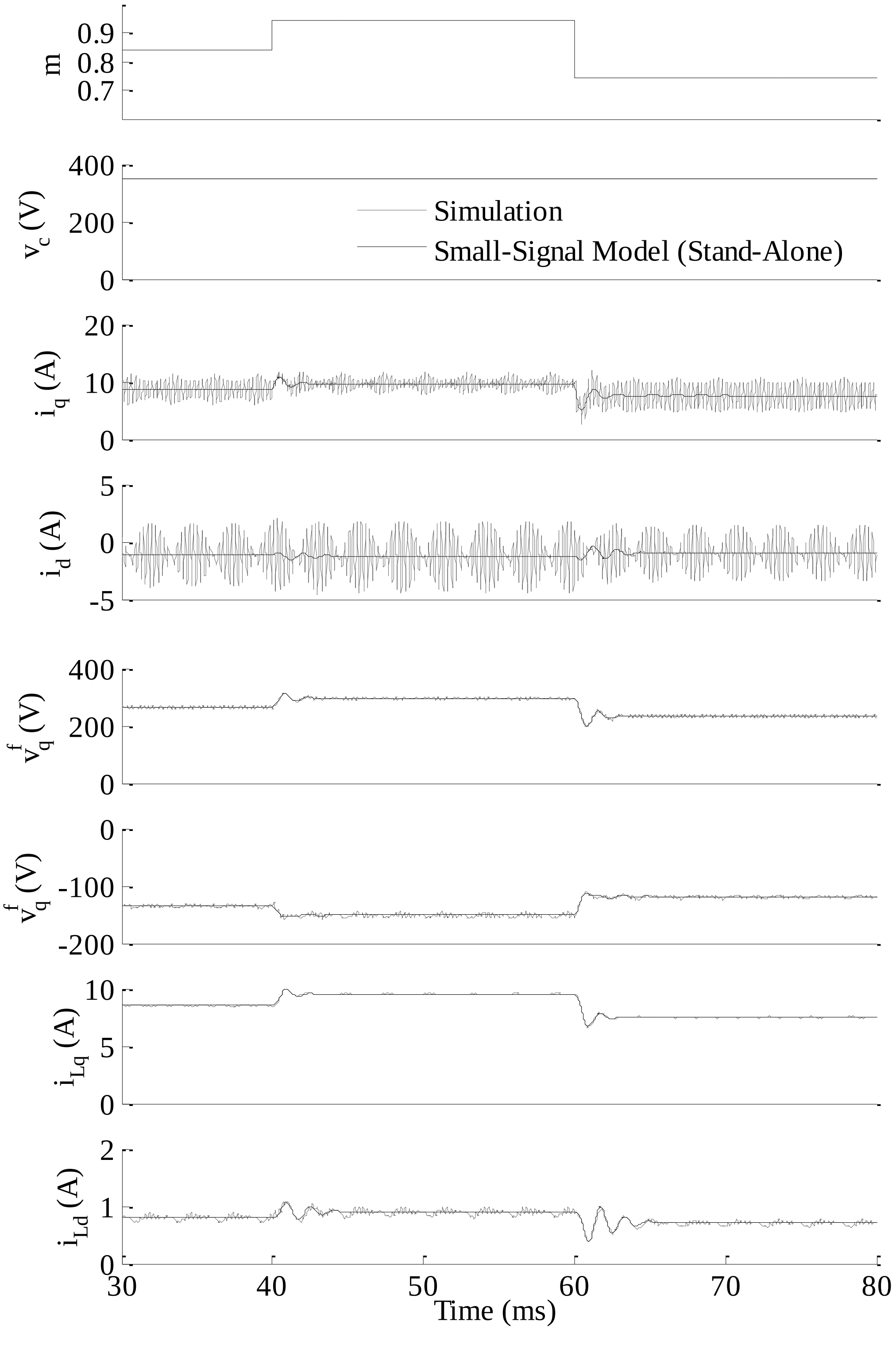

Figure 5-4: Simulation Results Compared Against Small-Signal Model in dq Frame of Reference (Stand-Alone)

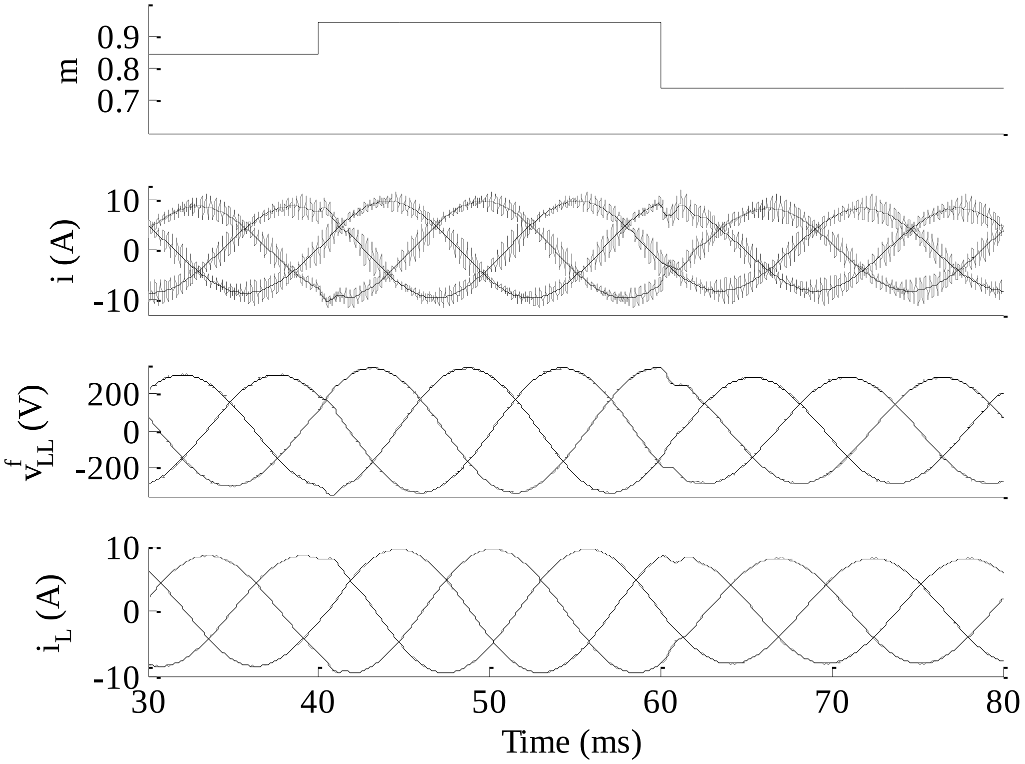

Figure 5-5: Simulation Results Compared Against Small-Signal Model in abc Frame of Reference (Stand-Alone)

5.1.2 Experimental Verification

In this subsection, the averaged-state space models (large-signal and small-signal) of the three-phase VSI under stand-alone conditions are verified through comparison against experimental results. As previously mentioned, a donated Rockwell motor drive was modified to be controlled via Dspace and used as a three-phase SVPWM VSI. Figure 5-6 shows the lab setup used to carry out the experiment. The hardware specifications of the experiment are given in Table 5-3 and the experiment parameters are given in Table 5-2. Due to technical reasons (pre-charging systems in the VSI and the DC power supply), the start-up dynamics of the VSI cannot be properly captured. Instead, state variables measurements were taken when the VSI reached a steady-state operation. The experimental results compared to the large-signal model in (4-39) and presented in dq frame of reference in Figure 5-7. In addition, the rotating state variables are presented in abc frame of reference in Figure 5-8 (since the experimental results of i_a, i_b, and i_c contain a lot of harmonics, they are plotted separately).

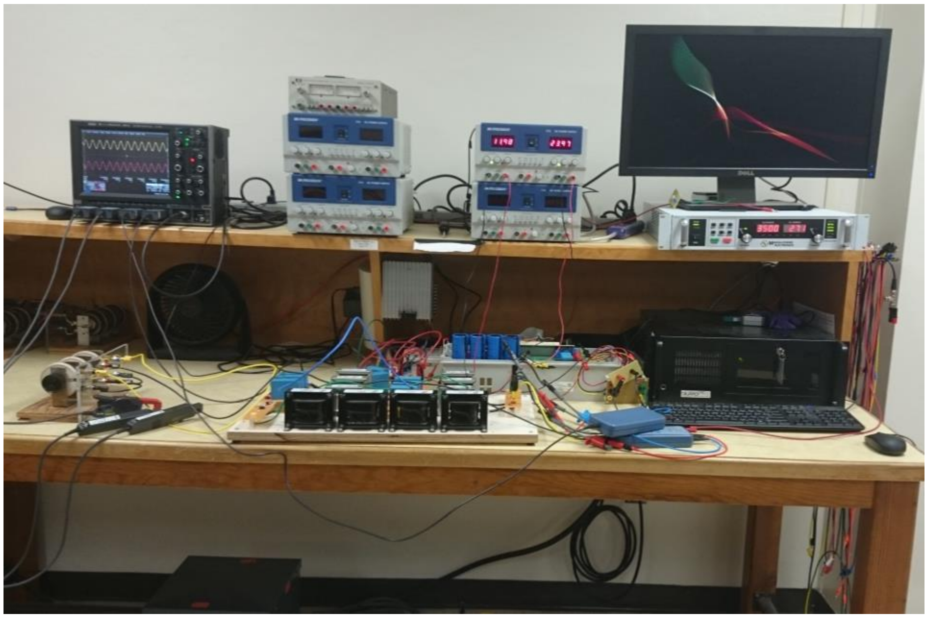

Figure 5-6: Lab Experimental Setup (Stand-Alone)

Table 5-3: Hardware Specifications

Parameter	Value
PWM Generator	CP 1103 dSpace
Switching Frequency	3.6 kHz
Dead Time	2 μs
Sampling Frequency	87 kHz
Input DC Source	XR-II Magna-Power Electronics
Oscilloscope	LeCory Waverunner 64XI-A
Inverter	Rockwell Automation Motor Drive

Table 5-2: Experiment Parameters (Stand-Alone)

Parameter	Value
V_{DC}	350 V
m	0.841
Frequency	60 Hz
C	3858 uF
R_s	0.1 Ω
R_1	0 Ω
L_1	2.5 mH
L_2	2.5 mH
L	0 mH
R_L	100 Ω
C_f	10 uF
R_f	0.7 Ω

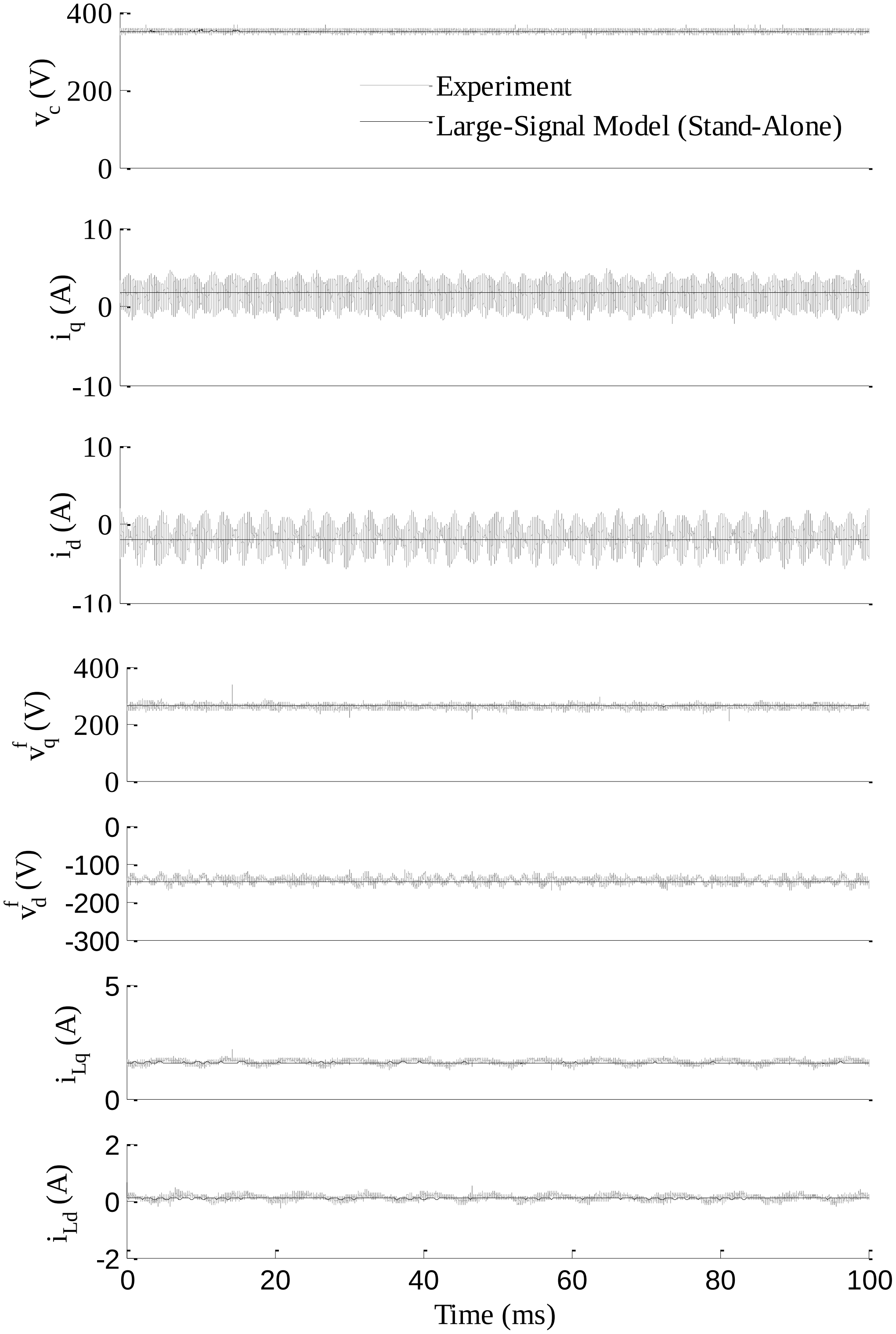

Figure 5-7: Experimental Results Compared Against Large-Signal Model in dq Frame of Reference (Stand-Alone)

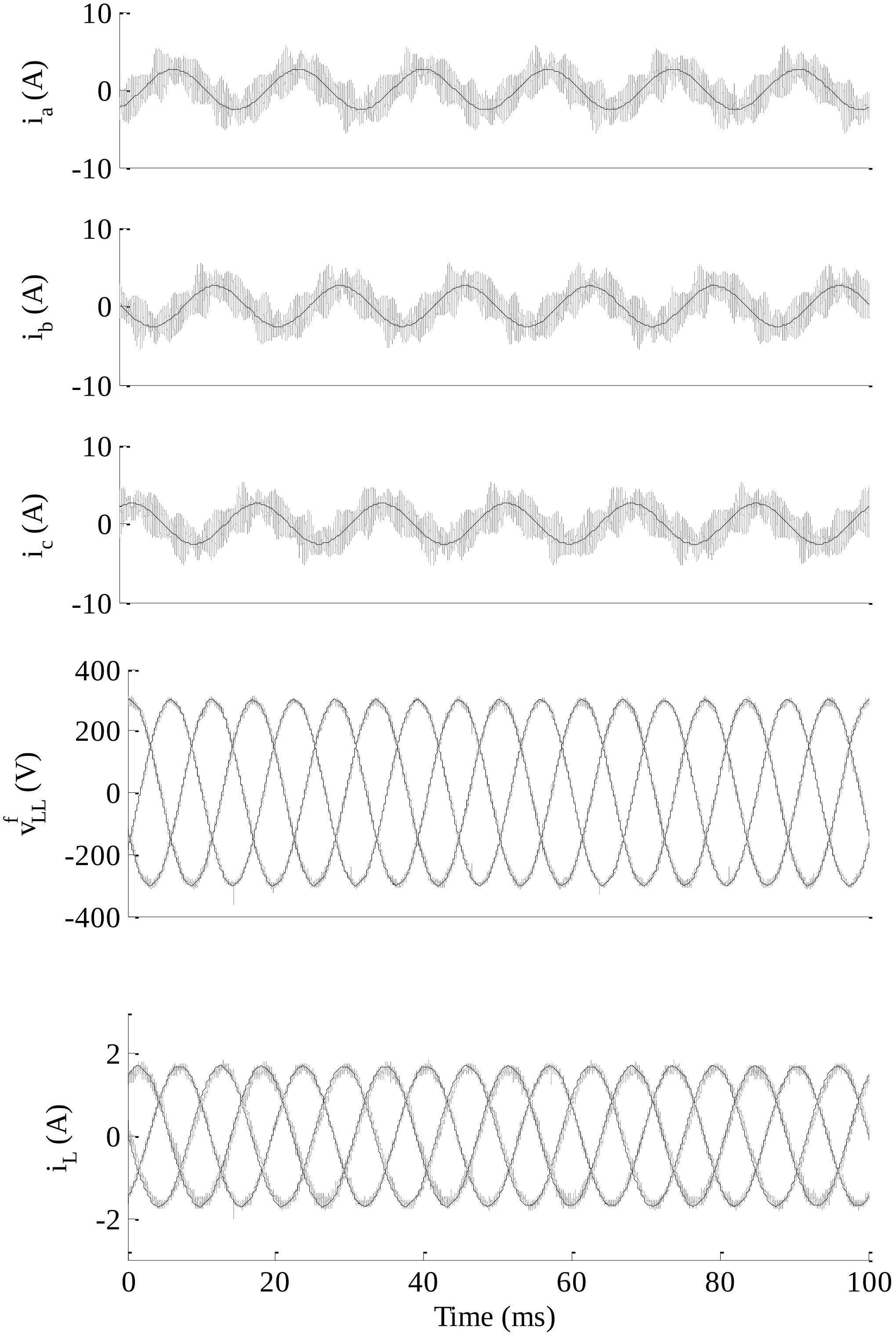

Figure 5-8: Experimental Results Compared Against Large-Signal Model in abc Frame of Reference (Stand Alone)

To verify the small-signal model, the parameters in Table 5-2 were used to carry out another experiment. In this experiment m was increased from 0.85 to 0.95 at $t = 35.2\,ms$ and then decreased to 0.8 at $t = 95.2\,ms$. The small-signal model in (4-43) was linearized around $\tilde{V}_c = 350\,V$, $\tilde{I}_q = 1.75\,A$ and, $M = 0.85$. Experimental results compared against the small-signal model results are presented in dq frame of reference in Figure 5-9. In addition, experimental results are presented in abc frame of reference in Figure 5-10

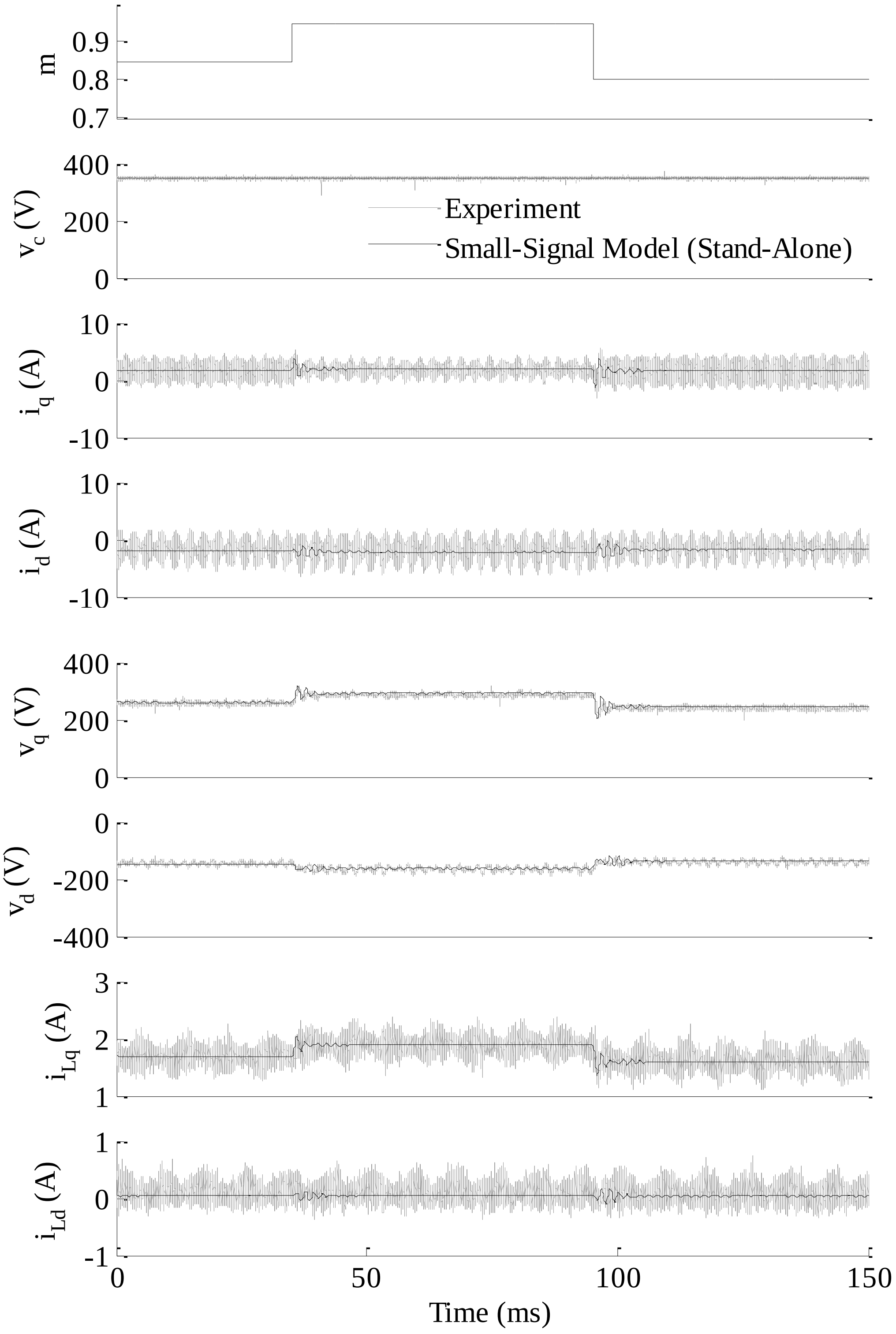

Figure 5-9: Experimental Results Compared Against Small-Signal Model in dq Frame of Reference (Stand-Alone)

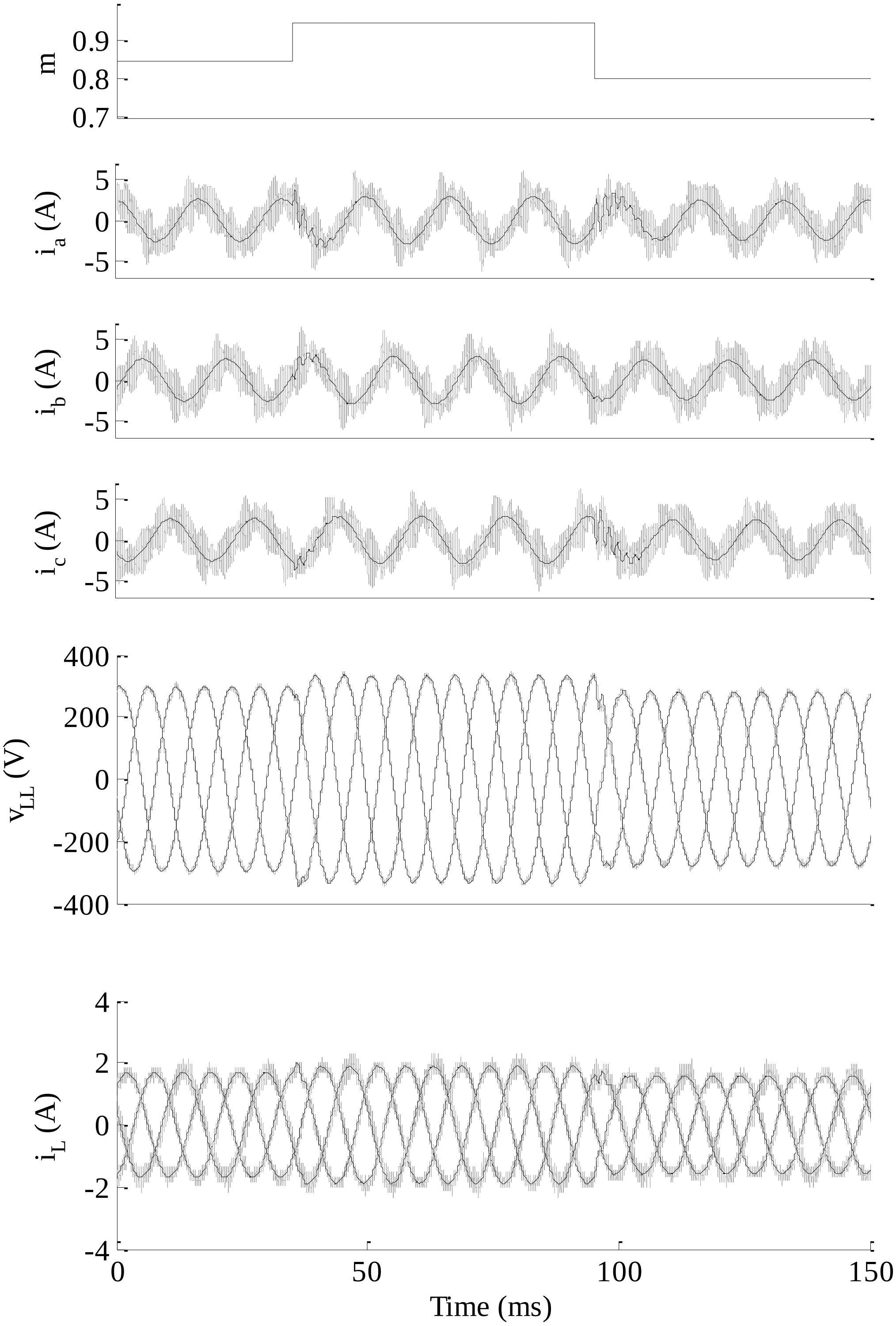

Figure 5-10: Experimental Results Compared Against Small-Signal Model in abc Frame of Reference (Stand-Alone)

5.2 Grid-Tied Models Verification

In this section, the large signal-model (4-72) and the small signal model (4-78) of the three-phase SVPWM VSI under grid-tied mode are verified using Matlab/Simulink simulations and experiments.

5.2.1 Verification through Simulation

In this subsection, the averaged-state-space models (small-signal and large-signal) under grid-tied mode are verified through Matlab/Simulink simulation. The circuit representing the SVPWM VSI in Figure 4-3 was built in Matlab/Simulink as shown in Figure 5-11. The simulation parameters are given in Table 5-4. The simulation results compared to the large-signal model in (4-72) are presented in dq frame of reference in Figure 5-12. In addition, the results in abc frame of reference are presented in Figure 5-13. Similar to the large-signal model developed for the stand-alone case, this model exhibited a great deal of accuracy in describing startup slow dynamics and steady-state behavior.

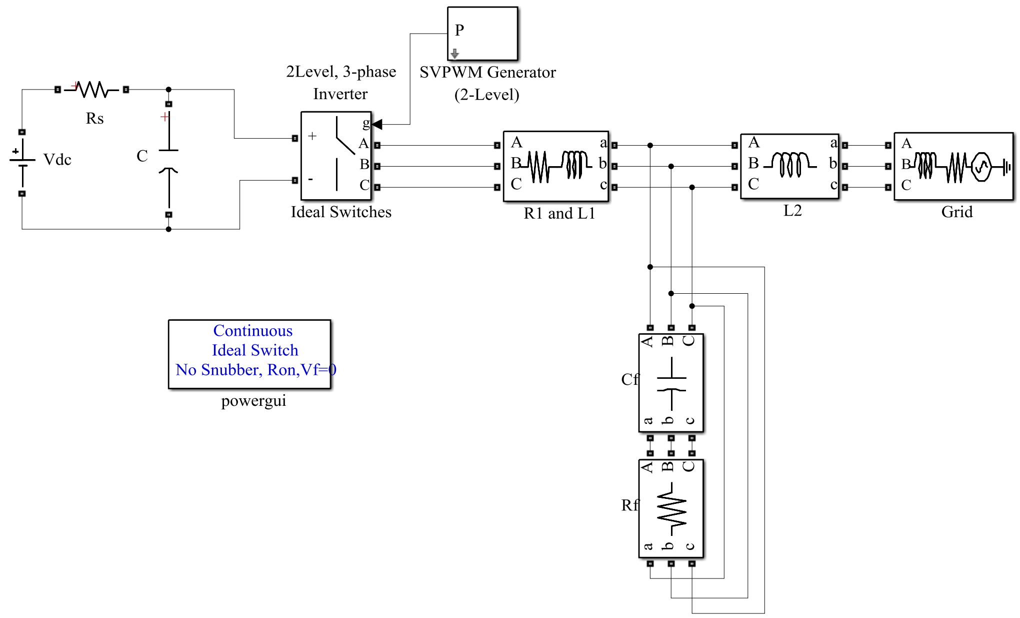

Figure 5-11: SVPWM VSI Matlab/Simulink Simulation (Grid-Tied)

Table 5-4: Simulation Parameters (Grid-Tied)

Parameter	Value
V_{dc}	350 V
m	0.841
C	4000 uF
L_1	2.5 mH
L_2	2.5 mH
R_1	0 Ω
R_2	0 Ω
L_g	2 mH
C_f	10 uF
R_f	0.7 Ω
R_g	3 Ω
f_s	3.6 kHz
f	60 Hz
ϕ	-30°

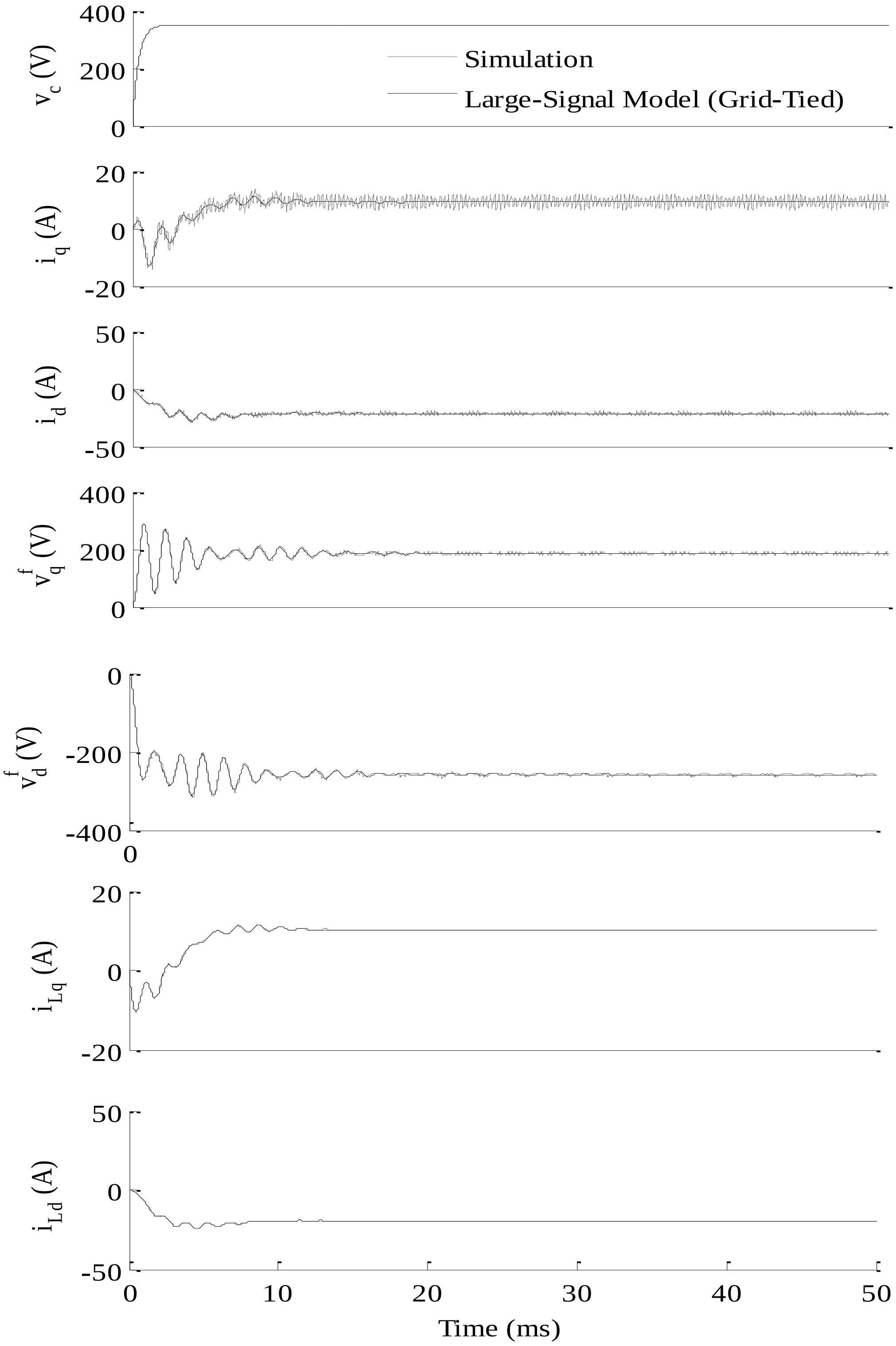

Figure 5-12: Simulation Results Compared Against Large-Signal Model in dq Frame of Reference (Grid-Tied)

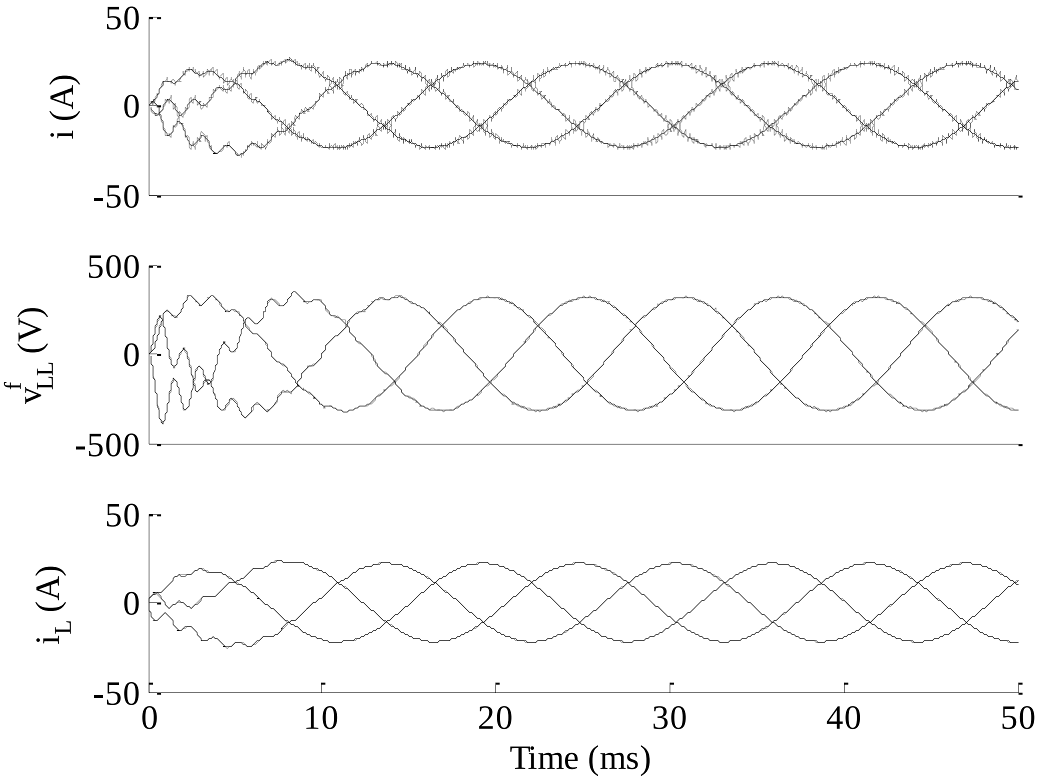

Figure 5-13: Simulation Results Compared Against Large-Signal Model in abc Frame of Reference (Grid-Tied)

To verify the small-signal-model in (4-78) a simulation was carried out in which ϕ was varied during the simulation. The same parameters in Table 5-4 were used and the model was linearized around the steady-state operating points of the simulation in Figure 5-12. The steady-state operating points are: $\tilde{V}_c = 348.6\,A$, $\tilde{I}_q = 9.233\,A$, $\tilde{I}_d = -21.48\,A$, $M = 0.841$, and $\Phi = -30^{\circ}$. In this simulation, ϕ was decreased from -30° to -33° at $t = 40\,ms$ then increased to -27° at $t = 65\,ms$. The simulation results compared against the small-signal model are presented in dq frame of reference in Figure 5-14. In addition, the results are presented in abc frame of reference in Figure 5-15.

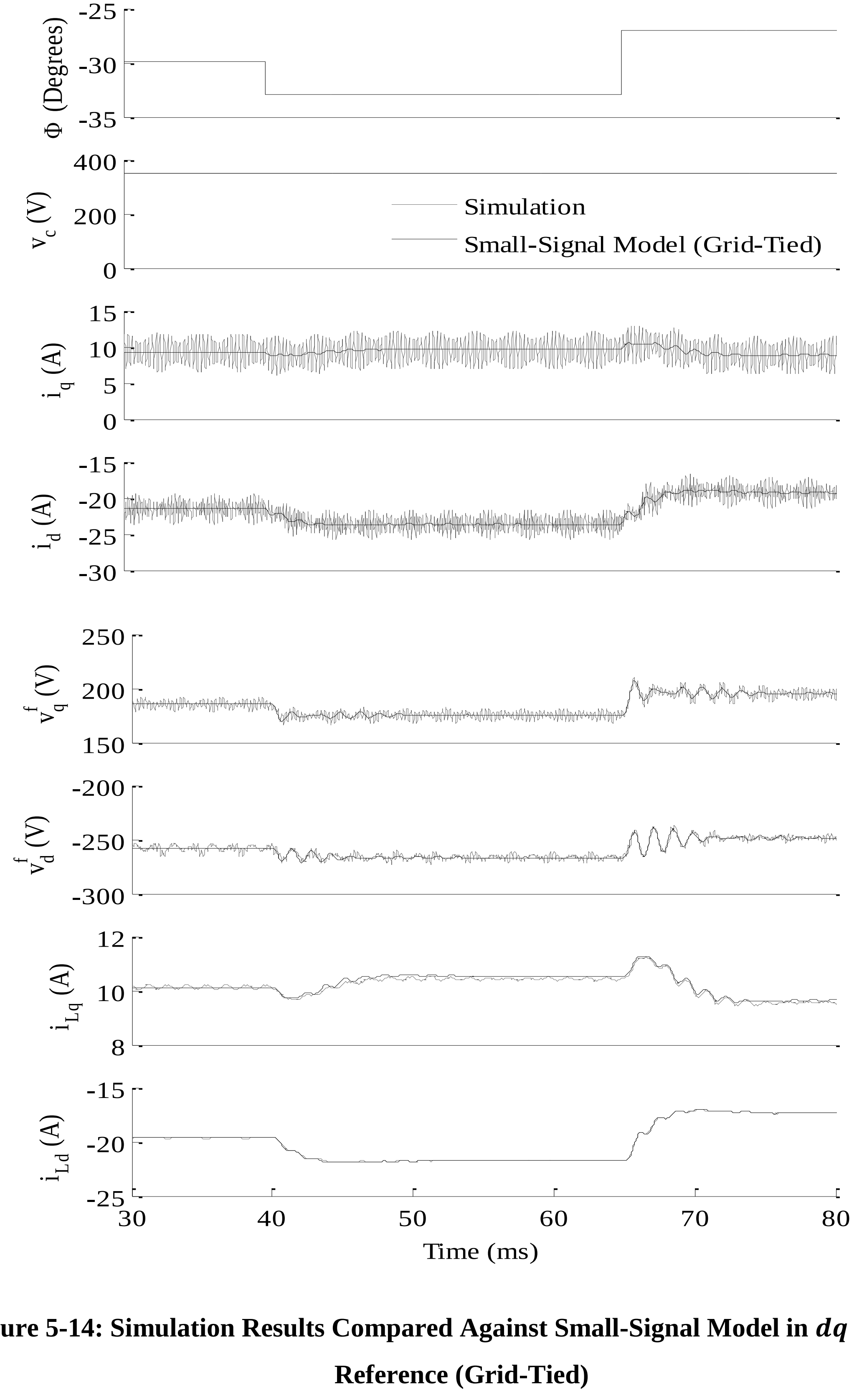

Figure 5-14: Simulation Results Compared Against Small-Signal Model in dq Frame of Reference (Grid-Tied)

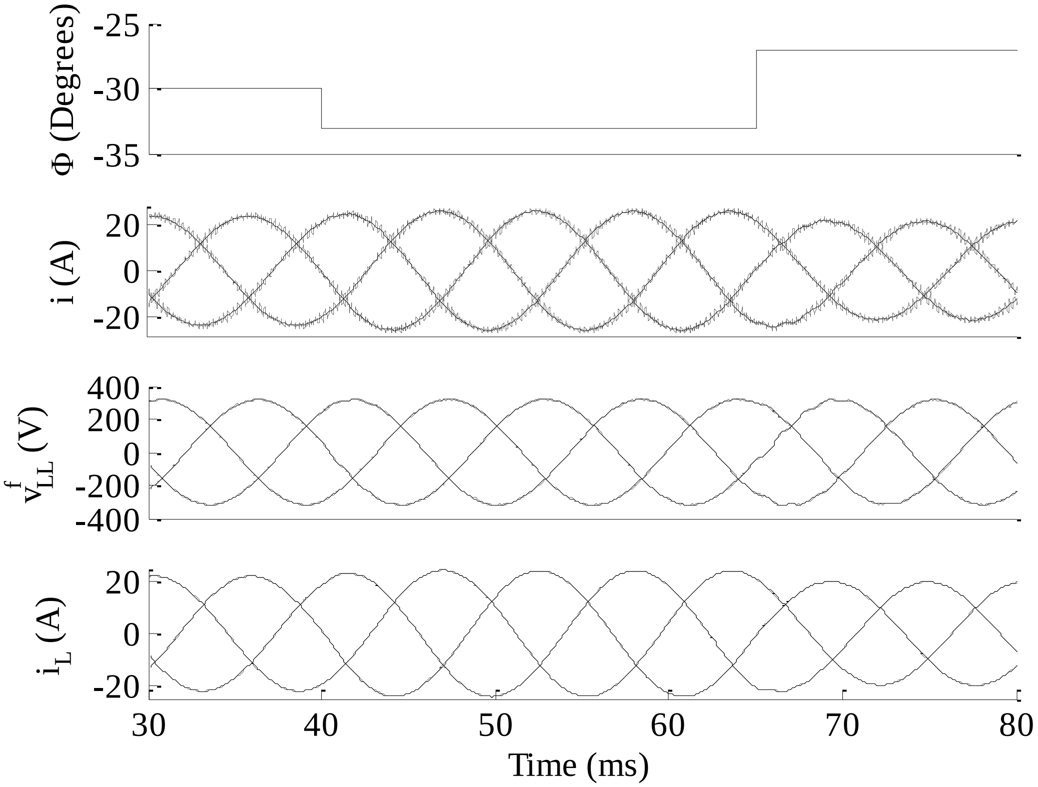

Figure 5-15: Simulation Results Compared Against Small-Signal Model in abc Frame of Reference (Grid-Tied)

5.2.2 Experimental Verification

In this subsection, the averaged-state-space models derived in Chapter 4 (Large-signal and Small-Signal) for the three-phase SVPWM VSI under grid-tied mode are verified through comparison against experimental results. In addition to the hardware used to carry out experiments under stand-alone mode in the previous section, four hardware items were added to carry out these experiments. First, an isolation signal transformer is needed to safely feed dSpace the grid angle in real time. For this purpose, *International Transformers 14A-2.5R-12* signal transformer is used in a simple voltage divider circuit (to step down the grid line-to-line voltage) as shown in Figure 5-15. Second, for the protection of the VSI, a 5 kVA Westinghouse isolation transformer is used to isolate the VSI from the grid. The isolation transformers data are given in Figure 5-17. Finally, an additional 10 mH inductance between the inverter and the grid is added.

The purpose of this inductance is to limit the current injected to the grid, since the purpose of this experiment is to test the accuracy of the model rather than the capabilities of the inverter. The hardware specifications and the experiments parameters are presented in Table 5-5 and Table 5-6, respectively.

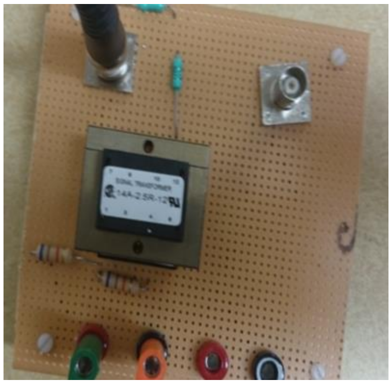

Figure 5-16: Grid Angle Feedback Circuit

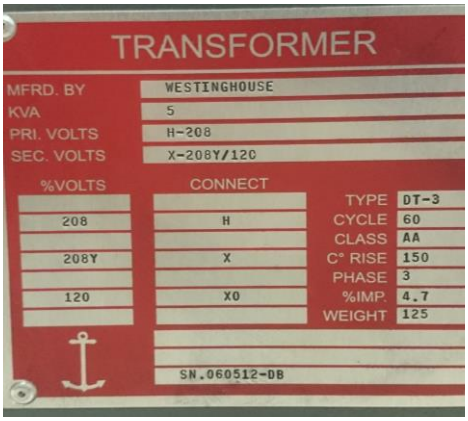

TRANSFORMER

MFRD. BY WESTINGHOUSE
KVA 5
PRI. VOLTS H-208
SEC. VOLTS X-208Y/120

%VOLTS	CONNECT
208	H
208Y	X
120	X0

TYPE DT-3
CYCLE 60
CLASS AA
C° RISE 150
PHASE 3
%IMP. 4.7
WEIGHT 125

SN.060512-DB

Figure 5-17: Isolation Transformer Data

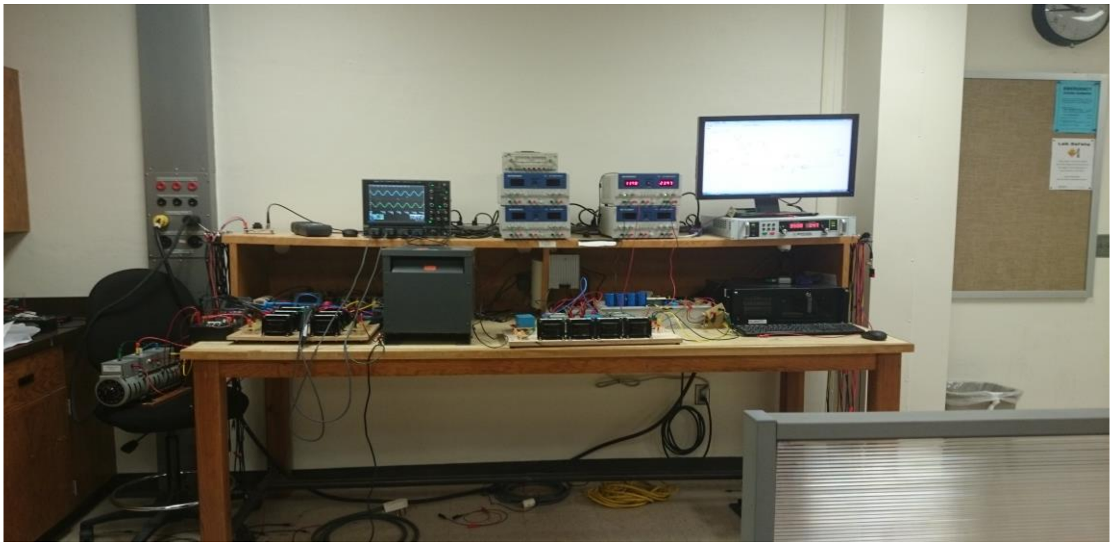

Figure 5-18: Experiment Setup (Grid-Tied)

Table 5-5: Hardware Specifications (Grid-Tied)

Parameter	Value
PWM Generator	CP 1103 dSpace
Switching Frequency	3.6 kHz
Sampling Frequency	87 kHz
Dead-Time	2 μs
Input DC Source	XR-II Magna-Power Electronics
Oscilloscope	LeCory Waverunner 64XI-A
VSI	Rockwell Automation Motor Drive
Signal transformer	International Transformers 14A-2.5R-12
Isolation Transformer	5 kVA Westinghouse Transformer

Table 5-6: Experiment Parameters (Grid-Tied)

Parameter	Value
V_{DC}	350 V
m	0.841
Frequency	60 Hz
C	3858 uF
R_s	0.1 Ω
L_1	2.5 mH
L_2	2.5 mH
L_g	11.1 mH
C_f	10 uF
R_f	0.7 Ω
R_1	0 Ω
R_g	3 Ω
ϕ	-7°

In this experiment, the actual grid inductance was assumed to be zero. However, L_g represents the isolation transformer inductance (which comes out to be $1.1\,mH$) and the additional inductance between the grid and the inverter ($10\,mH$). The complete experiment set up is shown in Figure 5-18. Using the parameters in Table 5-6, the experiment was carried out. Experimental results compared to the large-signal model in (4-72) are presented in dq frame of reference in Figure 5-19.

From Figure 5-19, two important observations should be noted. First, the model description of the steady-state operation of the VSI is satisfactory. Second, the experimental results have additional harmonics at various frequencies. Some of these harmonics are at frequencies closer to 60 Hz. While other harmonics are at higher frequencies, some of them are caused by the switching of the inverter. However, the majority of these harmonics are orginated from the grid. The THD of the line currents was 4.4 %, compared to 1% in the stand-alone experiment. The averaged-state-space-model does not describe high frequencies phenomena accurately, as previously discussed. Therefore, it can be noticed that lower frequencies phenomena caused by the grid is reflected on the model while higher frequency phenomena are not. For further illustration, the experimental results compared to the large-signal model in abc frame of reference are presented in Figure 5-20.

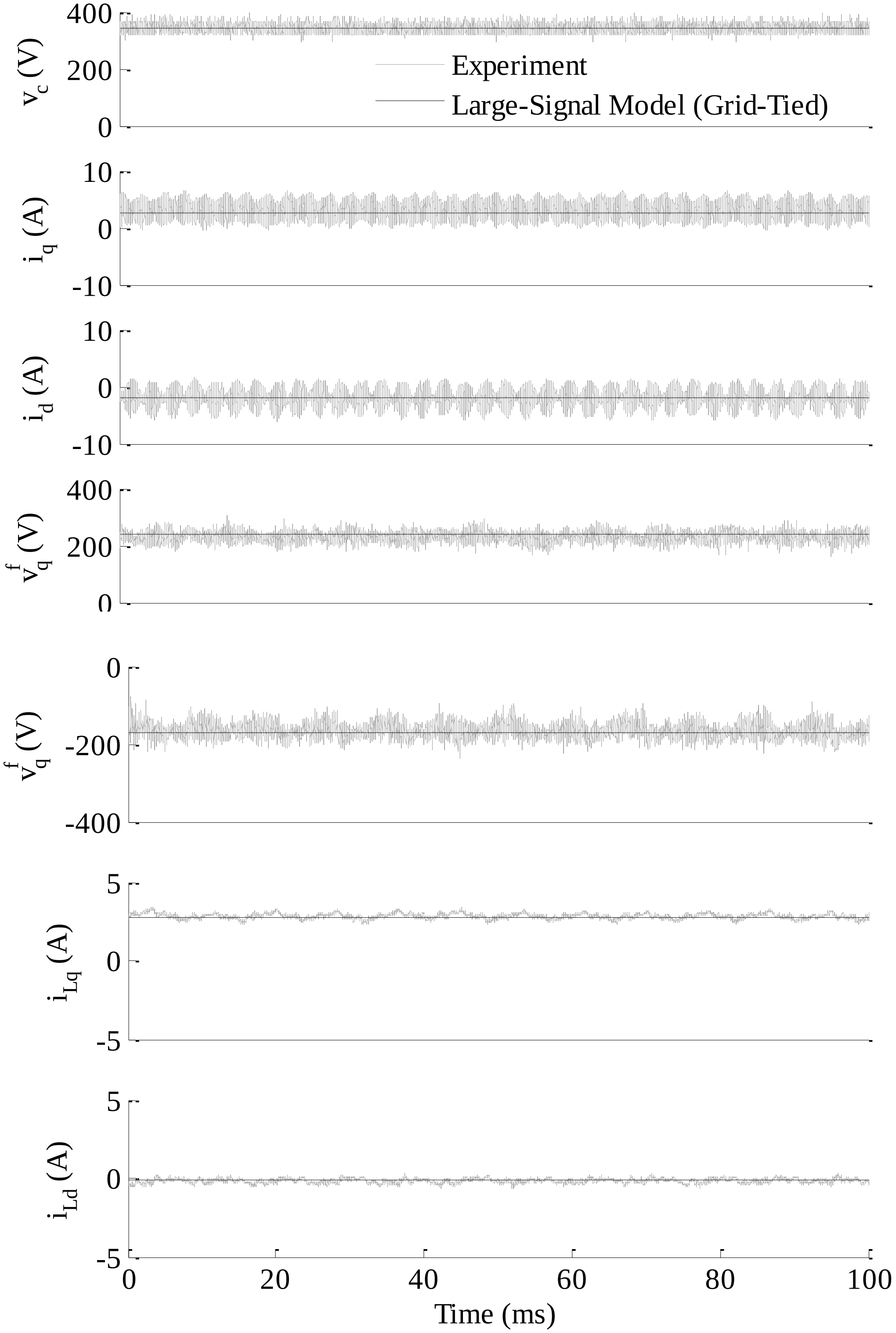

Figure 5-19: Experimental Results Compared Against Large-Signal Model in dq Frame of Reference (Grid-Tied)

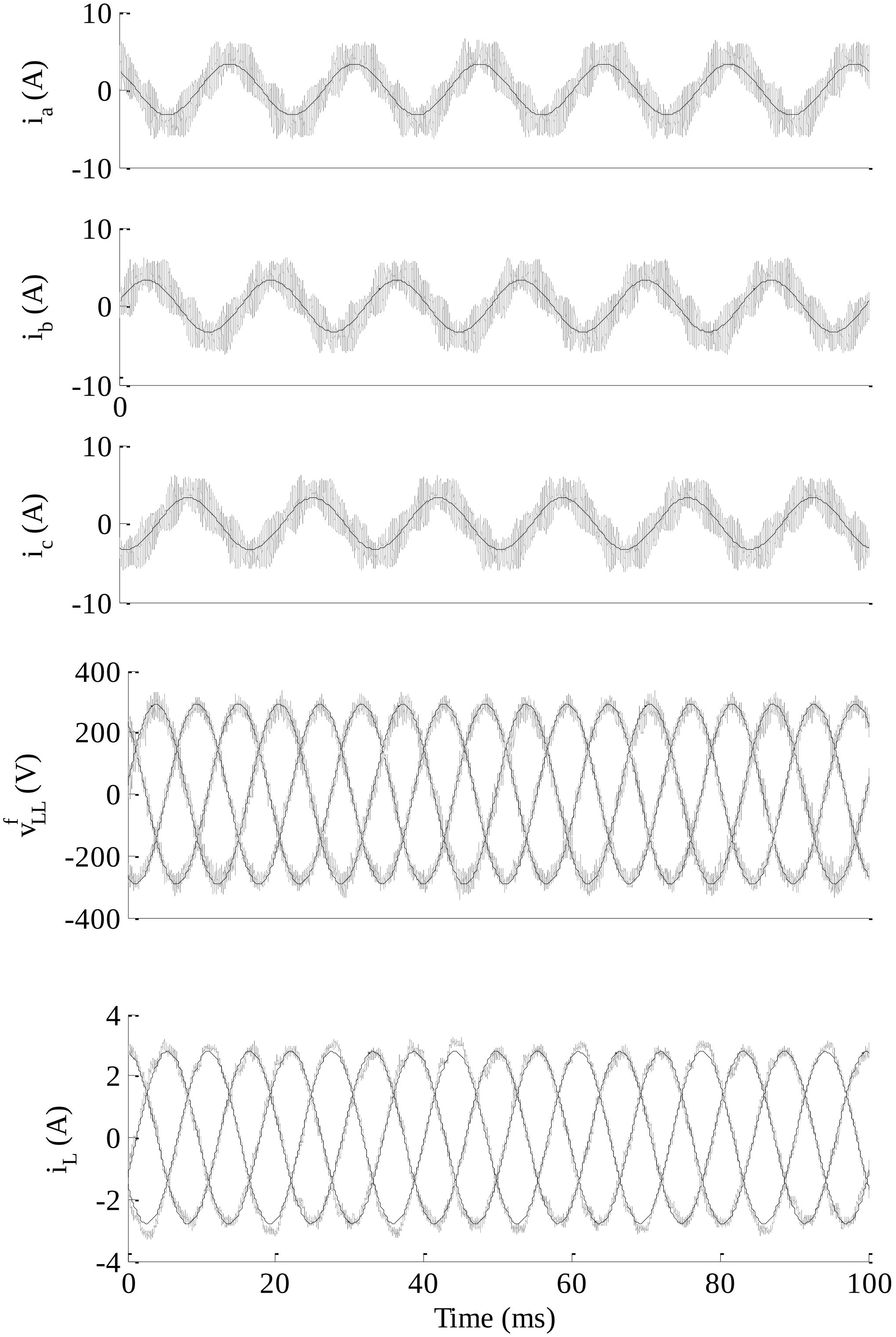

Figure 5-20: Experimental Results Compared Against Large-Signal Model in abc Frame of Reference (Grid-Tied)

To verify the small-signal-model in (4-78) another experiment was carried out in which ϕ was decrease from -7° to -10° at $t = 52\ ms$. The same parameters in Table 5-6 were used and the model was linearized around the steady-state operating points of the large-signal model in Figure 5.20. The steady-state operating points are: $\tilde{V}_c = 347$, $\tilde{I}_q = 2.58$, $\tilde{I}_d = -2.02$, $M = 0.841$, and $\Phi = -7^{\circ}$. Experimental results compared against the small-signal model are presented in dq frame of reference in Figure 5-21. In addition, the results in abc frame of reference are presented in Figure 5-22

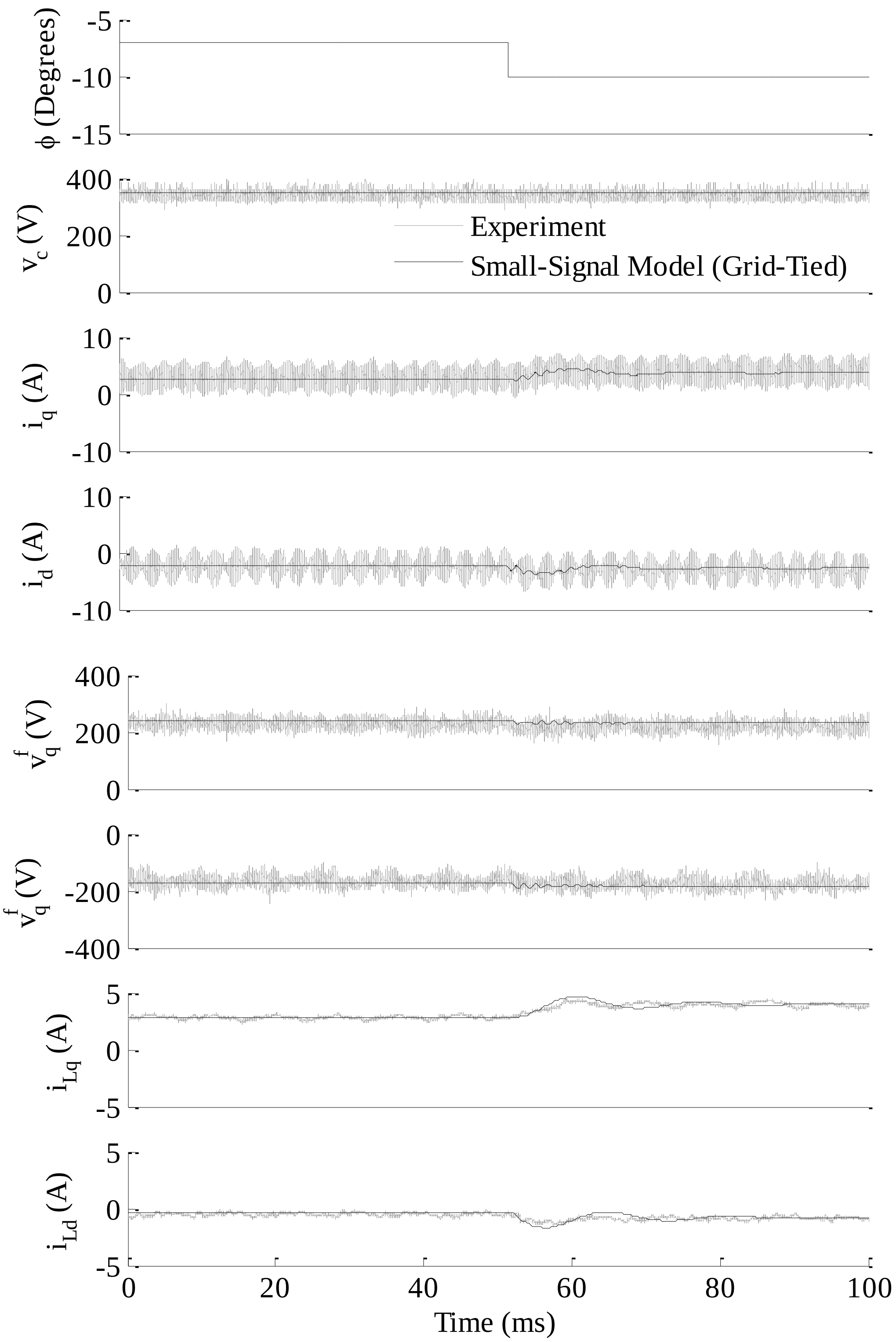

Figure 5-21: Experimental Results Compared Against Small-Signal Model in dq Frame of Reference (Grid-Tied)

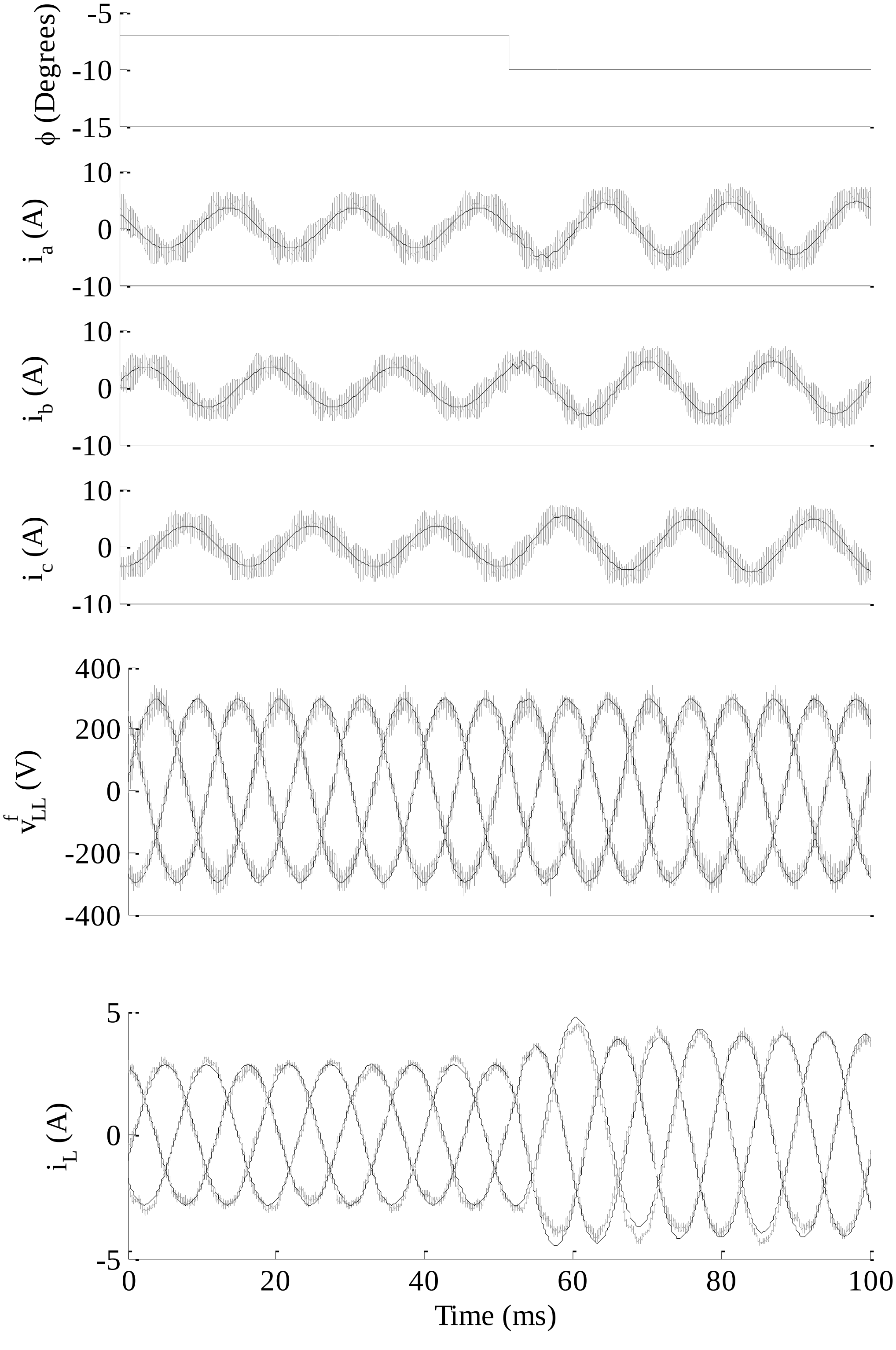

Figure 5-22: Experimental Results Compared Against Small-Signal Model in abc Frame of Reference (Grid-Tied)

5.3 Conclusion and Closing Remarks

In this chapter, the averaged-state-space models of the three-phase SVPWM VSI under stand-alone and grid-tied modes were successfully verified through Matlab/Simulink simulations and lab experiments. The Matlab/Simulink simulation results showed that the models can accurately describe the startup dynamics, the transient dynamics, and the steady-state behavior of the VSI. Similarly, the models exhibited a great deal of accuracy when compared to experimental results. However, the differences between the model and the experimental results were more noticeable (especially the grid-tied experimental results). These differences are caused by practical non-idealities that are not considered by the model. These practical non-idealities can be summarized as follows:

i. Presence of parasitic inductance, within the VSI circuit, the LCL filter, and external wires
ii. Implementation of snubber circuits to protect the switches from voltage spikes
iii. Voltage drops across the switches
iv. Implementation of dead-time, to prevent shorting the DC bus
v. Distortion caused by the grids non-idealities (only for grid-tied)

Chapter 6 - Conclusion and Future Work

This chapter presents a summary of work carried out in this thesis. The chapter also includes a few suggestions on the use of the developed averaged-state-space-models. This chapter has two sections. Section 6.1 presents a summary of the contributions of thesis and Section 6.2 presents a few suggestions for future work.

6.1 Conclusion

In this thesis, the state-space averaging method was applied to the three-phase SVPWM VSI to obtain dynamic models for the SVPWM VSI under stand-alone and grid-tied modes. The thesis began with an introductory chapter in which the background of the problem, the contribution of the thesis, and the organization of the thesis are thoroughly discussed. In Chapter 2, different three-phase PWM switching techniques were discussed. Their advantages and disadvantages were outlined. From Chapter 2 concluded that the SVPWM is the most efficient PWM technique for two reasons: SVPWM provides better utilization of the DC bus voltage, and implementation of SVPWM requires less computation. Chapter 3 discussed the black-box modeling method and the state-space averaging modeling method. Chapter 3 concluded that the state-space averaging method is far more comprehensive and less complicated compared to the black-box modeling method. The reference-frame theory was also discussed in Chapter 3. In Chapter 4, the mathematical implementation of the state-space averaging method to derive dynamic models of the SVPWM VSI was thoroughly discussed. Large-signal and small-signal models were derived for stand-alone and grid-tied modes. In addition, the small-signal models were used to carry out eigenvalues sensitivity analysis. In Chapter 5, the developed models were verified through Matlab/Simulink simulations and lab experiments.

6.2 Future Work

As previously mentioned, the developed models are tools that can be used in the design and analysis of the three-phase SVPWM VSI. The small-signal model of the averaged-state-space model under stand-alone mode in (4-43) can be used to design voltage regulation systems for the VSI. Since the VSI modulation index, m, is one of the models inputs and the VSI output voltages, v_q^f and v_d^f, are state variables, a transfer function can be obtained with the VSI modulation index as an input and the VSI output currents as outputs. This transfer function can be used to design and optimize a PID controller-based voltage regulation system. Similarly, the small-signal model in (4-77) can be used to design a power control system for the three-phase VSI under grid-tied mode. Since the phase angle of the output voltage, ϕ, is one of the model inputs and the VSI output currents, $i_{L_q}$and i_{L_d}, are state variables, a transfer function with the output voltage phase angle as an input and the output currents as outputs can be obtained. This transfer function can be used to design a controller that tracks target power requirements.

In addition to their use as design and analysis tools, the developed models can be used as simulation tools. Due to the increase in adapting RES to generate electric power, the number of VSIs connected to the electric grid is rapidly increasing. Using software simulation packages to simulate large number of VSIs require large amount of computation time. For systems level simulation purposes, only slow dynamics and steady-state operation are needed. In other words, high frequency switching transients are neglected. Therefore, the developed models of the three-phase VSI under grid-tied mode are ideal fast alternatives to detailed simulation obtained by software simulation packages.

In addition to investigating the possibilities of solving existing design problems using the models developed in this thesis, the developed models can be further improved as follow:

- Developed models were derived for three-phase balanced systems. Therefore, the developed models cannot be used to analyze the behavior of the VSI under unbalanced conditions. Following the same procedure adapted in this thesis to develop averaged-state-space models that can accommodate non-balanced conditions would yield more practical models.
- Developed models do not consider the dead-time implemented in VSIs. Fortunately the VSI used for the experimental verification is an IGBT-based VSI. Since IGBTs are fast switching devices, the required dead-time is very short ($2\ \mu s$) and its effect did not cause any significant mismatch between the model and the experimental results. However, longer dead-time is required in slow switching devices, possibly hindering the model accuracy. To eliminate this possibility dead-time should be incorporated into the models.

- Developed models did not include snubber circuits. Devloping models that include the snubber circuit components would improve the models accuracy in describing the behavior of the VSI. In addition, it would assess the effect of snubber circuits on the overall stability of the system, through eigenvalues sensitivity analysis.

References

[1] American Wind Energy Association, "Wind Generation Records & Turbine Productivity," American Wind Energy Association, 2013.

[2] SEIA; GTM, "U.S. Solar Market Insight Report 2013 Year-in-Review," SEIA & GTM, 2014.

[3] R.D. Middlebrook and S. Cuk, "A general unified approach to modeling switching-converter power stages," in *IEEE Power Electronics Specialists Conference* , 1976, pp. 18-34.

[4] Muhammad H. Rashid, *Power Electronics: Circuits, Devices, and Applications* , 4th ed. United States : Pearson , 2013.

[5] D. Grahame and Thomas A. Lipo, *Pulse Width Modulation for Power Converters*, Mohammed E. El-Hawary, Ed. USA: A John Wiley & Sons, Inc , 2003.

[6] Mohan, Undeland, and Robbins, *Power Electronics: Converters, Applications, and Design* , 2nd ed.: John Wiley & Sons, Inc.

[7] V. Valdivia et al., "Simple Modeling and Identification Procedures for “Black-Box” Behavioral Modeling of Power Converters Based on Transient Response Analysis ," *IEEE Transactions on Power Electronics*, vol. 24, no. 12, pp. 2776-2790, Dec 2009.

[8] Luis Amedo, R. Burgos, F. Wang, and D Boroyevich, "Black-Box Terminal Characterization Modeling of DC-to-DC Converters," in *Applied Power Electronics Conference, APEC 2007 - Twenty Second Annual IEEE*, 2007, pp. 457-463.

[9] V. Valdivia et al., "Black-Box Behavioral Modeling and Identification of DC–DC Converters With Input Current Control for Fuel Cell Power Conditioning," *IEEE Transactions on Industrial Electronics* , vol. 61, no. 4, pp. 1891-1903, April 2014.

[10] V. Valdivia et al., "Black-Box Modeling of Three-Phase Voltage Source Inverters for

System-Level Analysis," *IEEE Transactions on Industrial Electronics*, vol. 59, no. 9, pp. 3648-3662, Sept 2012.

[11] R. D. Middlebrook and Slobodan Cuk, "A General Unified Approach To Modeling Switching-Converter Power Stages ," in *IEEE Power Electronics Specialists Conference* , Cleveland, 1976, pp. 73-84.

[12] N. Kroutikova, C.A. Hernandez-Aramburo, and T.C. Green, "State-space model of grid-connected inverters under current control mode," *Electric Power Applications, IET*, vol. 1, no. 3, pp. 329-338, May 2007.

[13] H. Kanaan, K. Al-Haddad, and F. Fnaiech, "Modelling and control of three-phase/switch/level fixed-frequency PWM rectifier: state-space averaged model," *Electric Power Applications, IEE Proceedings*, vol. 152, no. 3, pp. 551-557, May 2005.

[14] A.K. Kaviani, Kang Yen, and B. Mirafzal, "Dynamic model of three-phase current source boost inverter for stand-alone applications," in *Applied Power Electronics Conference and Exposition (APEC)*, 2012, pp. 18-24.

[15] A.K. Kaviani and B. Mirafzal, "Dynamic model of the three-phase single-stage boost inverter for grid-connected applications," in *Energy Conversion Congress and Exposition (ECCE)*, 2012, pp. 4627-4634.

[16] William L. Brogan, *Modern Control Theory* , 3rd ed.: Pearson, 2011.

[17] R.H. Park, "Two-reaction theory of synchronous machines generalized method of analysis-part I," *American Institute of Electrical Engineers*, vol. 48, no. 3, pp. 717-727, July 1929.

[18] T.C.Y. Wang, Zhihong Ye, Gautam Sinha, and Xiaoming Yuan, "Output filter design for a grid-interconnected three-phase inverter," in *Power Electronics Specialist Conference, 2003*, 2003, pp. 779-784.

Appendix A: State Space Representations of SVPWM Switching States

A) Stand-Alone:

$$A_{000}=\begin{bmatrix}\frac{-1}{CR_s} & 0 & 0 & 0 & 0 & 0 & 0\\ 0 & \frac{-(3R_1+R_f)}{3L_1} & 0 & \frac{-2}{3L_1} & \frac{-1}{3L_1} & \frac{R_f}{3L_1} & 0\\ 0 & 0 & \frac{-(3R_1+R_f)}{3L_1} & \frac{1}{3L_1} & \frac{-1}{3L_1} & 0 & \frac{R_f}{3L_1}\\ 0 & \frac{1}{3C_f} & \frac{-1}{3C_f} & 0 & 0 & \frac{-1}{3C_f} & \frac{1}{3C_f}\\ 0 & \frac{1}{3C_f} & \frac{2}{3C_f} & 0 & 0 & \frac{-1}{3C_f} & \frac{-2}{3C_f}\\ 0 & \frac{R_f}{3(L_2+L)} & 0 & \frac{2}{3(L_2+L)} & \frac{1}{3(L_2+L)} & \frac{-3R_L-R_f}{3(L_2+L)} & 0\\ 0 & 0 & \frac{R_f}{3(L_2+L)} & \frac{-1}{3(L_2+L)} & \frac{1}{3(L_2+L)} & 0 & \frac{-3R_L-R_f}{3(L_2+L)}\end{bmatrix},B_{000}=\begin{bmatrix}\frac{1}{CR_s}\\ 0\\ 0\\ 0\\ 0\\ 0\\ 0\end{bmatrix}$$

$$A_{100}=\begin{bmatrix}\frac{-1}{CR_s} & \frac{-1}{C} & 0 & 0 & 0 & 0 & 0\\ \frac{2}{3L_1} & \frac{-(3R_1+R_f)}{3L_1} & 0 & \frac{-2}{3L_1} & \frac{-1}{3L_1} & \frac{R_f}{3L_1} & 0\\ \frac{-1}{3L_1} & 0 & \frac{-(3R_1+R_f)}{3L_1} & \frac{1}{3L_1} & \frac{-1}{3L_1} & 0 & \frac{R_f}{3L_1}\\ 0 & \frac{1}{3C_f} & \frac{-1}{3C_f} & 0 & 0 & \frac{-1}{3C_f} & \frac{1}{3C_f}\\ 0 & \frac{1}{3C_f} & \frac{2}{3C_f} & 0 & 0 & \frac{-1}{3C_f} & \frac{-2}{3C_f}\\ 0 & \frac{R_f}{3(L_2+L)} & 0 & \frac{2}{3(L_2+L)} & \frac{1}{3(L_2+L)} & \frac{-3R_L-R_f}{3(L_2+L)} & 0\\ 0 & 0 & \frac{R_f}{3(L_2+L)} & \frac{-1}{3(L_2+L)} & \frac{1}{3(L_2+L)} & 0 & \frac{-3R_L-R_f}{3(L_2+L)}\end{bmatrix},B_{100}=B_{000}$$

$$A_{110}=\begin{bmatrix} \frac{-1}{CR_s} & \frac{-1}{C} & \frac{-1}{C} & 0 & 0 & 0 & 0 \\ \frac{1}{3L_1} & \frac{-(3R_1+R_f)}{3L_1} & 0 & \frac{-2}{3L_1} & \frac{-1}{3L_1} & \frac{R_f}{3L_1} & 0 \\ \frac{1}{3L_1} & 0 & \frac{-(3R_1+R_f)}{3L_1} & \frac{1}{3L_1} & \frac{-1}{3L_1} & 0 & \frac{R_f}{3L_1} \\ 0 & \frac{1}{3C_f} & \frac{-1}{3C_f} & 0 & 0 & \frac{-1}{3C_f} & \frac{1}{3C_f} \\ 0 & \frac{1}{3C_f} & \frac{2}{3C_f} & 0 & 0 & \frac{-1}{3C_f} & \frac{-2}{3C_f} \\ 0 & \frac{R_f}{3(L_2+L)} & 0 & \frac{2}{3(L_2+L)} & \frac{1}{3(L_2+L)} & \frac{-3R_L-R_f}{3(L_2+L)} & 0 \\ 0 & 0 & \frac{R_f}{3(L_2+L)} & \frac{-1}{3(L_2+L)} & \frac{1}{3(L_2+L)} & 0 & \frac{-3R_L-R_f}{3(L_2+L)} \end{bmatrix}, B_{110}=B_{000}$$

$$A_{010}=\begin{bmatrix} \frac{-1}{CR_s} & 0 & \frac{-1}{C} & 0 & 0 & 0 & 0 \\ \frac{-1}{3L_1} & \frac{-(3R_1+R_f)}{3L_1} & 0 & \frac{-2}{3L_1} & \frac{-1}{3L_1} & \frac{R_f}{3L_1} & 0 \\ \frac{2}{3L_1} & 0 & \frac{-(3R_1+R_f)}{3L_1} & \frac{1}{3L_1} & \frac{-1}{3L_1} & 0 & \frac{R_f}{3L_1} \\ 0 & \frac{1}{3C_f} & \frac{-1}{3C_f} & 0 & 0 & \frac{-1}{3C_f} & \frac{1}{3C_f} \\ 0 & \frac{1}{3C_f} & \frac{2}{3C_f} & 0 & 0 & \frac{-1}{3C_f} & \frac{-2}{3C_f} \\ 0 & \frac{R_f}{3(L_2+L)} & 0 & \frac{2}{3(L_2+L)} & \frac{1}{3(L_2+L)} & \frac{-3R_L-R_f}{3(L_2+L)} & 0 \\ 0 & 0 & \frac{R_f}{3(L_2+L)} & \frac{-1}{3(L_2+L)} & \frac{1}{3(L_2+L)} & 0 & \frac{-3R_L-R_f}{3(L_2+L)} \end{bmatrix}, B_{010}=B_{000}$$

$$A_{011}=\begin{bmatrix} \frac{-1}{CR_s} & \frac{1}{C} & 0 & 0 & 0 & 0 & 0 \\ \frac{-2}{3L_1} & \frac{-(3R_1+R_f)}{3L_1} & 0 & \frac{-2}{3L_1} & \frac{-1}{3L_1} & \frac{R_f}{3L_1} & 0 \\ \frac{1}{3L_1} & 0 & \frac{-(3R_1+R_f)}{3L_1} & \frac{1}{3L_1} & \frac{-1}{3L_1} & 0 & \frac{R_f}{3L_1} \\ 0 & \frac{1}{3C_f} & \frac{-1}{3C_f} & 0 & 0 & \frac{-1}{3C_f} & \frac{1}{3C_f} \\ 0 & \frac{1}{3C_f} & \frac{2}{3C_f} & 0 & 0 & \frac{-1}{3C_f} & \frac{-2}{3C_f} \\ 0 & \frac{R_f}{3(L_2+L)} & 0 & \frac{2}{3(L_2+L)} & \frac{1}{3(L_2+L)} & \frac{-3R_L-R_f}{3(L_2+L)} & 0 \\ 0 & 0 & \frac{R_f}{3(L_2+L)} & \frac{-1}{3(L_2+L)} & \frac{1}{3(L_2+L)} & 0 & \frac{-3R_L-R_f}{3(L_2+L)} \end{bmatrix}, B_{011}=B_{000}$$

$$A_{001}=\begin{bmatrix}\frac{-1}{CR_s} & \frac{1}{C} & \frac{1}{C} & 0 & 0 & 0 & 0\\ \frac{-1}{3L_1} & \frac{-(3R_1+R_f)}{3L_1} & 0 & \frac{-2}{3L_1} & \frac{-1}{3L_1} & \frac{R_f}{3L_1} & 0\\ \frac{-1}{3L_1} & 0 & \frac{-(3R_1+R_f)}{3L_1} & \frac{1}{3L_1} & \frac{-1}{3L_1} & 0 & \frac{R_f}{3L_1}\\ 0 & \frac{1}{3C_f} & \frac{-1}{3C_f} & 0 & 0 & \frac{-1}{3C_f} & \frac{1}{3C_f}\\ 0 & \frac{1}{3C_f} & \frac{2}{3C_f} & 0 & 0 & \frac{-1}{3C_f} & \frac{-2}{3C_f}\\ 0 & \frac{R_f}{3(L_2+L)} & 0 & \frac{2}{3(L_2+L)} & \frac{1}{3(L_2+L)} & \frac{-3R_L-R_f}{3(L_2+L)} & 0\\ 0 & 0 & \frac{R_f}{3(L_2+L)} & \frac{-1}{3(L_2+L)} & \frac{1}{3(L_2+L)} & 0 & \frac{-3R_L-R_f}{3(L_2+L)}\end{bmatrix}, B_{001}=B_{000}$$

$$A_{101}=\begin{bmatrix}\frac{-1}{CR_s} & 0 & \frac{1}{C} & 0 & 0 & 0 & 0\\ \frac{1}{3L_1} & \frac{-(3R_1+R_f)}{3L_1} & 0 & \frac{-2}{3L_1} & \frac{-1}{3L_1} & \frac{R_f}{3L_1} & 0\\ \frac{-2}{3L_1} & 0 & \frac{-(3R_1+R_f)}{3L_1} & \frac{1}{3L_1} & \frac{-1}{3L_1} & 0 & \frac{R_f}{3L_1}\\ 0 & \frac{1}{3C_f} & \frac{-1}{3C_f} & 0 & 0 & \frac{-1}{3C_f} & \frac{1}{3C_f}\\ 0 & \frac{1}{3C_f} & \frac{2}{3C_f} & 0 & 0 & \frac{-1}{3C_f} & \frac{-2}{3C_f}\\ 0 & \frac{R_f}{3(L_2+L)} & 0 & \frac{2}{3(L_2+L)} & \frac{1}{3(L_2+L)} & \frac{-3R_L-R_f}{3(L_2+L)} & 0\\ 0 & 0 & \frac{R_f}{3(L_2+L)} & \frac{-1}{3(L_2+L)} & \frac{1}{3(L_2+L)} & 0 & \frac{-3R_L-R_f}{3(L_2+L)}\end{bmatrix}, B_{101}=B_{000}$$

B) Grid-Tied:

$$A_{000} = \begin{bmatrix} \frac{-1}{CR_s} & 0 & 0 & 0 & 0 & 0 & 0 \\ 0 & \frac{-(3R_1+R_f)}{3L_1} & 0 & \frac{-2}{3L_1} & \frac{-1}{3L_1} & \frac{R_f}{3L_1} & 0 \\ 0 & 0 & \frac{-(3R_1+R_f)}{3L_1} & \frac{1}{3L_1} & \frac{-1}{3L_1} & 0 & \frac{R_f}{3L_1} \\ 0 & \frac{1}{3C_f} & \frac{-1}{3C_f} & 0 & 0 & \frac{-1}{3C_f} & \frac{1}{3C_f} \\ 0 & \frac{1}{3C_f} & \frac{2}{3C_f} & 0 & 0 & \frac{-1}{3C_f} & \frac{-2}{3C_f} \\ 0 & \frac{R_f}{3(L_2+L_g)} & 0 & \frac{2}{3(L_2+L_g)} & \frac{1}{3(L_2+L_g)} & \frac{-3R_L-R_f}{3(L_2+L_g)} & 0 \\ 0 & 0 & \frac{R_f}{3(L_2+L_g)} & \frac{-1}{3(L_2+L_g)} & \frac{1}{3(L_2+L_g)} & 0 & \frac{-3R_L-R_f}{3(L_2+L_g)} \end{bmatrix}, B_{000} =$$

$$\begin{bmatrix} \frac{1}{CR_s} & 0 & 0 \\ 0 & 0 & 0 \\ 0 & 0 & 0 \\ 0 & 0 & 0 \\ 0 & 0 & 0 \\ 0 & \frac{-2}{3(L_2+L_g)} & \frac{-1}{3(L_2+L_g)} \\ 0 & \frac{1}{3(L_2+L_g)} & \frac{-1}{3(L_2+L_g)} \end{bmatrix}$$

$$A_{100} = \begin{bmatrix} \frac{-1}{CR_s} & \frac{-1}{C} & 0 & 0 & 0 & 0 & 0 \\ \frac{2}{3L_1} & \frac{-(3R_1+R_f)}{3L_1} & 0 & \frac{-2}{3L_1} & \frac{-1}{3L_1} & \frac{R_f}{3L_1} & 0 \\ \frac{-1}{3L_1} & 0 & \frac{-(3R_1+R_f)}{3L_1} & \frac{1}{3L_1} & \frac{-1}{3L_1} & 0 & \frac{R_f}{3L_1} \\ 0 & \frac{1}{3C_f} & \frac{-1}{3C_f} & 0 & 0 & \frac{-1}{3C_f} & \frac{1}{3C_f} \\ 0 & \frac{1}{3C_f} & \frac{2}{3C_f} & 0 & 0 & \frac{-1}{3C_f} & \frac{-2}{3C_f} \\ 0 & \frac{R_f}{3(L_2+L_g)} & 0 & \frac{2}{3(L_2+L_g)} & \frac{1}{3(L_2+L_g)} & \frac{-3R_L-R_f}{3(L_2+L_g)} & 0 \\ 0 & 0 & \frac{R_f}{3(L_2+L_g)} & \frac{-1}{3(L_2+L_g)} & \frac{1}{3(L_2+L_g)} & 0 & \frac{-3R_L-R_f}{3(L_2+L_g)} \end{bmatrix}, B_{100} = B_{000}$$

$$A_{110}=\begin{bmatrix}\frac{-1}{CR_s} & \frac{-1}{C} & \frac{-1}{C} & 0 & 0 & 0 & 0\\ \frac{1}{3L_1} & \frac{-(3R_1+R_f)}{3L_1} & 0 & \frac{-2}{3L_1} & \frac{-1}{3L_1} & \frac{R_f}{3L_1} & 0\\ \frac{1}{3L_1} & 0 & \frac{-(3R_1+R_f)}{3L_1} & \frac{1}{3L_1} & \frac{-1}{3L_1} & 0 & \frac{R_f}{3L_1}\\ 0 & \frac{1}{3C_f} & \frac{-1}{3C_f} & 0 & 0 & \frac{-1}{3C_f} & \frac{1}{3C_f}\\ 0 & \frac{1}{3C_f} & \frac{2}{3C_f} & 0 & 0 & \frac{-1}{3C_f} & \frac{-2}{3C_f}\\ 0 & \frac{R_f}{3(L_2+L_g)} & 0 & \frac{2}{3(L_2+L_g)} & \frac{1}{3(L_2+L_g)} & \frac{-3R_L-R_f}{3(L_2+L_g)} & 0\\ 0 & 0 & \frac{R_f}{3(L_2+L_g)} & \frac{-1}{3(L_2+L_g)} & \frac{1}{3(L_2+L_g)} & 0 & \frac{-3R_L-R_f}{3(L_2+L_g)}\end{bmatrix}, B_{110}=B_{000}$$

$$A_{010}=\begin{bmatrix}\frac{-1}{CR_s} & 0 & \frac{-1}{C} & 0 & 0 & 0 & 0\\ \frac{-1}{3L_1} & \frac{-(3R_1+R_f)}{3L_1} & 0 & \frac{-2}{3L_1} & \frac{-1}{3L_1} & \frac{R_f}{3L_1} & 0\\ \frac{2}{3L_1} & 0 & \frac{-(3R_1+R_f)}{3L_1} & \frac{1}{3L_1} & \frac{-1}{3L_1} & 0 & \frac{R_f}{3L_1}\\ 0 & \frac{1}{3C_f} & \frac{-1}{3C_f} & 0 & 0 & \frac{-1}{3C_f} & \frac{1}{3C_f}\\ 0 & \frac{1}{3C_f} & \frac{2}{3C_f} & 0 & 0 & \frac{-1}{3C_f} & \frac{-2}{3C_f}\\ 0 & \frac{R_f}{3(L_2+L_g)} & 0 & \frac{2}{3(L_2+L_g)} & \frac{1}{3(L_2+L_g)} & \frac{-3R_L-R_f}{3(L_2+L_g)} & 0\\ 0 & 0 & \frac{R_f}{3(L_2+L_g)} & \frac{-1}{3(L_2+L_g)} & \frac{1}{3(L_2+L_g)} & 0 & \frac{-3R_L-R_f}{3(L_2+L_g)}\end{bmatrix}, B_{010}=B_{000}$$

$$A_{011}=\begin{bmatrix}\frac{-1}{CR_s} & \frac{1}{C} & 0 & 0 & 0 & 0 & 0\\ \frac{-2}{3L_1} & \frac{-(3R_1+R_f)}{3L_1} & 0 & \frac{-2}{3L_1} & \frac{-1}{3L_1} & \frac{R_f}{3L_1} & 0\\ \frac{1}{3L_1} & 0 & \frac{-(3R_1+R_f)}{3L_1} & \frac{1}{3L_1} & \frac{-1}{3L_1} & 0 & \frac{R_f}{3L_1}\\ 0 & \frac{1}{3C_f} & \frac{-1}{3C_f} & 0 & 0 & \frac{-1}{3C_f} & \frac{1}{3C_f}\\ 0 & \frac{1}{3C_f} & \frac{2}{3C_f} & 0 & 0 & \frac{-1}{3C_f} & \frac{-2}{3C_f}\\ 0 & \frac{R_f}{3(L_2+L_g)} & 0 & \frac{2}{3(L_2+L_g)} & \frac{1}{3(L_2+L_g)} & \frac{-3R_L-R_f}{3(L_2+L_g)} & 0\\ 0 & 0 & \frac{R_f}{3(L_2+L_g)} & \frac{-1}{3(L_2+L_g)} & \frac{1}{3(L_2+L_g)} & 0 & \frac{-3R_L-R_f}{3(L_2+L_g)}\end{bmatrix}, B_{011}=B_{000}$$

$$A_{001}=\begin{bmatrix}\frac{-1}{CR_s} & \frac{1}{C} & \frac{1}{C} & 0 & 0 & 0 & 0\\ \frac{-1}{3L_1} & \frac{-(3R_1+R_f)}{3L_1} & 0 & \frac{-2}{3L_1} & \frac{-1}{3L_1} & \frac{R_f}{3L_1} & 0\\ \frac{-1}{3L_1} & 0 & \frac{-(3R_1+R_f)}{3L_1} & \frac{1}{3L_1} & \frac{-1}{3L_1} & 0 & \frac{R_f}{3L_1}\\ 0 & \frac{1}{3C_f} & \frac{-1}{3C_f} & 0 & 0 & \frac{-1}{3C_f} & \frac{1}{3C_f}\\ 0 & \frac{1}{3C_f} & \frac{2}{3C_f} & 0 & 0 & \frac{-1}{3C_f} & \frac{-2}{3C_f}\\ 0 & \frac{R_f}{3(L_2+L_g)} & 0 & \frac{2}{3(L_2+L_g)} & \frac{1}{3(L_2+L_g)} & \frac{-3R_L-R_f}{3(L_2+L_g)} & 0\\ 0 & 0 & \frac{R_f}{3(L_2+L_g)} & \frac{-1}{3(L_2+L_g)} & \frac{1}{3(L_2+L_g)} & 0 & \frac{-3R_L-R_f}{3(L_2+L_g)}\end{bmatrix}, B_{001}=B_{000}$$

$$A_{101}=\begin{bmatrix}\frac{-1}{CR_s} & 0 & \frac{1}{C} & 0 & 0 & 0 & 0\\ \frac{1}{3L_1} & \frac{-(3R_1+R_f)}{3L_1} & 0 & \frac{-2}{3L_1} & \frac{-1}{3L_1} & \frac{R_f}{3L_1} & 0\\ \frac{-2}{3L_1} & 0 & \frac{-(3R_1+R_f)}{3L_1} & \frac{1}{3L_1} & \frac{-1}{3L_1} & 0 & \frac{R_f}{3L_1}\\ 0 & \frac{1}{3C_f} & \frac{-1}{3C_f} & 0 & 0 & \frac{-1}{3C_f} & \frac{1}{3C_f}\\ 0 & \frac{1}{3C_f} & \frac{2}{3C_f} & 0 & 0 & \frac{-1}{3C_f} & \frac{-2}{3C_f}\\ 0 & \frac{R_f}{3(L_2+L_g)} & 0 & \frac{2}{3(L_2+L_g)} & \frac{1}{3(L_2+L_g)} & \frac{-3R_L-R_f}{3(L_2+L_g)} & 0\\ 0 & 0 & \frac{R_f}{3(L_2+L_g)} & \frac{-1}{3(L_2+L_g)} & \frac{1}{3(L_2+L_g)} & 0 & \frac{-3R_L-R_f}{3(L_2+L_g)}\end{bmatrix}, B_{101}=B_{000}$$

Appendix B: Averaged State-Space Models of SVPWM Sectors

A) Stand-Alone:

$$\bar{A}_I = \begin{bmatrix} \frac{-1}{CR_s} & \frac{-(d_1+d_2)}{C} & \frac{-d_2}{C} & 0 & 0 & 0 & 0 \\ \frac{2d_1+d_2}{3L_1} & \frac{-(3R_1+R_f)}{3L_1} & 0 & \frac{-2}{3L_1} & \frac{-1}{3L_1} & \frac{R_f}{3L_1} & 0 \\ \frac{-d_1+d_2}{3L_1} & 0 & \frac{-(3R_1+R_f)}{3L_1} & \frac{1}{3L_1} & \frac{-1}{3L_1} & 0 & \frac{R_f}{3L_1} \\ 0 & \frac{1}{3C_f} & \frac{-1}{3C_f} & 0 & 0 & \frac{-1}{3C_f} & \frac{1}{3C_f} \\ 0 & \frac{1}{3C_f} & \frac{2}{3C_f} & 0 & 0 & \frac{-1}{3C_f} & \frac{-2}{3C_f} \\ 0 & \frac{R_f}{3(L_2+L)} & 0 & \frac{2}{3(L_2+L)} & \frac{1}{3(L_2+L)} & \frac{-3R_L-R_f}{3(L_2+L)} & 0 \\ 0 & 0 & \frac{R_f}{3(L_2+L)} & \frac{-1}{3(L_2+L)} & \frac{1}{3(L_2+L)} & 0 & \frac{-3R_L-R_f}{3(L_2+L)} \end{bmatrix}$$

$$\bar{A}_{II} = \begin{bmatrix} \frac{-1}{CR_s} & \frac{-d_1}{C} & \frac{-(d_1+d_2)}{C} & 0 & 0 & 0 & 0 \\ \frac{d_1-d_2}{3L_1} & \frac{-(3R_1+R_f)}{3L_1} & 0 & \frac{-2}{3L_1} & \frac{-1}{3L_1} & \frac{R_f}{3L_1} & 0 \\ \frac{d_1+2d_2}{3L_1} & 0 & \frac{-(3R_1+R_f)}{3L_1} & \frac{1}{3L_1} & \frac{-1}{3L_1} & 0 & \frac{R_f}{3L_1} \\ 0 & \frac{1}{3C_f} & \frac{-1}{3C_f} & 0 & 0 & \frac{-1}{3C_f} & \frac{1}{3C_f} \\ 0 & \frac{1}{3C_f} & \frac{2}{3C_f} & 0 & 0 & \frac{-1}{3C_f} & \frac{-2}{3C_f} \\ 0 & \frac{R_f}{3(L_2+L)} & 0 & \frac{2}{3(L_2+L)} & \frac{1}{3(L_2+L)} & \frac{-3R_L-R_f}{3(L_2+L)} & 0 \\ 0 & 0 & \frac{R_f}{3(L_2+L)} & \frac{-1}{3(L_2+L)} & \frac{1}{3(L_2+L)} & 0 & \frac{-3R_L-R_f}{3(L_2+L)} \end{bmatrix}$$

$$\bar{A}_{III} = \begin{bmatrix} \frac{-1}{CR_s} & \frac{d_2}{C} & \frac{-d_1}{C} & 0 & 0 & 0 & 0 \\ \frac{-(d_1+2d_2)}{3L_1} & \frac{-(3R_1+R_f)}{3L_1} & 0 & \frac{-2}{3L_1} & \frac{-1}{3L_1} & \frac{R_f}{3L_1} & 0 \\ \frac{2d_1+d_2}{3L_1} & 0 & \frac{-(3R_1+R_f)}{3L_1} & \frac{1}{3L_1} & \frac{-1}{3L_1} & 0 & \frac{R_f}{3L_1} \\ 0 & \frac{1}{3C_f} & \frac{-1}{3C_f} & 0 & 0 & \frac{-1}{3C_f} & \frac{1}{3C_f} \\ 0 & \frac{1}{3C_f} & \frac{2}{3C_f} & 0 & 0 & \frac{-1}{3C_f} & \frac{-2}{3C_f} \\ 0 & \frac{R_f}{3(L_2+L)} & 0 & \frac{2}{3(L_2+L)} & \frac{1}{3(L_2+L)} & \frac{-3R_L-R_f}{3(L_2+L)} & 0 \\ 0 & 0 & \frac{R_f}{3(L_2+L)} & \frac{-1}{3(L_2+L)} & \frac{1}{3(L_2+L)} & 0 & \frac{-3R_L-R_f}{3(L_2+L)} \end{bmatrix}$$

$$\bar{A}_{IV} = \begin{bmatrix} \frac{-1}{CR_S} & \frac{d_1+d_2}{C} & \frac{d_2}{C} & 0 & 0 & 0 & 0 \\ \frac{-(2d_1+d_2)}{3L_1} & \frac{-(3R_1+R_f)}{3L_1} & 0 & \frac{-2}{3L_1} & \frac{-1}{3L_1} & \frac{R_f}{3L_1} & 0 \\ \frac{d_1-d_2}{3L_1} & 0 & \frac{-(3R_1+R_f)}{3L_1} & \frac{1}{3L_1} & \frac{-1}{3L_1} & 0 & \frac{R_f}{3L_1} \\ 0 & \frac{1}{3C_f} & \frac{-1}{3C_f} & 0 & 0 & \frac{-1}{3C_f} & \frac{1}{3C_f} \\ 0 & \frac{1}{3C_f} & \frac{2}{3C_f} & 0 & 0 & \frac{-1}{3C_f} & \frac{-2}{3C_f} \\ 0 & \frac{R_f}{3(L_2+L)} & 0 & \frac{2}{3(L_2+L)} & \frac{1}{3(L_2+L)} & \frac{-3R_L-R_f}{3(L_2+L)} & 0 \\ 0 & 0 & \frac{R_f}{3(L_2+L)} & \frac{-1}{3(L_2+L)} & \frac{1}{3(L_2+L)} & 0 & \frac{-3R_L-R_f}{3(L_2+L)} \end{bmatrix}$$

$$\bar{A}_{V} = \begin{bmatrix} \frac{-1}{CR_S} & \frac{d_1}{C} & \frac{d_1+d_2}{C} & 0 & 0 & 0 & 0 \\ \frac{-d_1+d_2}{3L_1} & \frac{-(3R_1+R_f)}{3L_1} & 0 & \frac{-2}{3L_1} & \frac{-1}{3L_1} & \frac{R_f}{3L_1} & 0 \\ \frac{-(d_1+2d_2)}{3L_1} & 0 & \frac{-(3R_1+R_f)}{3L_1} & \frac{1}{3L_1} & \frac{-1}{3L_1} & 0 & \frac{R_f}{3L_1} \\ 0 & \frac{1}{3C_f} & \frac{-1}{3C_f} & 0 & 0 & \frac{-1}{3C_f} & \frac{1}{3C_f} \\ 0 & \frac{1}{3C_f} & \frac{2}{3C_f} & 0 & 0 & \frac{-1}{3C_f} & \frac{-2}{3C_f} \\ 0 & \frac{R_f}{3(L_2+L)} & 0 & \frac{2}{3(L_2+L)} & \frac{1}{3(L_2+L)} & \frac{-3R_L-R_f}{3(L_2+L)} & 0 \\ 0 & 0 & \frac{R_f}{3(L_2+L)} & \frac{-1}{3(L_2+L)} & \frac{1}{3(L_2+L)} & 0 & \frac{-3R_L-R_f}{3(L_2+L)} \end{bmatrix}$$

$$\bar{A}_{VI} = \begin{bmatrix} \frac{-1}{CR_S} & \frac{-d_1}{C} & \frac{d_2}{C} & 0 & 0 & 0 & 0 \\ \frac{d_1+2d_2}{3L_1} & \frac{-(3R_1+R_f)}{3L_1} & 0 & \frac{-2}{3L_1} & \frac{-1}{3L_1} & \frac{R_f}{3L_1} & 0 \\ \frac{-(2d_1+d_2)}{3L_1} & 0 & \frac{-(3R_1+R_f)}{3L_1} & \frac{1}{3L_1} & \frac{-1}{3L_1} & 0 & \frac{R_f}{3L_1} \\ 0 & \frac{1}{3C_f} & \frac{-1}{3C_f} & 0 & 0 & \frac{-1}{3C_f} & \frac{1}{3C_f} \\ 0 & \frac{1}{3C_f} & \frac{2}{3C_f} & 0 & 0 & \frac{-1}{3C_f} & \frac{-2}{3C_f} \\ 0 & \frac{R_f}{3(L_2+L)} & 0 & \frac{2}{3(L_2+L)} & \frac{1}{3(L_2+L)} & \frac{-3R_L-R_f}{3(L_2+L)} & 0 \\ 0 & 0 & \frac{R_f}{3(L_2+L)} & \frac{-1}{3(L_2+L)} & \frac{1}{3(L_2+L)} & 0 & \frac{-3R_L-R_f}{3(L_2+L)} \end{bmatrix}$$

B) Grid-Tied:

$$\bar{A}_I = \begin{bmatrix} \frac{-1}{CR_s} & \frac{-(d_1+d_2)}{C} & \frac{-d_2}{C} & 0 & 0 & 0 & 0 \\ \frac{2d_1+d_2}{3L_1} & \frac{-(3R_1+R_f)}{3L_1} & 0 & \frac{-2}{3L_1} & \frac{-1}{3L_1} & \frac{R_f}{3L_1} & 0 \\ \frac{-d_1+d_2}{3L_1} & 0 & \frac{-(3R_1+R_f)}{3L_1} & \frac{1}{3L_1} & \frac{-1}{3L_1} & 0 & \frac{R_f}{3L_1} \\ 0 & \frac{1}{3C_f} & \frac{-1}{3C_f} & 0 & 0 & \frac{-1}{3C_f} & \frac{1}{3C_f} \\ 0 & \frac{1}{3C_f} & \frac{2}{3C_f} & 0 & 0 & \frac{-1}{3C_f} & \frac{-2}{3C_f} \\ 0 & \frac{R_f}{3(L_2+L_g)} & 0 & \frac{2}{3(L_2+L_g)} & \frac{1}{3(L_2+L_g)} & \frac{-3R_L-R_f}{3(L_2+L_g)} & 0 \\ 0 & 0 & \frac{R_f}{3(L_2+L_g)} & \frac{-1}{3(L_2+L_g)} & \frac{1}{3(L_2+L_g)} & 0 & \frac{-3R_L-R_f}{3(L_2+L_g)} \end{bmatrix}$$

$$\bar{A}_{II} = \begin{bmatrix} \frac{-1}{CR_s} & \frac{-d_1}{C} & \frac{-(d_1+d_2)}{C} & 0 & 0 & 0 & 0 \\ \frac{d_1-d_2}{3L_1} & \frac{-(3R_1+R_f)}{3L_1} & 0 & \frac{-2}{3L_1} & \frac{-1}{3L_1} & \frac{R_f}{3L_1} & 0 \\ \frac{d_1+2d_2}{3L_1} & 0 & \frac{-(3R_1+R_f)}{3L_1} & \frac{1}{3L_1} & \frac{-1}{3L_1} & 0 & \frac{R_f}{3L_1} \\ 0 & \frac{1}{3C_f} & \frac{-1}{3C_f} & 0 & 0 & \frac{-1}{3C_f} & \frac{1}{3C_f} \\ 0 & \frac{1}{3C_f} & \frac{2}{3C_f} & 0 & 0 & \frac{-1}{3C_f} & \frac{-2}{3C_f} \\ 0 & \frac{R_f}{3(L_2+L_g)} & 0 & \frac{2}{3(L_2+L_g)} & \frac{1}{3(L_2+L_g)} & \frac{-3R_L-R_f}{3(L_2+L_g)} & 0 \\ 0 & 0 & \frac{R_f}{3(L_2+L_g)} & \frac{-1}{3(L_2+L_g)} & \frac{1}{3(L_2+L_g)} & 0 & \frac{-3R_L-R_f}{3(L_2+L_g)} \end{bmatrix}$$

$$\bar{A}_{III} = \begin{bmatrix} \frac{-1}{CR_s} & \frac{d_2}{C} & \frac{-d_1}{C} & 0 & 0 & 0 & 0 \\ \frac{-(d_1+2d_2)}{3L_1} & \frac{-(3R_1+R_f)}{3L_1} & 0 & \frac{-2}{3L_1} & \frac{-1}{3L_1} & \frac{R_f}{3L_1} & 0 \\ \frac{2d_1+d_2}{3L_1} & 0 & \frac{-(3R_1+R_f)}{3L_1} & \frac{1}{3L_1} & \frac{-1}{3L_1} & 0 & \frac{R_f}{3L_1} \\ 0 & \frac{1}{3C_f} & \frac{-1}{3C_f} & 0 & 0 & \frac{-1}{3C_f} & \frac{1}{3C_f} \\ 0 & \frac{1}{3C_f} & \frac{2}{3C_f} & 0 & 0 & \frac{-1}{3C_f} & \frac{-2}{3C_f} \\ 0 & \frac{R_f}{3(L_2+L_g)} & 0 & \frac{2}{3(L_2+L_g)} & \frac{1}{3(L_2+L_g)} & \frac{-3R_L-R_f}{3(L_2+L_g)} & 0 \\ 0 & 0 & \frac{R_f}{3(L_2+L_g)} & \frac{-1}{3(L_2+L_g)} & \frac{1}{3(L_2+L_g)} & 0 & \frac{-3R_L-R_f}{3(L_2+L_g)} \end{bmatrix}$$

$$\bar{A}_{IV} = \begin{bmatrix} \frac{-1}{CR_s} & \frac{d_1+d_2}{C} & \frac{d_2}{C} & 0 & 0 & 0 & 0 \\ \frac{-(2d_1+d_2)}{3L_1} & \frac{-(3R_1+R_f)}{3L_1} & 0 & \frac{-2}{3L_1} & \frac{-1}{3L_1} & \frac{R_f}{3L_1} & 0 \\ \frac{d_1-d_2}{3L_1} & 0 & \frac{-(3R_1+R_f)}{3L_1} & \frac{1}{3L_1} & \frac{-1}{3L_1} & 0 & \frac{R_f}{3L_1} \\ 0 & \frac{1}{3C_f} & \frac{-1}{3C_f} & 0 & 0 & \frac{-1}{3C_f} & \frac{1}{3C_f} \\ 0 & \frac{1}{3C_f} & \frac{2}{3C_f} & 0 & 0 & \frac{-1}{3C_f} & \frac{-2}{3C_f} \\ 0 & \frac{R_f}{3(L_2+L_g)} & 0 & \frac{2}{3(L_2+L_g)} & \frac{1}{3(L_2+L_g)} & \frac{-3R_L-R_f}{3(L_2+L_g)} & 0 \\ 0 & 0 & \frac{R_f}{3(L_2+L_g)} & \frac{-1}{3(L_2+L_g)} & \frac{1}{3(L_2+L_g)} & 0 & \frac{-3R_L-R_f}{3(L_2+L_g)} \end{bmatrix}$$

$$\bar{A}_{V} = \begin{bmatrix} \frac{-1}{CR_s} & \frac{d_1}{C} & \frac{d_1+d_2}{C} & 0 & 0 & 0 & 0 \\ \frac{-d_1+d_2}{3L_1} & \frac{-(3R_1+R_f)}{3L_1} & 0 & \frac{-2}{3L_1} & \frac{-1}{3L_1} & \frac{R_f}{3L_1} & 0 \\ \frac{-(d_1+2d_2)}{3L_1} & 0 & \frac{-(3R_1+R_f)}{3L_1} & \frac{1}{3L_1} & \frac{-1}{3L_1} & 0 & \frac{R_f}{3L_1} \\ 0 & \frac{1}{3C_f} & \frac{-1}{3C_f} & 0 & 0 & \frac{-1}{3C_f} & \frac{1}{3C_f} \\ 0 & \frac{1}{3C_f} & \frac{2}{3C_f} & 0 & 0 & \frac{-1}{3C_f} & \frac{-2}{3C_f} \\ 0 & \frac{R_f}{3(L_2+L_g)} & 0 & \frac{2}{3(L_2+L_g)} & \frac{1}{3(L_2+L_g)} & \frac{-3R_L-R_f}{3(L_2+L_g)} & 0 \\ 0 & 0 & \frac{R_f}{3(L_2+L_g)} & \frac{-1}{3(L_2+L_g)} & \frac{1}{3(L_2+L_g)} & 0 & \frac{-3R_L-R_f}{3(L_2+L_g)} \end{bmatrix}$$

$$\bar{A}_{VI} = \begin{bmatrix} \frac{-1}{CR_s} & \frac{-d_1}{C} & \frac{d_2}{C} & 0 & 0 & 0 & 0 \\ \frac{d_1+2d_2}{3L_1} & \frac{-(3R_1+R_f)}{3L_1} & 0 & \frac{-2}{3L_1} & \frac{-1}{3L_1} & \frac{R_f}{3L_1} & 0 \\ \frac{-(2d_1+d_2)}{3L_1} & 0 & \frac{-(3R_1+R_f)}{3L_1} & \frac{1}{3L_1} & \frac{-1}{3L_1} & 0 & \frac{R_f}{3L_1} \\ 0 & \frac{1}{3C_f} & \frac{-1}{3C_f} & 0 & 0 & \frac{-1}{3C_f} & \frac{1}{3C_f} \\ 0 & \frac{1}{3C_f} & \frac{2}{3C_f} & 0 & 0 & \frac{-1}{3C_f} & \frac{-2}{3C_f} \\ 0 & \frac{R_f}{3(L_2+L_g)} & 0 & \frac{2}{3(L_2+L_g)} & \frac{1}{3(L_2+L_g)} & \frac{-3R_L-R_f}{3(L_2+L_g)} & 0 \\ 0 & 0 & \frac{R_f}{3(L_2+L_g)} & \frac{-1}{3(L_2+L_g)} & \frac{1}{3(L_2+L_g)} & 0 & \frac{-3R_L-R_f}{3(L_2+L_g)} \end{bmatrix}$$